Alma Mater Studiorum · Università di Bologna

Scuola di Scienze
Corso di Laurea Magistrale in Fisica

THE WIND PROFILE IN THE ATMOSPHERIC STABLE BOUNDARY LAYER OVER COMPLEX TERRAIN AND HETEROGENEOUS SURFACES: LIMITATIONS OF LOCAL SIMILARITY THEORY

Relatore:
Prof. Silvana Di Sabatino

Presentata da:
Mario Schiavon

Correlatore:
Prof. Francesco Tampieri

Sessione II
Anno Accademico 2014/2015

Sommario

L'indagine ha riguardato il profilo del vento nei primi 30 metri dello strato limite atmosferico stabile nell'ambito della teoria di similarità locale formulata da Nieuwstadt nel 1984 come estensione della similarità di Monin-Obukhov (1954). Ad oggi, diversi esperimenti hanno confermato la validità della teoria per strati-limite stabili (almeno per $0 < z/\Lambda \lesssim 1$, z, altezza dal suolo e Λ, lunghezza di Obukhov locale) su terreni che si avvicinavano il più possibile alla condizione ideale di superficie piatta e omogenea. Tuttavia, tali superfici sono piuttosto rare ed è perciò interessante comprendere quali siano i limiti di validità della teoria in condizioni di terreno complesso e superfici non uniformi.

Entrambe le condizioni sono presenti a Ny-Ålesund, Svalbard (Norvegia) dove si trova la Climate Change Tower (CCT): una torre alta 30 m gestita dal Consiglio Nazionale delle Ricerche (CNR). La torre si trova a circa 1 km dalla costa, in un fiordo artico, su terreni ondulati e a distanza di qualche kilometro da montagne che raggiungono i 700 m di altezza.

Parte delle misure di vento (da quattro anemometri a elica) e di turbolenza (da tre anemoetri sonici) acquisite sulla CCT, da Maggio 2012 a Maggio 2013, sono state analizzate nell'ambito della teoria della similarità locale. In particolare, la dipendenza del gradiente verticale adimensionale della velocità del vento, ϕ_m, dal parametro di stabilità, z/Λ, è stata valuatata a tre altezze dal suolo ($z = 3.7$, 7.5 e 20.5 m) coincidenti con le quote a cui le misure di turbolenza erano acquisite.

Il raffronto tra le misure di vento provenienti dai diversi anemometri presenti sulla torre ha evidenziato deviazioni sistematiche tra il dato sonico e quello ad elica che hanno suggertito diverse influenze della torre su i due tipi di strumenti.

I gradienti del vento ottenuti fittando le osservazioni con profili contenenti un andamento logaritmico o interpolandole con splines (cubiche o lineari) in $\ln z$ sono risultati in generale poco sensibili al metodo utilizzato. Metodi diversi hanno presentato però risposte diverse alla presenza di una *dipslacement height* incognita nel profilo osservato.

Deviazioni significative sono state riscontrate tra le relazioni di flusso-gradiente osservate e quelle maggiormente utlizzate (derivate da osservazioni su terreni piatti) in particolare per i livelli più distanti dal suolo. Tali deviazioni hanno mostrato una dipendenza da z/Λ. Per $z/\Lambda \lesssim 0.1$, valori di ϕ_m più grandi di quelli attesi sono risultati associati a flussi di calore piccoli e anomali, a una perdità di validità di Λ come parametro di stabilità e a un apparente disaccoppiamento tra la superficie e l'atmosfera sovrastante. Tale comportamento è stato riscontrato per venti che soffiavano dal mare verso la costa ed è stato attribuito alla formazione di strati-limite interni. Per $z/\Lambda \gtrsim 0.1$, invece, valori di ϕ_m inferiori a quelli attesi, e decrescenti con la quota, sono stati attribuiti a fenomeni di accentuazione della turbolenza ad opera delle irregolarità del terreno. Non è stato possibile ecludere tuttavia che parte del comportamento osservato avesse origini strumentali.

Il livello di self-correlazione presente nelle relazioni di flusso-gradiente osservate è stato stimato derivando l'espressione per il coefficiente di self-correlazione lineare tra ϕ_m e z/Λ a causa della dipendenza congiunta dal flusso di momento. Inoltre, i livelli di sigificatività della correlazione osservata sono stati ottenuti dalle funzioni di distribuzione empiriche del coefficiente di self-correlazione determinate tramite la generazione di dataset casuali. In generale, le relazioni di flusso-gradiente osservate sono risultate affette da self-correlazione in modo significativo o comunque non trascurabile, in particolare per i livelli più distanti dal suolo.

Abstract

The main topic of the research work was the wind profile in the first 30 meters of the stably stratified atmospheric boundary layer, studied in the framework of local similarity theory, developed by Nieuwstadt in 1984 as an extension of Monin-Obukhov similarity theory (1954). Several experiments, carried out on almost flat and homogeneous terrain, have confirmed the theory in stable conditions, at least for the range $0 < z/\Lambda \lesssim 1$ (z, the height above ground and Λ, the local Obukhov length). This ideal surfaces, however, are not very common and it is then of some interest to asses the limits of the theory on complex terrain and heterogeneous surfaces.

Both these conditions are encountered at Ny-Ålesund, Svalbard (Norway), where in 2009 the Italian National Council of Research (CNR) placed a 30-m high tower: the Climate Change Tower (CCT). The tower is located at about 1 km from the coast of an arctic fjord, on undulated terrain with up to 700-m high mountains few kilometers far.

Some of wind and turbulence measurements acquired on the CCT by four propeller-vane and three sonic anemometers from May 2012 to May 2013 were analyzed in the framework of local similarity theory. In particular, the relation between the dimensionless vertical gradient of wind speed, ϕ_m, and the stability parameter, z/Λ was evaluated at three levels where turbulence measurement were carried out ($z = 3.7$, 7.5 and 20.5 m).

The comparison between wind speed observations from all the anemometers on the CCT has revealed systematic deviations between sonic and propeller readings suggesting uneven influences of the tower's structure on the two instrument types.

An intercomparison between wind speed gradients have shown little sensitivity to the method of estimation when observations were fitted with a profile containing a logarithmic behavior or interpolated with splines (linear or cubic) in $\ln z$. However, different methods have shown different sensitivity to an unknown displacement height.

Deviations between observed and expected ϕ_m from most used flux-gradient relationships (derived on flat terrain) were observed, particularly at the highest levels. For low stabilities (i.e. $z/\Lambda \lesssim 0.1$), higher than expected ϕ_m, caused by anomalously small heat fluxes and Λ, were attributed to a thermal decoupling between surface and the atmosphere above arising from on-shore flows. For higher stabilities (i.e. $z/\Lambda \gtrsim 0.1$), lower than expected and decreasing with height values of ϕ_m were inputed to enhanced turbulence by complex terrain although instrumental effects were not completely ruled out.

To asses the level of self-correlation affecting observed flux-gradient relationships, the expression for the linear self-correlation coefficient between ϕ_m and z/Λ, because of the shared variable u_* (the friction velocity), was derived. Furthermore, the estimation of the strength of the observed correlation from empirical distribution functions of the self-correlation index, derived through random datasets generation, is also proposed. Overall, observed flux-gradient relationships resulted significantly affected by self-correlation, especially for the highest observational levels.

Contents

Introduction

The boundary layer meteorology studies the part of the atmosphere most influenced by the earth's surface. Indicatively, the planetary boundary layer (PBL) extends from the ground up to about 1-2 km (Kaimal and Finnigan, 1994; Stull, 1988), although diurnal, seasonal and geographical variations in PBL's height are large. It is in this layer where exchanges of momentum, heat, water vapor and other species, between the earth's surface and the atmosphere, take place. Here pollutants are released by human activities, plants grow up and biosphere-atmosphere interactions occur. Here, global circulation models have their lowest levels.

We have all experienced boundary layer phenomena since «From our first breath, we spend most of our lives near the earth's surface.» (Stull, 1988). Breezes, fog, fair weather cumulus clouds on sunny days, dust devils, the looping smoke plume from a chimney are among these. However, despite of their "daily" occurrence, all these phenomena hide a fascinating complexity, which is peculiar of all PBL meteorology.

Indeed, PBL's flows are dominated by turbulence, the chaotic and unpredictable motion of fluids. This make the study of the PBL challenging both from a theoretical and an experimental point of view.

Theoretically, PBL's dynamic is described by the Navier-Stokes equations, non-linear partial differential equations, for which no exact solution exists. It is usual, in turbulence research, to express the fluid motion as a superposition of a mean flow (obtained from time, space or, at leas theoretically, ensemble averages of the observed one) and turbulence. However, because of non-linearity, it is not possible to separate the description of the mean component from the turbulent one. Mathematically, the prognostic equations for the mean flow are unclosed since they contain (unknown) turbulence-related terms. Closures can be obtained approximating turbulence-related terms as functions of mean flow variables.

Acquisition and processing of boundary layer data is also a difficult task. Fast-response sensors able to capture the rapid fluctuations of meteorological variables due to turbulent motions were employed not earlier than 50 years ago. The development of sonic anemometry around 1960 (Wyngaard, 1981) represented a great advance in the capability of measuring turbulence. The first systematic use of sonic anemometers in a field program goes back to the 1968 Kansas experiment (Businger et al., 1971; Haugen et al., 1971), from which some results are still used today. However, measuring turbulence present still many issues because high accuracy and resolution are required.

Important advances in turbulence description were obtained from semi-empirical theories, starting from observations and organizing them by mean of dimensional arguments. Similarity theories are among them. They states that, when properly adimensionalized, observations from different experiments should follow the same universal law.

In 1954, the two Russian scientists A. S. Monin and A. M. Obukhov proposed a similarity theory for the profile of mean variables (wind speed, temperature, humidity and other

passive tracers) in the thermally stratified, horizontally homogeneous and quasi-stationary surface layer. In this layer, that occupies roughly the lowest 10% of the whole boundary layer (Stull, 1988) turbulent fluxes do not vary significantly with height and meteorological variables experience their sharpest gradients (Kaimal and Finnigan, 1994). This means that turbulence is driven primarily by gradients of mean variables leading to the concept of *flux-gradient relationship*.

In 1984, Nieuwstadt proposed to extend Monin-Obukhov similarity theory (MOST) above the surface layer, in the stably stratified boundary layer, substituting surface scales with local ones and leading to the so called *local similarity theory*.

Since the formulation of MOST and the possibility to measure turbulent fluxes directly, many surface-layer experiments were conducted for the determination of flux-gradient relationships, mainly over almost flat terrain and homogeneous surfaces. The behaviour of the theory over complex terrain have received recently more attention.

The flux-gradient relations from different experiments show the largest differences for very stable conditions. Also in numerical models that uses flux-profile relationships based on MOST, the largest deviations between predicted and observed fluxes occur for the SBL, especially during winter at higher latitudes (Cheng and Brutsaert, 2005b). These elements suggest that some limitations can exist in the applicability of MOST for stable, or very stable, conditions. It is further no clear if the adoption of local scaling improve similarity (Grachev et al., 2007b).

On the effects causing these deviations for the SBL there is still debate. Indeed, the SBL is characterized by many phenomena that can lead to the break-down of the flux-gradient mechanism: e.g. low level jets, intermittent turbulence, breaking and non-breaking gravity waves, Kelvin-Helmholtz instability (Cheng and Brutsaert, 2005b).

The Admundsen-Nobile Climate Change Tower (CCT) placed at Ny-Ålesund, Svalbard (Norway), by the Italian National Council of Research (CNR) represents a unique opportunity to study the lowest part of the arctic stable boundary layer over non ideal terrain. In the present work, some of the wind speed and turbulence measurement acquired on the CCT from May 2012 to May 2014 are analyzed in the framework of local similarity theory, comparing observations with most used flux-gradient relationships derived over flat and homogeneous surfaces. Particular attention is dedicated also on data selection and analysis methods.

In chapter 1, the theoretical framework in which CCT data were analyzed, with particular attention to similarity theories, is presented. In chapter 2, a brief description of the experimental site, with particular regard to its morphology, and CCT instrumentation is given. In chapter 3, results for the CCT dataset are presented. Conclusions and possible future research are also discussed.

Chapter 1

Theoretical framework

The focus of this study is the wind profile in the lowest tens of meters of the stably stratified atmospheric boundary layer. This chapter should give the main elements of the theoretical framework in which PBL observations and results are interpreted.

After a qualitative description of the main features of the planetary boundary layer (PBL) and its states (section 1.1), whit particular attention to the stably stratified case, equations governing PBL flows and empirical theories that have produced important advances in PBL description are presented.

The physic of the planetary boundary layer is the physic of turbulent flows. In sections 1.2 to 1.4, governing equations, mathematical tools and simplifications adopted in the theoric description of turbulent geophysical flows were presented. Sections 1.5 to 1.9 regard to the surface layer (lowest 10% of the PBL) with particular attention dedicated to Monin-Obukov similarity theory. Finally, in section 1.10, main aspects of local similarity theory, which is the extension of Monin-Obukov similarity for the whole stable boundary layer, are discussed.

1.1 The Planetary Boundary Layer over land

Conventionally, the earth's atmosphere extends from the surface to about 100 km where begins the space. However, about 90% of the mass of the atmosphere is concentrated in the lowest 10 km : the troposphere (the lowest 10% of the atmosphere). It is here where meteorological phenomena occur. The earth's surface is a lower boundary for the atmosphere. The part of the atmosphere most influenced by this boundary is the *planetary boundary layer* (PBL). The PBL height varies in time and space. During a sunny day, in mid latitudes over land it is about 1 km (the lowest 10% of the troposphere). There is a layer even more influenced by the presence of the earth's surface which occupies about the first 10% of the PBL depth : the *surface layer*.

In some general sense, this study refers to the surface-layer, since analyzed observations were collected in the lowest tens of meters of the atmosphere. This can not be true, however, when the PBL height is small and the surface layer concentrated very near to the surface. These conditions can occur in conditions of stable stratification, which was just the focus of this study.

Over land in high pressure conditions (i.e. fair weather), the PBL has a well defined structure that evolves with the diurnal cycle (fig. 1.1).

During day, from some hours after sunrise to before sunset, a *convective* or *well mixed* boundary layer forms. Convectively driven turbulence is maintained by the ground heating

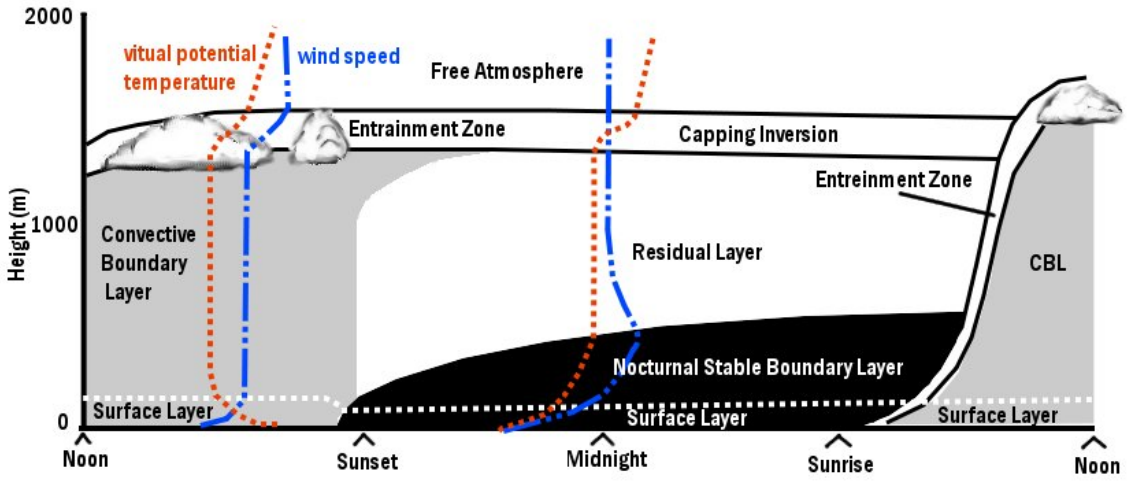

Figure 1.1: The diurnal evolution of the planetary boundary layer over land (rielaboration from Stull, 1988).

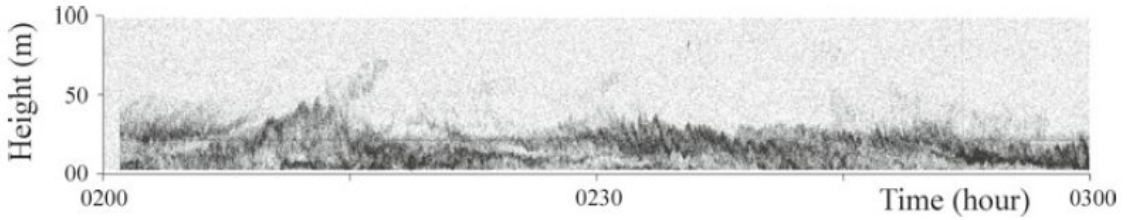

Figure 1.2: Sodar facsimile for a nocturnal stable boundary layer (from Argentini et al., 2012). In this case the SBL top is below 50 m.

from solar radiation. Positively buoyant raising air parcels can organize into *thermals* which may generate cumulus clouds (fair weather cumulus). "Dust-devils" are other phenomena occurring in the CBL. The convective boundary layer (CBL) grows from the top, with the entrainment of less turbulent and stably stratified air of the free atmosphere. The temperature profile is super-adiabatic near the surface and a temperature inversion caps the CBL at the top. In the CBL, wind speed, temperature and humidity profiles are almost constant with height due to the strong turbulent mixing. The CBL reaches its maximum depth in the late afternoon.

Slightly before sunset, the ground starts to cool-down interrupting the feeding of turbulence that begins to decay. The PBL maintains some of the characteristics of the formerly well mixed layer and it is thus called the *residual layer* (RL). As the ground cools-down further, the lowest part of the residual layer is transformed in the *stable boundary layer* (SBL). The RL is thus isolated from the ground, maintaining its neutral stratification and cooling slowly during the night by radiative emission. As the night progresses the SBL grows from stabilization of the lowest part of the RL.

Contrary to the CBL, the SBL has not a well defined top. Furthermore it is characterized by weak and intermittent turbulence with small vertical mixing. Since the stable stratification, gravity waves are also present in the SBL. Reduced mixing and waves are responsible for the wavy layered structure observed in sodar echoes of light winds SBLs (fig. 1.2). Each layer is almost disconnected from the surface leading to the so called z-less stratification (section 1.10). Since reduced vertical mixing and light winds, pollutants

concentration builds-up and fog can form is the SBL.

A temperature inversion characterize the SBL (fig. 1.1): i.e. virtual potential temperature decreases with height until the almost-adiabatic profile of the RL is encountered at the SBL top. The wind profile in the SBL can show quite peculiar characteristics. Indeed, despite light or calm winds near the ground, a wind maximum (a "nose") in the wind profile can be observed at the stable boundary layer top, at about 100 m from the ground (the wind maximum is indeed used to define the SBL height). This is a manifestation of a *low-level* or *nocturnal jet*. The term "jet" is used although the wind speed maximum can not be confined in the horizontal direction forming a layer, instead of a jet, with high wind speed. Low-level jets can be related to katabatic or drainage flows over sloped terrains.

Stable conditions can occur also when warm air is advected over a cooler surface. At high latitudes, when the sun is low above the horizon or polar night is present long lived stable boundary layers onset. In this case, the diurnal cycle of the boundary layer disappears and the SBL can last several days (or even months).

At least in principle, the existence of the surface layer does not depend on stability conditions (fig. 1.1) although its height varies according to PBL height. In the lowest few centimeters of air, a *microlayer* or *interfacial layer*, where molecular transport dominates, has also been individuated (Stull, 1988).

As a new day begins and , after sunrise, a CBL forms again (fig. 1.1) growing from entrainment of nocturnal SBL air. The growth accelerates when the RL is reached.

1.2 The PBL governing equations

The fluid motion in the PBL is described by the Navier-Stokes equations (e.g. Stull, 1988):

$$\frac{\partial u}{\partial t} + u\frac{\partial u}{\partial x} + v\frac{\partial u}{\partial y} + w\frac{\partial u}{\partial z} = -\frac{1}{\rho}\frac{\partial p}{\partial x} + fv + \nu\left(\frac{\partial^2 u}{\partial x^2} + \frac{\partial^2 u}{\partial y^2} + \frac{\partial^2 u}{\partial z^2}\right) \tag{1.1a}$$

$$\frac{\partial v}{\partial t} + u\frac{\partial v}{\partial x} + v\frac{\partial v}{\partial y} + w\frac{\partial v}{\partial z} = -\frac{1}{\rho}\frac{\partial p}{\partial y} - fu + \nu\left(\frac{\partial^2 v}{\partial x^2} + \frac{\partial^2 v}{\partial y^2} + \frac{\partial^2 v}{\partial z^2}\right) \tag{1.1b}$$

$$\frac{\partial w}{\partial t} + u\frac{\partial w}{\partial x} + v\frac{\partial w}{\partial y} + w\frac{\partial w}{\partial z} = -\frac{1}{\rho}\frac{\partial p}{\partial z} - g + \nu\left(\frac{\partial^2 w}{\partial x^2} + \frac{\partial^2 w}{\partial y^2} + \frac{\partial^2 w}{\partial z^2}\right), \tag{1.1c}$$

where the meteorological system is adopted: vertical z-axis aligned with the acceleration of gravity, x-axis pointing east and y-axis pointing north. In (1.1), u, v and w are the westerly, the southerly and the vertical components of the fluid velocity vector; ρ is the fluid density and p, the pressure; $f = 2\Omega \sin\phi$ is the Coriolis parameter, $\Omega = 7 \times 10^{-5}\,\mathrm{s}^{-1}$, the angular speed of earth's rotation and ϕ, the latitude; ν is the kinematic viscosity of the fluid and it assumed constant, for air $\nu = 1.5 \times 10^{-5}\,\mathrm{m}^2\,\mathrm{s}^{-1}$; $g = 9.8\,\mathrm{m\,s}^{-2}$ is the acceleration due to gravity.

The conservation of mass is expressed by the continuity equation:

$$\frac{\partial \rho}{\partial t} + u\frac{\partial \rho}{\partial x} + v\frac{\partial \rho}{\partial y} + w\frac{\partial \rho}{\partial z} = -\rho\left(\frac{\partial u}{\partial x} + \frac{\partial v}{\partial y} + \frac{\partial w}{\partial z}\right). \tag{1.2}$$

Pressure, density and virtual temperature T_v are related by the equation of state for ideal gases:

$$p = R\rho T_v \tag{1.3}$$

where $R = 287\,\mathrm{J\ K^{-1}\ kg^{-1}}$ is the gas constant for dry air and

$$T_v = T(1 + 0.61q) \tag{1.4}$$

for moist unsaturated air (e.g. Wyngaard, 2010), T, the absolute temperature of air and q, the specific humidity (mass of water vapor per mass of moist air).

Instead of the equation for absolute temperature is more convenient to consider that for the potential temperature, θ:

$$\frac{\partial\theta}{\partial t} + u\frac{\partial\theta}{\partial x} + v\frac{\partial\theta}{\partial y} + w\frac{\partial\theta}{\partial z} = \nu_\theta\left(\frac{\partial^2\theta}{\partial x^2} + \frac{\partial^2\theta}{\partial y^2} + \frac{\partial^2\theta}{\partial z^2}\right) - \frac{1}{\rho c_p}\left(\frac{\partial Q_x^*}{\partial x} + \frac{\partial Q_y^*}{\partial y} + \frac{\partial Q_x^*}{\partial z}\right) \tag{1.5}$$

where the contribution from latent heat because of water changes of phase is neglected, $\nu_\theta = k/(\rho c_p) = 2 \times 10^{-5}\,\mathrm{m^2\ s^{-1}}$ ($k = 2.5 \times 10^{-2}\,\mathrm{W\ m^{-1}\ K^{-1}}$, the thermal conductivity of air and $c_p = 1 \times 10^3\,\mathrm{J\ K^{-1}\ kg^{-1}}$, the specific heat at constant pressure) and Q_i^* is the net flux of radiation ($\mathrm{W\ m^{-2}}$) in the i-th direction.

The potential temperature and the absolute temperature are related by the Poisson's equation:

$$\theta = T\left(\frac{p_0}{p}\right)^{\frac{R}{c_p}}, \tag{1.6}$$

where p_0 is some reference pressure, typically $p_0 = 1000\,\mathrm{hPa}$. Furthermore, a relation between the virtual potential temperature, θ_v, and the potential temperature, θ, can be written as for (1.4):

$$\theta_v = \theta(1 + 0.61q). \tag{1.7}$$

Finally, the equation for the conservation of water vapor, i.e. $\rho_v = q\rho$, ρ, density of moist air, neglecting sink/source terms, is

$$\frac{\partial\rho_v}{\partial t} + u\frac{\partial\rho_v}{\partial x} + v\frac{\partial\rho_v}{\partial y} + w\frac{\partial\rho_v}{\partial z} = \nu_v\left(\frac{\partial^2\rho_v}{\partial x^2} + \frac{\partial^2\rho_v}{\partial y^2} + \frac{\partial^2\rho_v}{\partial z^2}\right), \tag{1.8}$$

ν_q, the molecular diffusivity of water vapor.

1.3 The Boussinesq approximation

The Boussinesq approximation states that: (i) the variations in the fluid density are neglected in the mass continuity equation (1.2) and in the equations of motion (1.1) with the exception of the buoyancy term in (1.1c); (ii) the contribution from pressure fluctuations to density fluctuations can be neglected (Mahrt, 1986).

Following Spiegel and Veronis (1960), let us consider a basic state of the PBL in which the atmosphere is at rest ($u = v = w = 0$) and write all thermodynamic variables as a superposition of the basic state (e.g. $\rho_0(z)$) and a perturbation due to fluid motion (e.g. $\widetilde{\rho}(x, y, z, t)$):

$$\rho(x, y, z, t) = \widetilde{\rho}(x, y, z, t) + \rho_0(z) \tag{1.9}$$

$$p(x, y, z, t) = \widetilde{p}(x, y, z, t) + p_0(z) \tag{1.10}$$

$$T_v(x, y, z, t) = \widetilde{T}_v(x, y, z, t) + T_{v0}(z). \tag{1.11}$$

From (1.1) and (1.3) (taking $u = v = w = 0$) we have that the basic state in in hydrostatic equilibrium:

$$\frac{dp_0}{dz} = -g\rho_0(z). \tag{1.12}$$

Defining the scale height

$$H \equiv \left| \frac{1}{\rho_0} \frac{d\rho_0}{dz} \right|^{-1}, \tag{1.13}$$

if h is the scale of vertical motions (the PBL depth), the Boussinesq approximation can be adopted if $h \ll H$. Furthermore, in this case, the relative variation of ρ_0 through the layer is small and we can further take $\rho_0 \approx \rho_{00} = \text{const.}$, where ρ_{00} is some representative value of the layer.

Furthermore, if the thermodynamic perturbations induced by the motion are much smaller than the basic state values (i.e. $|\widetilde{\rho}/\rho_0| \ll 1$, $|\widetilde{T}_v/T_{v0}| \ll 1$ and $|\widetilde{p}/p_0| \ll 1$) we can linearize the equation of state (1.3) as

$$\frac{\widetilde{\rho}}{\rho_0} \approx -\frac{\widetilde{T}_v}{T_{v0}} + \frac{\widetilde{p}}{p_0} \tag{1.14}$$

and, further

$$\frac{\widetilde{\rho}}{\rho_0} \approx -\frac{\widetilde{T}_v}{T_{v0}} \approx -\frac{\widetilde{\theta}_v}{\theta_{v0}}, \tag{1.15}$$

since pressure fluctuations are much smaller than temperature ones (Spiegel and Veronis, 1960). This means that the buoyancy term can be expressed in term of temperature fluctuations that can be measured more easily.

The equations of motion (1.1) under the Boussinesq approximation become

$$\frac{\partial u}{\partial t} + u\frac{\partial u}{\partial x} + v\frac{\partial u}{\partial y} + w\frac{\partial u}{\partial z} = -\frac{1}{\rho_0}\frac{\partial \widetilde{p}}{\partial x} + fv + \nu\left(\frac{\partial^2 u}{\partial x^2} + \frac{\partial^2 u}{\partial y^2} + \frac{\partial^2 u}{\partial z^2}\right) \tag{1.16a}$$

$$\frac{\partial v}{\partial t} + u\frac{\partial v}{\partial x} + v\frac{\partial v}{\partial y} + w\frac{\partial v}{\partial z} = -\frac{1}{\rho_0}\frac{\partial \widetilde{p}}{\partial y} - fu + \nu\left(\frac{\partial^2 v}{\partial x^2} + \frac{\partial^2 v}{\partial y^2} + \frac{\partial^2 v}{\partial z^2}\right) \tag{1.16b}$$

$$\frac{\partial w}{\partial t} + u\frac{\partial w}{\partial x} + v\frac{\partial w}{\partial y} + w\frac{\partial w}{\partial z} = -\frac{1}{\rho_0}\frac{\partial \widetilde{p}}{\partial z} + g\frac{\widetilde{\theta}_v}{\theta_{v0}} + \nu\left(\frac{\partial^2 w}{\partial x^2} + \frac{\partial^2 w}{\partial y^2} + \frac{\partial^2 w}{\partial z^2}\right). \tag{1.16c}$$

In (1.16), the further approximation $\rho_0 \approx \rho_{00} = \text{const.}$ and $\theta_{v0} \approx \theta_{v00} = \text{const.}$ can be adopted, where ρ_{00} and θ_{v00} are representative values for the whole boundary layer.

The continuity equation becomes that of an incompressible fluid:

$$\frac{\partial u}{\partial x} + \frac{\partial v}{\partial y} + \frac{\partial w}{\partial z} = 0. \tag{1.17}$$

The equation for the potential temperature is obtained from (1.5), taking $\theta_v(x, y, z, t) = \theta_0(z) + \widetilde{\theta}_v(x, y, z, t)$,

$$\frac{\partial \widetilde{\theta}}{\partial t} + u\frac{\partial \widetilde{\theta}}{\partial x} + v\frac{\partial \widetilde{\theta}}{\partial y} + w\frac{\partial \widetilde{\theta}}{\partial z} = -w\frac{d\theta_0}{dz} + \nu_\theta\left(\frac{\partial^2 \widetilde{\theta}}{\partial x^2} + \frac{\partial^2 \widetilde{\theta}}{\partial y^2} + \frac{\partial^2 \widetilde{\theta}}{\partial z^2} + \frac{d^2\theta_0}{dz^2}\right) \tag{1.18}$$

where the radiative flux-divergence term was neglected.

The equation for the water vapor (1.8) can be written for the specific humidity, $q \approx \rho_v/\rho_0$, dividing both sides for ρ_0:

$$\frac{\partial \widetilde{q}}{\partial t} + u\frac{\partial \widetilde{q}}{\partial x} + v\frac{\partial \widetilde{q}}{\partial y} + w\frac{\partial \widetilde{q}}{\partial z} = -w\frac{dq_0}{dz} + \nu_v\left(\frac{\partial^2 \widetilde{q}}{\partial x^2} + \frac{\partial^2 \widetilde{q}}{\partial y^2} + \frac{\partial^2 \widetilde{q}}{\partial z^2} + \frac{d^2 q_0}{dz^2}\right). \tag{1.19}$$

Finally we have

$$\theta_{v0} = \theta_0(1 + 0.61 q_0) \tag{1.20}$$

and

$$\widetilde{\theta}_v = \widetilde{\theta}(1 + 0.61\widetilde{q}) + 0.61(\widetilde{q}\theta_0 + q_0\widetilde{\theta}). \tag{1.21}$$

1.4 Mean and turbulent motion

It is common in turbulence research to separate the contribution of the mean motion from the turbulent one to the observed flow. This separation has some physical ground in the existence of a spectral gap in the spectrum of turbulent flows, which separates large scale (mean) motions from small scale (turbulent) ones. However, as pointed out by Wyngaard (2010), the mean flow should be regarded only as a statistical description of the observed one.

1.4.1 Reynolds averaging

With Reynolds averaging the contribution of the mean motion to the observed flow is separated from that of turbulence. At least, theoretically Reynolds averaging is an ensemble averaging: i.e. the average between many independent realizations of the same flow. Practically, ensemble averages are substituted by time or space averages. Also Reynolds, in 1895, introduced this method for volume average although using ensemble average rules.

In this way, each variable a can be decomposed as a sum of a mean value $\overline{a}$ and a fluctuation a':

$$a = \overline{a} + a' \quad \text{with} \quad \overline{\overline{a}} = \overline{a} \quad \text{and} \quad \overline{a'} = 0. \tag{1.22}$$

Furthermore

$$\overline{a + b} = \overline{a} + \overline{b} \quad \text{and} \quad \overline{ab} = \overline{a}\,\overline{b} + \overline{a'b'}, \tag{1.23}$$

where $\overline{a'b'}$ is the covariance between a and b. Only if two variables are uncorrelated, i.e. $\overline{a'b'} = 0$, the average of the product equals the product of the averages. As will be shown, covariances and variances have a key role in turbulence description.

The ensemble average commutes with the derivation:

$$\overline{\frac{\partial a}{\partial x}} = \frac{\partial \overline{a}}{\partial x}, \quad \overline{\frac{\partial a}{\partial y}} = \frac{\partial \overline{a}}{\partial y}, \quad \overline{\frac{\partial a}{\partial z}} = \frac{\partial \overline{a}}{\partial z}, \quad \text{and} \quad \overline{\frac{\partial a}{\partial t}} = \frac{\partial \overline{a}}{\partial t}. \tag{1.24}$$

This not holds rigorously when time or space averages are consider.

1.4.2 Equations for mean variables

Equations for mean variables are obtained expressing all variables as sums of averages and fluctuations in the set of equations under Boussinesq approximation and averaging them. The averaged equations are (1.16), (1.17), (1.18), (1.19) and (1.21).

The averaged Navier-Stokes equation (1.16) is

$$\frac{\partial \overline{u}_i}{\partial t} + \overline{u}_j \frac{\partial \overline{u}_i}{\partial x_j} = -\frac{1}{\rho_{00}} \frac{\partial \overline{p}}{\partial x_i} + g \frac{\overline{\theta}_v}{\theta_{v00}} \delta_{i3} + f \varepsilon_{ij3} \overline{u}_j - \frac{\partial \overline{u'_j u'_i}}{\partial x_j} + \nu \frac{\partial^2 \overline{u}_i}{\partial x_j \partial x_j} \quad \text{for} \quad i = 1, 2, 3 \tag{1.25}$$

where $x_1 = x$, $x_2 = y$, $x_3 = z$, $u_1 = u$, $u_2 = v$ and $u_3 = w$, the convention of sum over repeated indexes is adopted and all mean thermodynamic variables are deviations from the motionless hydrostatic basic state (i.e. $\overline{\theta}_v \equiv \widetilde{\overline{\theta}_v}$ and $\overline{p} \equiv \widetilde{\overline{p}}$). To obtain (1.25) the incompressibility of turbulent fluctuations (1.27) is used.

The covariances $\overline{u'_j u'_i}$ appeared in (1.25) can be interpreted as the kinematic flux of the i-th momentum component along the j-th direction due to turbulent motion, or vice versa (e.g. Stull (1988)); $\tau_{ij} = -\rho_{00} \overline{u'_i u'_j}$ is called Reynolds stress.

From (1.17), the incompressibility of mean motion

$$\frac{\partial \overline{u}_j}{\partial x_j} = 0. \tag{1.26}$$

and fluctuations

$$\frac{\partial u'_j}{\partial x_j} = 0 \tag{1.27}$$

is readily obtained.

Neglecting the radiative flux-divergence term, the equation of mean potential temperature is obtained from (1.5) using again (1.27):

$$\frac{\partial \overline{\theta}}{\partial t} + \overline{u}_j \frac{\partial \overline{\theta}}{\partial x_j} = -\overline{u}_3 \frac{d\theta_0}{dx_3} - \frac{\partial \overline{u'_j \theta'}}{\partial x_j} + \nu_\theta \frac{\partial^2 \overline{\theta}}{\partial x_j \partial x_j} + \nu_\theta \frac{d^2 \theta_0}{dx_3^2} \tag{1.28}$$

In this case, the divergence of the turbulent flux of potential temperature in the j-th direction, $\overline{u'_j \theta}$, is present; the turbulent flux of sensible heat being $\rho_{00} c_p \overline{u'_j \theta}$.

The conservation equation for the mean specific humidity, $\overline{q}$, from (1.19), is

$$\frac{\partial \overline{q}}{\partial t} + \overline{u}_j \frac{\partial \overline{q}}{\partial x_j} = -\overline{u}_3 \frac{dq_0}{dx_3} - \frac{\partial \overline{u'_j q'}}{\partial x'_j} + \nu_v \frac{\partial^2 \overline{q}}{\partial x_j \partial x_j} + \nu_v \frac{d^2 q_0}{dx_3^2}, \tag{1.29}$$

where $\rho_{00} \overline{u'_j q'}$ is the turbulent flux of water vapor in the j-th direction.

The set is closed by the expression for the mean virtual potential temperature (from (1.7)):

$$\overline{\theta}_v \approx \overline{\theta}(1 + 0.61\overline{q}) + 0.61(\theta_0 \overline{q} + \overline{\theta} q_0) \tag{1.30}$$

supposing that $|\overline{\theta' q'}| \ll \overline{\theta}\overline{q}$.

The set of equations (1.25), (1.26), (1.28), (1.29) and (1.30) is unclosed since equations for turbulent fluxes (covariances) are also needed. However, equations for second order moments require equations for third order moments, and so on. The problem is then mathematical intractable, unless higher order moments are expressed as functions of lower ones, i.e., unless closures are found.

1.4.3 The equation for the turbulent kinetic energy

Among all the prognostic equations for second order moments (variances and covariances), a key role is played by that for the turbulent kinetic energy (TKE) $\overline{e} = (\overline{u'^2} + \overline{v'^2} + \overline{w'^2})/2$ (e.g. Stull (1988)):

$$\underbrace{\frac{\partial \overline{e}}{\partial t}}_{\text{i}} + \underbrace{\overline{u}_j \frac{\partial \overline{e}}{\partial x_j}}_{\text{ii}} = \underbrace{-\overline{u'_i u'_j} \frac{\partial \overline{u}_i}{\partial x_j}}_{\text{iii}} + \underbrace{\frac{g}{\theta_{v00}} \overline{u'_3 \theta'_v}}_{\text{iv}} - \underbrace{\frac{\partial \overline{u'_j e}}{\partial x_j}}_{\text{v}} - \underbrace{\frac{1}{\rho_{00}} \frac{\partial \overline{u'_j p'}}{\partial x_j}}_{\text{vi}} - \underbrace{\varepsilon}_{\text{vii}}. \tag{1.31}$$

where $e = (u'^2 + v'^2 + w'^2)/2$ and

$$\varepsilon = \nu \overline{\frac{\partial u'_i \partial u'_i}{\partial x_j \partial x_j}}. \tag{1.32}$$

The physical meaning of each term is explained below:

i. *local storage* of TKE.

ii. TKE *advection* by mean flow.

iii. mechanical or *shear production* term: the kinematic flux of momentum $\overline{u_i' u_j'}$ is usually in the opposite direction of the gradient $\partial u_i/\partial x_j$ making this term positive. This is a source term in TKE equation and a sink one in the equation for the kinetic energy of the mean flow.

iv. *buoyant production* or *consumption*: when $\overline{u_3'\theta'} > 0$, potential energy is transformed into kinetic one and the strength of turbulence increasing (convective boundary layer); when $\overline{u_3'\theta'} < 0$, the opposite is true (stable boundary layer).

v. *turbulent transport* of TKE.

vi. *pressure correlation* term: redistribution of TKE by pressure perturbations.

vii. *viscous dissipation*: TKE is transformed into heat at the smallest scales, this term is always a sink of TKE:. This means that TKE is conserved, i.e. the PBL remains turbulent, only if generation or transport processes are acting.

A simplified expression for the TKE budget (1.32) can be obtained assuming horizontal homogeneity, no subsidence and aligning the coordinate system with the mean wind, assuming no wind rotation with height, (Stull, 1988):

$$\frac{\partial \overline{e}}{\partial t} = -\overline{u'w'}\frac{\partial \overline{u}}{\partial z} + \frac{g}{\theta_{v00}}\overline{w'\theta_v'} - \frac{\partial \overline{w'e}}{\partial z} - \frac{1}{\rho_{00}}\frac{\partial \overline{w'p'}}{\partial z} - \varepsilon. \tag{1.33}$$

This is the equation usually adopted for the surface layer (lowest 10% of the boundary layer) over flat and homogeneous terrain.

1.5 The surface layer

We consider the simplest case of a stationary flow over an infinite, flat, homogeneous surface. In this ideal conditions, the properties of the flow are functions of the height above the surface, z, only. These conditions are better encountered in the surface-layer: the atmospheric layer that extends from above the grass up to about 10% of the PBL height. In this layer, gradients of mean variables are usually large, suggesting the possibility to express turbulent fluxes as functions of mean gradients.

The Reynolds number, $\mathrm{Re} = UL/\nu$, where U and L are the velocity and the length scales of the flow, and ν is the kinematic viscosity, expresses the ratio between inertial and viscous forces. For $\mathrm{Re} \gtrsim 2000$, inertia dominates on viscous damping and the flow becomes fully turbulent. For the typical surface layer scales, $L = 10 \div 100\,\mathrm{m}$, $U = 1 \div 10\,\mathrm{m\ s^{-1}}$ and $\nu \sim 10^{-5}\,\mathrm{m^2\ s^{-1}}$, $\mathrm{Re} = 10^6 \div 10^8$. For this reason, viscous terms will always be neglected hereafter in the equations for the mean flow.In the surface layer $\mathrm{Ro} = U/(fL) \sim 10^3$ and then also the effect of earth's rotation is usually negligible.

The constancy of fluxes can be used to determine the surface layer height (Monin and Obukhov, 1954). Consider a reference system with the x-axis aligned with the mean wind at the earth's surface (slightly above the grass height), i.e. $\overline{v}(0) = 0$. Furthermore, assume horizontal homogeneity and stationarity. Under these conditions the equations of motion

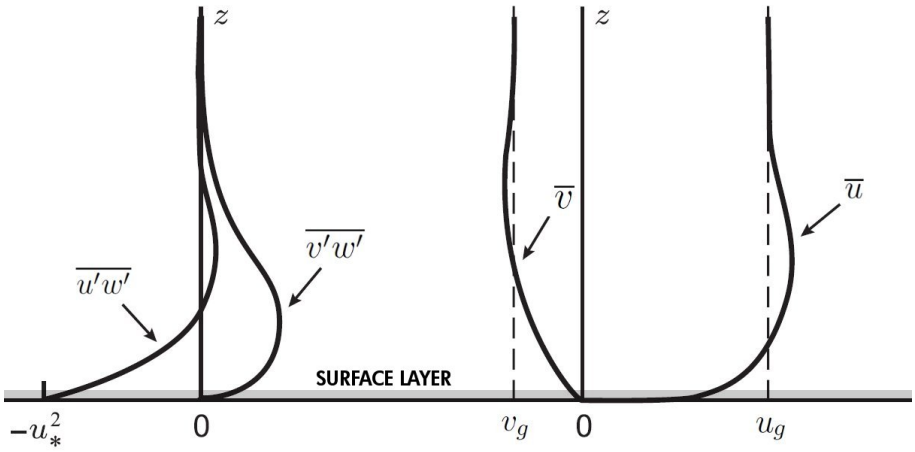

Figure 1.3: Qualitative behaviour of kinematic momentum fluxes and mean wind speed for the near-neutral PBL (adapted from Wyngaard (2010)). The dashed area indicates approximately the surface layer depth.

(1.25) becomes

$$\frac{d\overline{u'w'}}{dz} = f(\overline{v} - v_g) \tag{1.34}$$

$$\frac{d\overline{v'w'}}{dz} = f(u_g - \overline{u}) \tag{1.35}$$

$$\frac{1}{\rho_{00}}\frac{\partial \overline{p}}{\partial z} = g\frac{\overline{\theta}_v}{\theta_{v00}}, \tag{1.36}$$

where the geostriphic wind components

$$u_g \equiv -\frac{1}{f\rho_{00}}\frac{\partial \overline{p}}{\partial y} \quad \text{and} \quad v_g \equiv \frac{1}{f\rho_{00}}\frac{\partial \overline{p}}{\partial x} \tag{1.37}$$

were introduced. We have $d\overline{v}/dz = 0$ if $d^2\overline{u'w'}/dz^2 = 0$, thus, the boundary layer cannot be stationary and unidimensional (no wind rotation) if the along-wind kinematic momentum flux $-\overline{u'w'}$ varies (not linearly) with height. In the surface layer, intended as constant flux layer, wind rotation with height can be neglected.

Integrating (1.34) in z, from above the grass (i.e. $z \simeq 0$) up to $z = h$ we have

$$u_*^2 - \tau_x(h) = \int_0^h f(\overline{v} - v_g)dz < \int_0^h f|v_g|dz = hf|v_g| \tag{1.38}$$

with $\tau_x \equiv -\overline{u'w'}$ with $\tau_x(0) \equiv u_*^2$, where u_* is the *friction velocity*. From fig. 1.3 we see that $\overline{v}$ have the same sign of v_g in the surface layer and that $|\overline{v}| < |v_g|$. Then

$$u_*^2 - \tau_x(h) < hf|v_g|. \tag{1.39}$$

Imposing that the relative variation of momentum fluxes remains below a threshold a, i.e.

$$\frac{u_*^2 - \tau_x(h)}{u_*^2} \leq a \tag{1.40}$$

leads to an expression for the maximum height above ground for which (1.40) is satisfied, i.e. an estimation of the surface layer depth:

$$h = \frac{a u_*^2}{f|v_g|}. \tag{1.41}$$

From observations (Monin and Obukhov (1954), Liang et al. (2014) and also from the CCT dataset, section 3.2)

$$\frac{u_*}{|v_g|} \sim 0.05,$$

from which

$$h \sim 2.5 \times 10^{-3} a \frac{|v_g|}{f}$$

and taking $a = 20\%$, $|v_g| \sim 10\,\mathrm{m\ s^{-1}}$ and $f \sim 10^{-4}\,\mathrm{s^{-1}}$ we have

$$h \sim 50\,\mathrm{m}.$$

As can be seen in fig. 1.3, steepest vertical variations of turbulent fluxes and of wind speed occur just near the ground. However, the surface layer depth, h, is much smaller than the PLB height, H, (defined, for example as the height at which $\overline{u'w'}$ reverse its sign). Then, because

$$\frac{d\overline{u'w'}}{dz} \sim \frac{u_*^2}{H} \quad \text{and} \quad \frac{d\overline{w'\theta_v'}}{dz} \sim \frac{Q_0}{H}, \tag{1.42}$$

with $Q_0 \equiv \overline{w'\theta_v'}(0)$, the relative variations of turbulent fluxes in the surface layer are

$$\frac{\tau_x - u_*^2}{u_*^2} \sim \frac{\overline{w'\theta_v'} - Q_0}{Q_0} \sim \frac{h}{H}. \tag{1.43}$$

Variations below 20% corresponds to $h/H \sim 20\%$.

1.6 Mixing length and K-theory closure

Especially where gradients of mean variables are large, as is in the surface layer, it is quite natural to try to relate turbulent fluxes to mean gradients. This leads to the idea of turbulent diffusion, in analogy with molecular diffusion, acting to reduce mean gradients. As in molecular diffusion molecules travel undisturbed until they collide with another molecule, in turbulent diffusion, a fluid parcel travel conserving its properties (momentum, temperature, humidity, etc.) until it merges with the surrounding fluid.

The length scale for which the fluid particle travels undisturbed is the equivalent of the mean free path in molecular diffusion. The concept of a length scale for turbulent mixing was independently developed by Taylor and Prandtl, at the beginning of 1900 (Wyngaard, 2010), although, some years later, Taylor became critical on the physical validity of this model.

For example, the fluctuation of the horizontal wind speed u because of a vertical displacement, l' ($l' > 0$ upward), can be expressed as

$$u' \approx -l' \frac{\partial \overline{u}}{\partial z}. \tag{1.44}$$

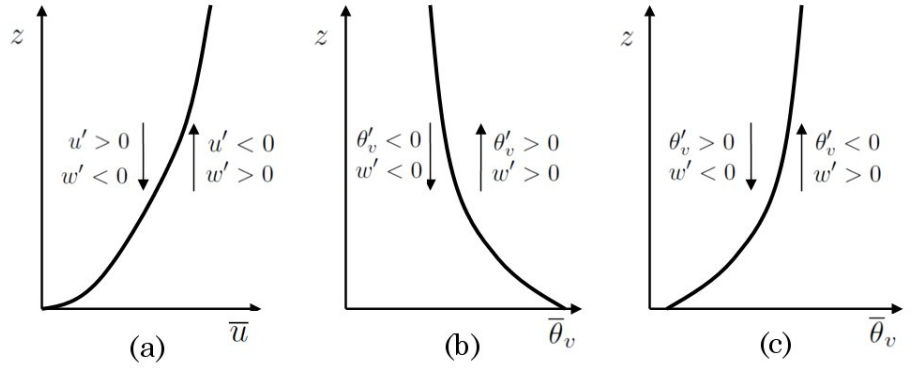

Figure 1.4: Correlation between the fluctuations of wind speed and vertical velocity (a) and between the virtual potential temperature and the vertical velocity for unstable (b) and stable (c) stratification.

Multiplying (1.44) for w' and averaging we obtain an expression the kinematic momentum flux

$$\overline{u'w'} \approx -\overline{l'w'}\frac{\partial \overline{u}}{\partial z} \equiv -K_m \frac{\partial \overline{u}}{\partial z}. \tag{1.45}$$

K_m is called *eddy diffusivity*, from which the name of "K-theory" of this closure. Furthermore, $K_m \geq 0$ since $\overline{w'l'} \geq 0$, allowing only for counter-gradient fluxes. It is defined in analogy with molecular diffusivity (kinematic viscosity). However, K_m is not a property of the fluid, but a variable characteristic of the flow, depending on both its dynamics and geometry.

If a correlation exists between u' and w', i.e. if $\overline{u'w'} \neq 0$,

$$w' \approx \alpha \operatorname{sgn}\left(\frac{\partial \overline{u}}{\partial z}\right) u'$$

and then

$$\overline{u'w'} \approx -\alpha \operatorname{sgn}\left(\frac{\partial \overline{u}}{\partial z}\right)\overline{u'^2} = -\alpha \overline{l'^2}\left|\frac{\partial \overline{u}}{\partial z}\right|\frac{\partial \overline{u}}{\partial z}, \tag{1.46}$$

where (1.44) was used. Comparing (1.46) with (1.45) we have

$$K_m \approx \alpha \overline{l'^2}\left|\frac{\partial \overline{u}}{\partial z}\right| \equiv l_m^2 \left|\frac{\partial \overline{u}}{\partial z}\right|, \tag{1.47}$$

where l_m is the *mixing length* (for momentum) directly proportional to the mean size of eddies, $\overline{l'^2}^{1/2}$, the constant of proportionality, $\alpha^{1/2}$, empirically determined from experimental data. It will be shown, that surface layer scales of velocity and length are u_*, the friction velocity, and z, the height above ground. Then, from dimensional arguments we have that, in the surface-layer

$$l_m \sim z \quad \text{and} \quad K_m \sim u_* z, \tag{1.48}$$

whit correction factors that must be introduced to account for stability.

Flux-gradient relationships can be formulated also for scalars, such as virtual potential temperature and specific humidity

$$\overline{w'\theta'_v} = -K_h \frac{\partial \overline{\theta}_v}{\partial z} \tag{1.49}$$

$$\overline{w'q'} = -K_q \frac{\partial \overline{q}}{\partial z}, \tag{1.50}$$

where it is sometimes assumed that (Obukhov, 1971)

$$K_q \sim K_h \sim K_m,$$

although experimental data show usually a more complicated behaviour.

In fig. 1.4, a representation of the mechanism generating downward momentum fluxes (a) and upward or downward heat fluxes for unstable (b) and stable (c) stratification, respectively, is given. It must be noted, however, that this picture is only *statistically* true, i.e., it is true *on average*. Indeed, the products $u'w'$ and $w'\theta'_v$ can have instantaneously also the "wrong" sign (as indeed occurs for real observations) and only on average counter-gradient fluxes should be observed.

The assumptions underling the K-theory (or *classical* theory of atmospheric turbulence) are (Obukhov, 1971):

1. while moving unmixed with the surrounding air, transported property is conserved by the fluid parcel;

2. the property is globally conserved during the mixing of the fluid parcel with the surrounding air;

3. the transported property is *passive*, i.e. its mixture does not influence the development of turbulence.

This condition can be more or less satisfied by material contaminants (smoke, dust, trace elements) that are indeed termed *passive tracers*. However, in particular the first and the third, are far from being strictly fulfilled by momentum and heat. This is the cause of the non-perfect coincidence between eddy diffusivities for momentum, heat and passive tracers (Obukhov, 1971).

1.7 Monin-Obukhov similarity theory

Much of the present understanding of the atmospheric surface layer was obtained in the framework of Monin-Obukov similarity theory (MOST). Similarity theories are based on dimensional analysis. The key variables governing the phenomenon are individuated and combined into dimensionless groups, the Buckingham Pi Theorem (e.g. Stull, 1988) prescribes how to do it. Finally universal laws relating dimensionless groups are derived from observations.

In 1954, Monin and Obukhov proposed that turbulence in the quasi-stationary and horizontally homogeneous surface layer was governed by four key variables: the height above ground, z; the friction velocity, $u_* = |\overline{u'w'}(0)|^{1/2}$; the temperature flux at the surface, $Q_0 = \overline{w'\theta'_v}(0)$; the buoyancy parameter $\beta = g/\theta_{v00}$.[1] MOST is a flux-based similarity, with fluxes evaluated at the earth's surface.

When properly normalized with combinations of the four key variables, turbulence quantities should be universal functions of z/L only, where

$$L \equiv -\frac{u_*^3}{\kappa\beta Q_0} \tag{1.51}$$

[1] In the original paper (Monin and Obukhov, 1954), the absolute temperature, instead of the virtual potential temperature, was used in both the definition of the temperature flux and the buoyancy parameter, although, today, definitions with the virtual potential temperature are most used.

is the Obukhov lenght, firstly introduced by the Russian physicist A. M. Obukhov in 1946 (Obukhov, 1971). For historical reasons, in the definition (1.51) enters the von Kármán constant, κ, that usually is assumed equal to 0.4 (Högström, 1996).

The physical interpretation of L is that of a characteristic scale of the depth of the *dynamical sublayer* (Obukhov, 1971), where the influence of thermal stratification is small and turbulence is mechanically generated by the wind shear. The Obukhov length can be both positive or negative, depending on the sign of the temperature flux. In the convective surface layer, $Q_0 > 0$ and $L < 0$; in the stable surface layer, $Q_0 < 0$ and $L > 0$; in almost neutral conditions $Q_0 \simeq 0$ and L becomes large with both positive or negative sign, i.e. $L \to \pm\infty$. For this reason, z/L is called the Monin-Obukhov *stability parameter*.

The M-O stability parameter appears also in the non-dimensional form of the TKE equation, obtained dividing (1.52) by $u_*^3/(\kappa z)$:

$$\frac{u_*^3}{\kappa z}\frac{\partial \overline{e}}{\partial t} = \phi_m - \frac{z}{L} + \phi_t - \phi_\varepsilon, \tag{1.52}$$

where

$$\phi_m \equiv \frac{\kappa z}{u_*}\frac{d\overline{u}}{dz} \tag{1.53}$$

is the normalized shear-production term but it is also the dimensionless wind shear; z/L expresses the effect of buoyancy production ($z/L < 0$, unstable case) or consumption ($z/L > 0$, stable case) of TKE; ϕ_t and ϕ_ε are the dimensionless transport (both from vertical velocity and pressure fluctuations) and the dimensionless viscous dissipation terms, respectively. For MOST, ϕ_m, ϕ_t and ϕ_ε are all universal functions of z/L.

In analogy with (1.53), the dimensionless temperature gradient is defined as

$$\phi_h \equiv \frac{\kappa z}{\theta_*}\frac{d\overline{\theta}_v}{dz} \tag{1.54}$$

where

$$\theta_* \equiv -\frac{Q_0}{u_*},$$

with $\theta_* > 0$ in stable conditions and $\theta_* < 0$ in unstable ones.

The similarity function for the specific humidity is

$$\phi_q \equiv \frac{\kappa z}{q*}\frac{d\overline{q}}{dz} \tag{1.55}$$

where

$$q_* \equiv \frac{-\overline{w'q'}}{u_*}.$$

Comparing (1.53), (1.54) and (1.55) with (1.45), (1.49) and (1.50) we have

$$K_m\phi_m = K_h\phi_h = K_q\phi_q = \kappa z u_*, \tag{1.56}$$

and, from (1.47),

$$l_m\phi_m = l_h\phi_h = l_q\phi_q = \kappa z. \tag{1.57}$$

1.8 The wind profile in the surface layer

MOST does not predict the functional form of universal functions $\phi_(z/L)$ which must instead be derived from experiments. For ϕ_m, the only constraints is that the logarithmic profile solution must be obtained as the surface-layer approaches near neutral conditions (i.e. $|z/L| \to 0$):

$$\phi_m(z/L = 0) = 1. \tag{1.58}$$

That the fluid velocity over an infinite flat and rough surfaces increases logarithmically with the distance from the surface for non-stratified fluids is predicted by Prandtl's similarity theory, which Monin and Obukhov extended to the case of stratified fluids (Monin and Obukhov, 1954).

From (1.53) we have

$$\frac{d\overline{u}}{dz} = \frac{u_*}{\kappa z}\phi_m\left(\frac{z}{L}\right) \tag{1.59}$$

that, integrated from z_{0m}, defined such that $\overline{u}(z_{0m}) = 0$, to z,

$$\overline{u}(z) = \frac{u_*}{\kappa L}\int_{z_{0m}/L}^{z/L} \phi_m(\zeta)\frac{d\zeta}{\zeta} \tag{1.60}$$

yields the wind profile

$$\overline{u}(z) = \frac{u_*}{\kappa}\left(\ln\left(\frac{z}{z_{0m}}\right) + \psi_m\left(\frac{z}{L}\right) - \psi_m\left(\frac{z_{0m}}{L}\right)\right), \tag{1.61}$$

where we remember that both u_* and L are constant and was defined the function

$$\psi_m(\zeta) \equiv \int_0^{\zeta} \frac{\phi_m(x) - 1}{x} dx \tag{1.62}$$

which is the deviation from the logarithmic profile. In stable conditions (i.e. $z/L \geq 0$), $\phi_m \geq 1$ (at leas for all similarity functions derived over flat and homogeneous terrain) and ψ_m is a non-negative monotonically increasing function of z/L with

$$\psi_m(0) = 0. \tag{1.63}$$

This express the fact that in the stably stratified surface layer the wind profile is super-logarithmic (fig. 1.5(b)). The opposite is true for the unstable surface layer for which the wind profile is sub-logarithmic. However, this not means that the *dimensional* wind is usually stronger in the stable surface layer since u_* is smaller in stable conditions. Indeed, stable conditions are usually characterized by lighter winds.

Since (1.61) should be used only for $z \gg z_{0m}$ and z_{0m}/L does not differ significantly from zero (if $L \sim z_{0m}$, a surface-layer does not exist) we can take

$$\overline{u}(z) \approx \frac{u_*}{\kappa}\left(\ln\left(\frac{z}{z_{0m}}\right) + \psi_m\left(\frac{z}{L}\right)\right). \tag{1.64}$$

The *aerodynamic roughness length*, z_{0m}, is the height at which the surface layer wind speed profile (i.e. that computed from (1.61)) goes to zero. This however does not mean that the wind speed is zero for $z \leq z_{0m}$ but only that, very near to the ground, where the influence of individual roughness elements is strong (i.e. in the *roughness sublayer*), the surface-layer profile is no longer valid.

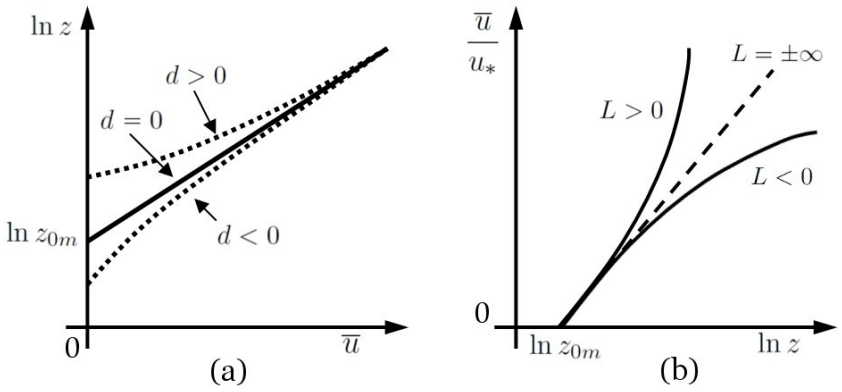

Figure 1.5: (a) The effect of a displacement height on the logarithmic wind profile; (b) qualitative behaviour of the wind profile for stable ($L > 0$), neutral ($L = \pm\infty$) and unstable ($L < 0$) conditions.

If the surface-layer profile can be extended also above the surface layer (i.e. for $|z/L| \gg 1$) is still an open question (Caporaso et al., 2013). It is a matter of fact, however, that proposed formulations for ϕ_m diverge for $z/L \gtrsim 1$ indicating limits in the validity of MOST. The roughness length is not directly related to the height of the roughness elements although it depend on the type of elements and their disposition. More specifically, z_{0m} is a property of the surface and not of the flow or, being independent on stability, wind speed or stress (Stull, 1988). Exception however exist, as for the sea-surface that changes under the effect of wind though the formation of waves. Tables containing typical values of z_{0m} for many surface types exist (e.g. Stull, 1988, p. 380) although for each site this value should be determined from observations. From Stull's table, typical values of z_{0m} ranges from about 0.1 mm for calm open sea or flat snow-covered ground up to about 100 m above mountainous areas; for grass or crops, z_{0m} of the order 1–10 cm are usual.

For tall and closely packed elements, such as tree in a forest or buildings in urban areas, the height above ground, the top of these elements acts like a displaced surfaces. In this case, the vertical scale of the surface layer, which eventually forms only above the canopy (above elements' top) is no longer z, the height above ground, but $z - d$, the height above the displaced surface. Indeed, d is usually called the *displacement height*.

From (1.64), the wind profile in the surface layer above a canopy in is expressed as

$$\overline{u}(z) = \frac{u_*}{\kappa}\left(\ln\left(\frac{z-d}{z_{0m}}\right) - \psi_m\left(\frac{z-d}{L}\right)\right) \tag{1.65}$$

where u_* and L are now evaluated from turbulent fluxes measured slightly above the canopy height and (1.65) holds for $z - d \gg z_{0m}$, (1.65). In fig. 1.5(a) is showed the effect of a displacement height on the neutral wind profile

$$\overline{u}(z) = \frac{u_*}{\kappa}\ln\left(\frac{z-d}{z_{0m}}\right). \tag{1.66}$$

when the wind speed is plotted against the logarithm of the height above ground, $\ln z$, without the correction for d. The case $d < 0$ corresponds to an underestimation of z, which now takes into account a displacement height which is however too large.

1.9 An overview on wind speed similarity functions for stable conditions

MOST predicts that, for the quasi-stationary and horizontally homogeneous surface layer, the dimensionless wind speed vertical gradient, ϕ_m, should be a universal function of z/L. However, it does not predict the behaviour of ϕ_m, beyond the neutral limit $\phi_m(z/L = 0) = 1$, that must be determined from experiments. Because of universality, data for different experiments should collapse on the same curve. In this section, the similarity functions from different experiments in the stable surface-layer (i.e. for $z/L > 0$) are presented. The overview has not the pretense of completeness, although most used similarity functions or those showing peculiar behaviours are present.

For small z/L, ϕ_m can be approximated with a linear function (Monin and Obukhov, 1954). Indeed, expanding ϕ_m in Taylor's series around the neutral case (i.e. $z/L = 0$) and retaining only the first two terms we have

$$\phi_m \approx 1 + \beta_m \frac{z}{L} \quad \text{for} \quad z/L < 1, \tag{1.67}$$

where β_m must be determined experimentally. Expression (1.67) leads to the log-linear wind profile (see eq. (1.64))

$$\overline{u}(z) = \frac{u_*}{\kappa}\left(\ln\left(\frac{z}{z_{0m}}\right) + \beta_m \frac{z}{L}\right). \tag{1.68}$$

From observations collected during the 1968 Kansas experiment (Businger et al., 1971; Haugen et al., 1971), Businger et al. (1971) proposed the linear expression

$$\phi_m = 1 + 4.7\frac{z}{L} \quad \text{for} \quad 0 \leq z/L \lesssim 1. \tag{1.69}$$

However, few observations were available for $z/L > 0.5$ and the scatter of data allowed for $4.5 \lesssim \beta_m \lesssim 5.0$ (Businger et al., 1971). They also noted a rapidly decrease in the slope of ϕ_m at the crossing of the neutral point (i.e. $z/L = 0$).

The 1968 Kansan was the first experiment relying on direct measurements of turbulence by mean of sonic anemometers. The experimental site was a Kansas' flat farmland covered by wheat stubble (Haugen et al., 1971). Businger et al. (1971) used in their analysis a value of 0.35 for κ, the von Kármán constant. However, the linear law proposed by Businger et al. (1971) was more or less confirmed by later experiments over flat terrain, at least for $z/L \lesssim 1$. Equation (1.69) is represented by the solid red curve in fig. 1.6. It must be noted that in fig. 1.6 all similarity functions are plotted up to $z/L = 100$ although most of the formulations were derived for a smaller stability range.

Högström (1988) derived a modified expression for (1.69) assuming $\kappa = 0.40$:

$$\phi_m = 1 + 6.0\frac{z}{L}. \tag{1.70}$$

He found, however, that observations from Lövsta site, Sweden (Högström, 1988), were better described by the relation

$$\phi_m = 1 + 4.8\frac{z}{L} \quad \text{for} \quad 0 \leq z/L \lesssim 0.5 \tag{1.71}$$

which is obtained modifying Dyer (1974) curve and that does not differ significantly from (1.69). For $z/L \gtrsim 0.5$, although few data points were present, he observed an indication of level-off for ϕ_m.

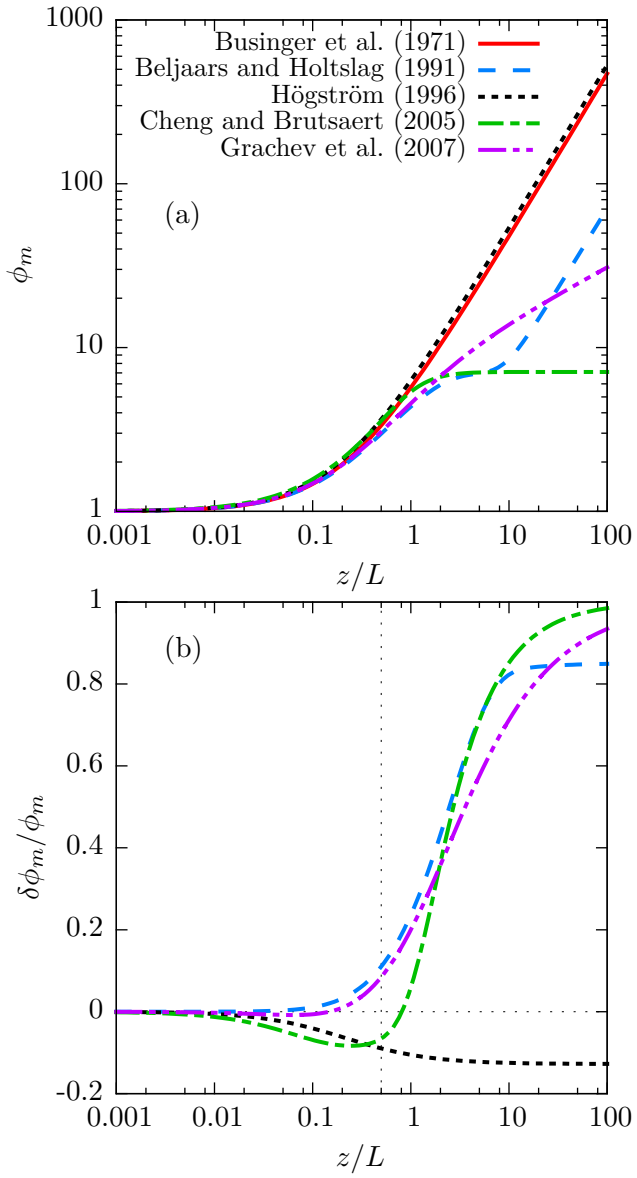

Figure 1.6: (a) Similarity functions for the dimensionless wind speed gradient proposed by different authors.(b) Relative deviations of formulations from the Businger et al. (1971) linear law (see eq. (1.76)).

From an averaging between similarity functions proposed up to that time (although that from Beljaars and Holtslag (1991) was not included) Högström (1996) recommended the expression

$$\phi_m = 1 + 5.3\frac{z}{L} \quad \text{for} \quad 0 \leq z/L \lesssim 0.5, \tag{1.72}$$

that is represented bu the black dotted curve in fig. 1.6(a).

From wind speed observations obtained at Cabauw, The Netherlands, Holtslag (1984) and Holtslag and De Bruin (1988)[2] proposed the function

$$\phi_m = 1 + a\frac{z}{L} + b\frac{z}{L}\left(1 + c - d\frac{z}{L}\right)e^{-d\frac{z}{L}} \quad \text{for} \quad 0 \leq z/L \lesssim 10 \tag{1.73}$$

with $a = 1$, $b = 0.667$, $c = 5.0$ and $d = 0.35$. The value of a, originally of 0.7, was chosen by Beljaars and Holtslag (1991) to account for a critical flux Richardson number of 1 (see section 1.10). We have

$$\phi_m \sim 1 + 5.1\frac{z}{L} \quad \text{for} \quad \frac{z}{L} \to 0 \quad \text{and} \quad \phi_m \sim \frac{z}{L} \quad \text{for} \quad \frac{z}{L} \to \infty.$$

Equation (1.73) is the blue dashed line in fig. 1.6(a).

Cheng and Brutsaert (2005a), from CASES99 (Cooperative Atmosphere- Surface Exchange Study-99) data (Kansas), proposed the similarity function

$$\phi_m = 1 + a\frac{\zeta + \zeta^b(1+\zeta^b)^{\frac{1-b}{b}}}{\zeta + (1+\zeta^b)^{\frac{1}{b}}} \quad \text{for} \quad 0 \leq \zeta \lesssim 5, \tag{1.74}$$

where $\zeta \equiv z/L$, $a = 6.1$ and $b = 2.5$, such that

$$\phi_m \sim 1 + a\zeta = 1 + 6.1\zeta \quad \text{for} \quad \zeta \to 0 \quad \text{and} \quad \phi_m \sim 1 + a = 7.1 \quad \text{for} \quad \zeta \to \infty.$$

Then (1.74) is a smooth interpolation between two behaviour: a linear behaviour such that of the modified-Kansas68 (1.70) in the near-neutral and weakly stable range ($\zeta \ll 1$); a constant behaviour with a value of 7 for very stable conditions ($\zeta \gg 1$). A transition regime is present around $\zeta = 1$, which assumes the role of a critical stability value. Equation (1.74) is the green dot-dashed line in fig. 1.6(a).

From the dataset of SHEBA (Surface Heat Budget of the Arctic Ocean) experiment, conducted over the arctic pack, Grachev et al. (2007b) proposed the similarity function

$$\phi_m = 1 + \frac{a\zeta(1+\zeta)^{1/3}}{1 + b\zeta} \quad \text{for} \quad 0 \leq \zeta \lesssim 100 \tag{1.75}$$

with $a = 5$ and $b = a/6.5 = 0.77$, which is a smooth interpolation between a linear behaviour in the weakly stable range

$$\phi_m \approx 1 + 5\zeta \quad \text{for} \quad \zeta \ll 1$$

and a $\zeta^{1/3}$-behaviour in the very stable range

$$\phi_m \approx 6.5\zeta^{1/3} \quad \text{for} \quad \zeta \gg 1.$$

[2]This is the reference reported in the paper of Beljaars and Holtslag (1991) although it apparently wrong in the references list. Unfortunately, this paper was not found.

The $\zeta^{1/3}$-behaviour in very stable conditions suggest the existence of a u_*-*less* regime, in which wind shear does not depend anymore on friction velocity (Grachev et al., 2007b). This behaviour arise because of self-correlation, since $\phi_m \propto u_*^{-1}$ and $\zeta \propto u_*^{-3}$. Also data presented by Yagüe et al. (2006) have about the same behaviour for $\zeta > 1$. It must be noted that data considered by Grachev et al. (2007b) reached very high stabilities compared to other experiments. Equation (1.75) is shown as the purple dash-dot-dot line in fig. 1.6(a).

In fig. 1.6(a), all presented stability functions are plotted together, also beyond the stability range for which they was originally proposed. Figure 1.6(b), show minus the relative deviation of the considered formulations from the original 1968-Kansas linear law proposed by Businger et al. (1971), i.e.

$$\frac{\delta\phi_m}{\phi_m} = \frac{\phi_m^{\mathrm{B71}} - \phi_m^{\mathrm{X}}}{\phi_m^{\mathrm{B71}}} \tag{1.76}$$

where ϕ_m^{B71} is eq. (1.69) and ϕ_m^{X} can be eq. (1.72) from Högström (1996), eq. (1.73) from Beljaars and Holtslag (1991), eq. (1.74) from Cheng and Brutsaert (2005a) or eq. (1.75) from Grachev et al. (2007b). The style of each curve in fig. 1.6(a) is retained in fig. 1.6(b).

For $z/L \lesssim 0.5$, the linear dependence of ϕ_m on z/L, over leveled terrain, is well established, with deviations between formulations smaller than 10%, with a value for $\beta_m \simeq 5$. Deviations remain below about 20% up to $z/L \simeq 1$. Beyond, sub-linear behaviour were observed (Beljaars and Holtslag, 1991; Cheng and Brutsaert, 2005a; Forrer and Rotach, 1997; Grachev et al., 2007b; Howell and Sun, 1999; Yagüe et al., 2006) but results from different experiments hardly collapse on the same curve. This may indicate a failure of MOST for very stable conditions (i.e. $z/L > 1$). It must be noted however that momentum fluxes become small in very stable conditions, making their measure more difficult and increasing the effect of instrumental errors on obtained results.

1.10 The local similarity theory

The application of MOST is limited to the surface layer, where turbulent fluxes are almost constant with height. However, for very stable conditions, this layer may be very shallow, occupying the first few meters above ground, or even may not exist. This means that, especially in the stable case, a theory to describe the flow above the surface layer (i.e. in the stable boundary layer) is required.

In the stable boundary layer, buoyancy suppresses turbulent eddies, starting from the largest ones. Then, if in near-neutral conditions the size of eddies scales with the height above ground, in stable conditions, instead, they are much smaller and almost independent on the presence of the surface. This regime, in which z does not play anymore the role of scaling variable, is indeed termed *z-less stratification* (Nieuwstadt, 1984; Wyngaard and Coté, 1972). This means also that surface scales, which enter in MOST, are no longer appropriate for the description of the flow in the stable boundary layer.

Nieuwstadt (1984) proposed the adoption of *local* scaling in the stable boundary layer: from which the name of *local similarity theory*. The scales are the same of MOST but now are evaluated at the level of interest and depend on z:

- the height above ground z (which is retained despite the z-less behaviour);
- the local friction velocity: $u_*(z) = \tau^{1/2}(z)$ where $\tau = \sqrt{(\overline{u'w'})^2 + (\overline{v'w'})^2}$ is the magnitude of the kinematic vertical flux of horizontal momentum;

- the local temperature flux: $Q(z) = -\overline{w'\theta'_v}(z)$;
- the buoyancy parameter $\beta = g/\overline{\theta}_v(z) \approx g/\theta_{v00}$, for which does not matter if the local or a reference temperature is used.

Combining above scales a local Obukhov length can be defined:

$$\Lambda(z) \equiv \frac{\tau^{3/2}}{\kappa\beta Q} \tag{1.77}$$

where $\kappa = 0.4$ is, as usual, the von Kármán constant.

Local similarity theory (as MOST) predicts that, for the quasi-stationary and horizontally homogeneous stable boundary layer, properly adimensionalized mean gradients and turbulence statistics (i.e. variances and covariances) should be universal functions of the local stability parameter z/Λ. Local similarity theory comprises MOST as a special case for which fluxes do not vary significantly with height.

Surface-layer similarity functions, if correct, should be valid also above, in the stable boundary layer, when z/Λ is substituted to z/L. Indeed, local similarity predicts that these are universal functions of z/Λ only and should not depend on the height above ground alone. However, as we move far from the ground, other scales beside Λ, such as the boundary layer height, can play some role (Zilitinkevich and Esau, 2007). This can determine a dependence of similarity functions on the dimensional height above ground or on time (through the variation of the PBL height).

The argument used by Nieuwstadt (1984) to prove the validity of local scaling was the observation of the z-less behaviour in similarity functions for variances and covariances as $z/\Lambda \to \infty$. In the z-less regime, mean gradients should not depend on the height above ground (this not mean that they are constant but that z is not anymore an important scale). This mean that

$$\phi_a\left(\frac{z}{\Lambda}\right) = \frac{\kappa z}{a_*}\frac{d\overline{a}}{dz} \sim \frac{z}{\Lambda} \quad \text{as} \quad \frac{z}{\Lambda} \to \infty \tag{1.78}$$

and then

$$\frac{d\overline{a}}{dz} \sim \frac{a_*}{\kappa\Lambda}, \tag{1.79}$$

where a can be the wind speed, the temperature or a passive scalar and $a_*(z) = -\overline{a'w'}(z)/u_*(z)$ is its turbulent scale. The mixing length, which is related to the size of eddies becomes (see eq. (1.57))

$$l_a = \frac{\kappa z}{\phi_a} \sim \kappa\Lambda \quad \text{as} \quad \frac{z}{\Lambda} \to \infty,$$

confirming that, in the z-less regime (i.e. $\Lambda \ll z$), the size of eddies scales as Λ which is much smaller than z, the height above the surface.

For the wind speed gradient, the existence of the z-less behaviour has important implications. The dimensionless form of the TKE for stationarity and horizontal homogeneity and neglecting transport terms reads (see eq. (1.52)):

$$\phi_m(1 - \mathrm{R}_f) - \phi_\varepsilon = 0, \tag{1.80}$$

where we have introduced the flux Richardson number

$$\mathrm{R}_f \equiv \frac{\beta Q}{\tau d\overline{u}/dz} = \frac{z/\Lambda}{\phi_m(z/\Lambda)} \tag{1.81}$$

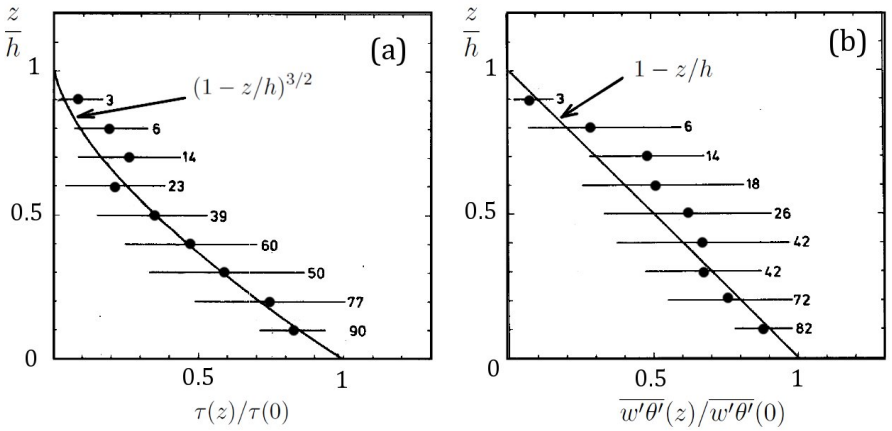

Figure 1.7: Vertical profiles for turbulent fluxes of momentum (a) and temperature (b), normalized by the surface value, for the stable boundary layer (adapted from Nieuwstadt, 1984).

which is an alternative local stability parameter.

R_f express the ratio between buoyancy destruction βQ and shear production $\tau d\overline{u}/dz$ of TKE. The flux Richardson number is positive for stable conditions with increasing stability corresponding to higher value of R_f. However, for the stationary and homogeneous turbulence no arbitrarily high value of R_f can be reached since for $R_f > 1$ destruction (both from buoyancy and viscous dissipation) overpass production in TKE budget (1.80) and conditions with decaying or intermittent turbulence occur.

From (1.81), the existence of a critical flux Richardson number, R_{fc}, requires that $\phi_m \sim z/\Lambda$ for $z/\Lambda \to \infty$, as z-less stratification predicts. Linear formulations of the type proposed by Högström (1996) and Businger et al. (1971) (i.e. $\phi_m = 1 + \beta_m(z/\Lambda)$, with $\beta_m \simeq 5$) predict the existence of a critical value $R_{fc} \simeq 0.2$, which is near to accepted limit for continuous turbulence (Grachev et al., 2013). The formulation adopted by Beljaars and Holtslag (1991) predicts $R_{fc} = 1$.

Similarity functions which levels-off or increase sub-linearly for $z/\Lambda \to \infty$ (as those proposed by Cheng and Brutsaert (2005a) and Grachev et al. (2007b)) does not predict the existence of any critical values for R_f. This level-off or sub-linear behaviour of ϕ_m for $z/\Lambda > 1$ is due to data points referring to the super-critical regime, i.e. characterized by $R_f > R_{fc} \simeq 0.2$-0.25 (Grachev et al., 2013), with turbulence which is not in equilibrium.

From a theoretical point of view, local similarity theory is satisfactory since it constitutes the framework in which turbulence in stable conditions can be studied independently on experimental circumstances. However, it is not well suited for practical applications since, for example, the vertical dependence of τ and Λ is necessary to derive the dimensional wind profile. Nieuwstadt (1984) derived vertical profiles of heat and momentum from a stable boundary layer model using as closure hypothesis a constant flux and gradient Richardson number, Ri$= (\phi_h/\phi_m^2)(z/\Lambda)$, equal to their critical values. In fig. 1.7, predictions from Nieuwstadt's model (curves) and observations (mean values and standard deviation in bin of z/h) at Cabauw mast, The Netherlands, are presented. The expected profiles for fluxes of momentum and heat in the stable boundary layer over flat terrain have the form (Sorbjan, 1986):

$$\tau(z) = u_*(1 - z/h)^{\alpha_1} \quad \text{and} \quad Q(z) = Q_0(1 - z/h)^{\alpha_2} \tag{1.82}$$

where h is the height of the boundary layer and α_1, α_2 are constants such that $\alpha_1 \geq \alpha_2$

that must be determined empirically. Nieuwstadt's model predict $\alpha_1 = 3/2$ and $\alpha_2 = 1$ (see fig. 1.7). From (1.82), (1.77)and (1.51) we have

$$\Lambda(z) = L(1 - z/h)^{3/2\alpha_1 - \alpha_2}. \tag{1.83}$$

However, further studies are required to establish the relation between local and global Obukhov length in the stable boundary layer.

Chapter 2

The experiment

An increasing concern arose about the effects of the changing climate on arctic regions. In the complex interactions occurring between land, sea, ice and atmosphere, the planetary boundary layer plays an essential role. For this reason, advance in the understanding of the arctic planetary boundary layer, which has, for most of the time the characteristics of a stable boundary layer (since long lived stable boundary layers onset from autumn to spring at high latitudes) is crucial.

This chapter give a description of the Climate Change Tower experiment (that is, indeed, an arctic experiment) from which the analyzed data comes. Firstly, a description of the experimental site, its morphology and climatology, is made. Then, a description of the instrumentation and data acquisition system is given.

2.1 The Climate Change Tower Integrated Project

The Italian National Research Council (CNR), since 1998, supported and coordinated research projects and scientific activities in the Arctic region, collaborating with the international community in Ny-Ålesund, a permanent settlements in the island of Spitzbergen, Svalbard archipelago.

The building and the implementation of the Amundsen-Nobile Climate Change Tower (CCT), in 2009, represented a major advance in the study of the arctic planetary boundary layer. Figure 2.3 refers to the earliest stages of the tower building. The name was chosen in honor of the Italian and the Norwegian explores Umberto Nobile and Roald Amundsen, who establish in Ny-Ålesund the starting point for their airship expeditions to the North Pole.

The CCT is located at Kolhaugen, just outside the Ny-Ålesund research village, at about 50 meters of altitude above seal level and it is 33 meters high. Instrumented with four level dedicated to the measurement of meteorological variables (wind speed, direction, temperature and relative humidity) and three dedicated to micrometeorological ones (by means of sonic anemometry), it permits the study of the lowest 30 m of the arctic planetary boundary layer. Data acquired on the CCT are transmitted in real-time to CNR, Institute of Atmospheric Science and Climate (ISAC) in Bologna, Italy. The work concentrated on observations taken from May 2012 to May 2014.

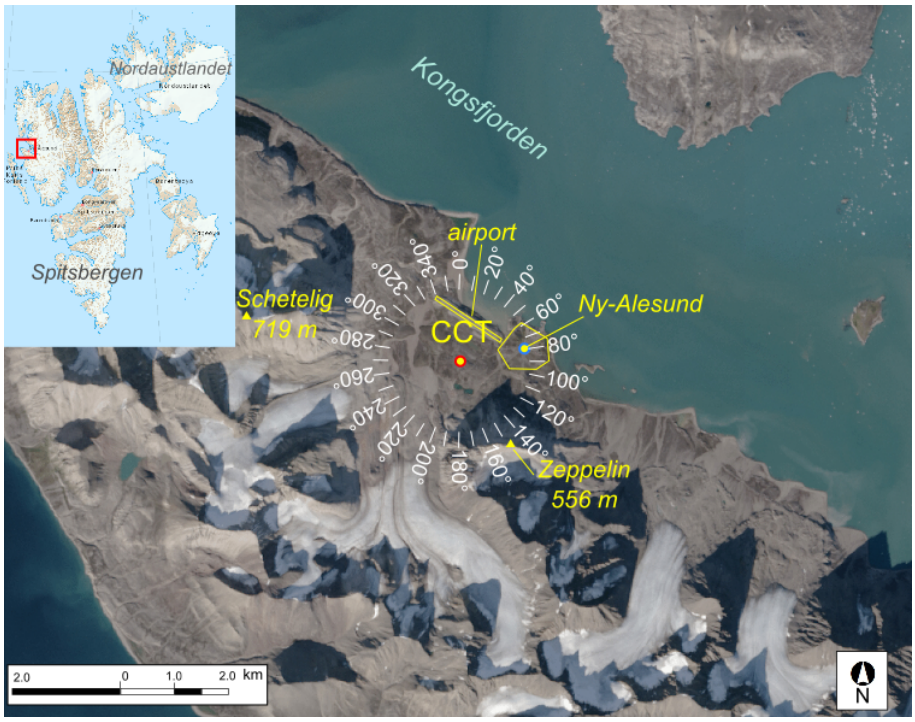

Figure 2.1: Left corner, small image: the Svalbard archipelago, the red square indicate Ny-Ålesund area. Big image: the experimental area and the main natural and artificial elements characterizing the site; the position of the CCT is indicated by the red dot (original maps from Norwegian Polar Institute (2015)).

2.2 The experimental site

The CCT is located in Ny-Ålesund (78°55.282′ N, 11°51.952′ E), a small village (originally devoted to mining) in the northwestern side of Spitzbergen, Savlbard, Norway (fig. 2.1). Ny-Ålesund is among the northernmost villages permanently inhabited, mostly for research activities. Indeed, because of its location on the western branch of the Spitzbergen current (the northernmost part of the gulf stream), Ny-Ålesund is characterized by a relatively mild climate, compared to other places at the same latitude.

2.2.1 Morphology

The topography of the area is quite complex (fig. 2.1). Ny-Ålesund is located in a peninsula facing Kongsfjorden. Both the fjord and the peninsula are oriented along the NW-SE direction and a mountain range, that do not overpass ∼700 m, runs through the peninsula in the same direction.

In particular, the CCT is located about 1.5 km west of the Ny-Ålesund village, in the coastal zone of Kongsfjorden (fig. 2.1). Mountains and glaciers surround the area from southeast to northwest. The nearest mountains are Schetelig (719 m, the highest), about 2 km northwest, and Zeppelin (556 m), about 1.5 km southeast. During the melting season, small lakes form in the area: one of them can be seen in fig. 2.1, about 500 m south of the tower.

The experimental site is not flat nor horizontally homogeneous (figs. 2.1 and 2.2). Furthermore, variations in terrain elevation are characterized by a wide range o spatial

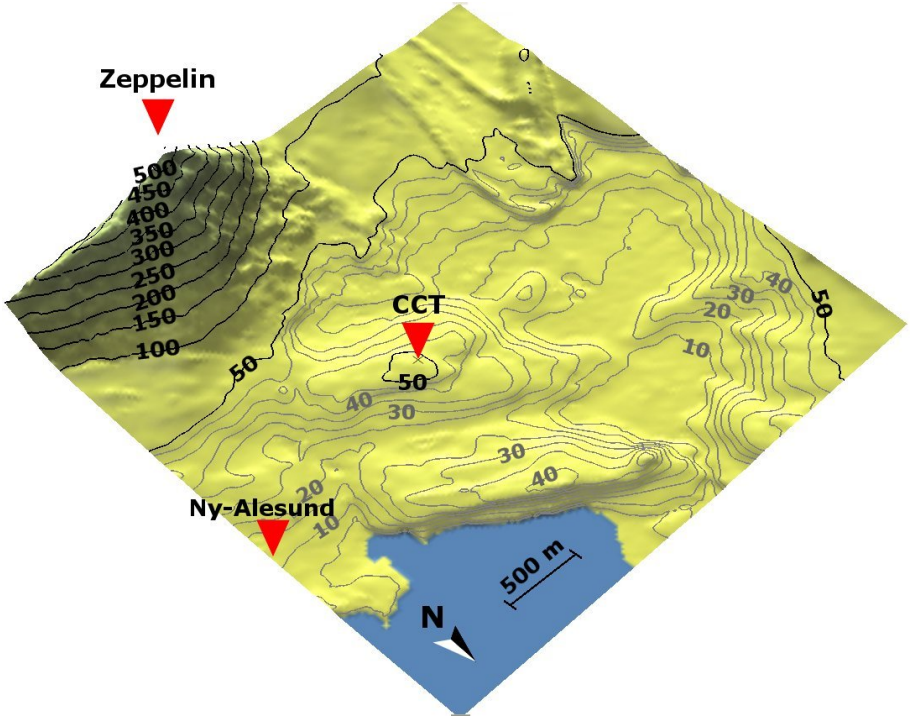

Figure 2.2: Elevations of the experimental site (in meters above m.s.l.): contour lines are drown, in gray, from 0 m to 50 m every 10 m and, above 50 m, in black, every 50 m (data from Norwegian Polar Institute (2014)).

scales and amplitudes. The most important are those associated with mountains, which occur on spatial scales of ∼1 km and have amplitude of ∼0.5 km, and those associated with terrain slopes near the coast, with spatial scales of ∼1 km and amplitude of ∼50 m (see fig. 2.2). Changes in surface characteristic also occur with land-sea, land-ice, land-urban transitions. Furthermore, seasonal variations of surface characteristics and morphology due to the snow-cover cycle are also present.

Surface morphology and characteristics show also a strong directional dependence with greater variations occurring in the cross-fjord direction (NE-SW) and lesser ones in the along-fjord direction (NW-SE), with respect to the position of the tower (figs. 2.1 and 2.2).

Also artificial structures are present in the area although their impact on the local environment should be much lesser than natural ones. About 1 km E-NE to the CCT there is the village of Ny-Ålesund, made of small buildings mostly devoted to research activities. At the same distance, the runway of Ny-Ålesund's airport, placed on a ridge along the coast, crosses the fetch in the sector 340–420°(60°) (figs. 2.1 and 2.2). Some elevated streets, which disappear in winter, connect Ny-Ålesund with other research stations in the area but their effect is fairly negligible compared with natural slopes.

Figure 2.3 shows the morphology of the area near the CCT in the snow-free period: the two photos were taken during the erection of the tower structure. On the left of fig. 2.3(a), taken looking toward northwest, is partially visible Schetelig mountain. From this point of view, the terrain appears quite flat with only gently slopes up to distances of 50–100 m from the tower. However, on the left of fig. 2.3(b), which was taken looking toward Kongsfjorden (north), are clearly visible slopes and depressions with melting snow or ice. On the right of fig. 2.3(b) is also visible the small house that host computers receiving data from the CCT instrumentation. During the snow-free season, the ground near the tower is covered

Figure 2.3: The CCT site as viewed from south-east (a) and from south (b) during the erection of the tower structure (ISAC–CNR, 2014).

by stones and short grass, typical of arctic tundra: no tall vegetation grows at these high latitudes.

Figure 2.5 refers to the permanent snow-cover period: May 2012, in that particular case. The snow cover smooths the irregularity of ground on small scales (e.g., stones) but slopes on larger scales still remain. Furthermore, during winter and spring the fjord can freeze, partially attenuating the effect of sea-land transitions.

2.2.2 Climatology

Being north of the Arctic Circle, Ny-Ålesund experiences polar night and polar day conditions: i.e., days with 24 hours of darkness and sunlight, respectively. Polar night starts on 24 October and ends on 18 February; polar day starts on 18 April and ends on 24 August (Maturilli et al., 2013).

The ground is covered by snow from October to May-June, when the melting season begins. However, summer snowfalls are also possible (Maturilli et al., 2013).

During polar night, a long lived stable boundary layer onsets. During polar day, when the sun is low above the horizon and snow covered ground is present (especially during spring), something like a “nocturnal” stable boundary layer can form. Transition months like September show conditions resembling that of a long lived SBL, probably because of the very low sun that cannot break-up the nocturnal layer during daytime.

Winds blow from three directions mainly (fig. 2.4): two along-fjord (noth-west and south-east) and one cross-fjord (south-west). Prevalently winds blow from south-east, in the sector 110°-130° although the strongest are from east/south-east, i.e. 90°-120° where we have unobstructed fetch for several kilometers (fig. 2.1). These winds, from inland of

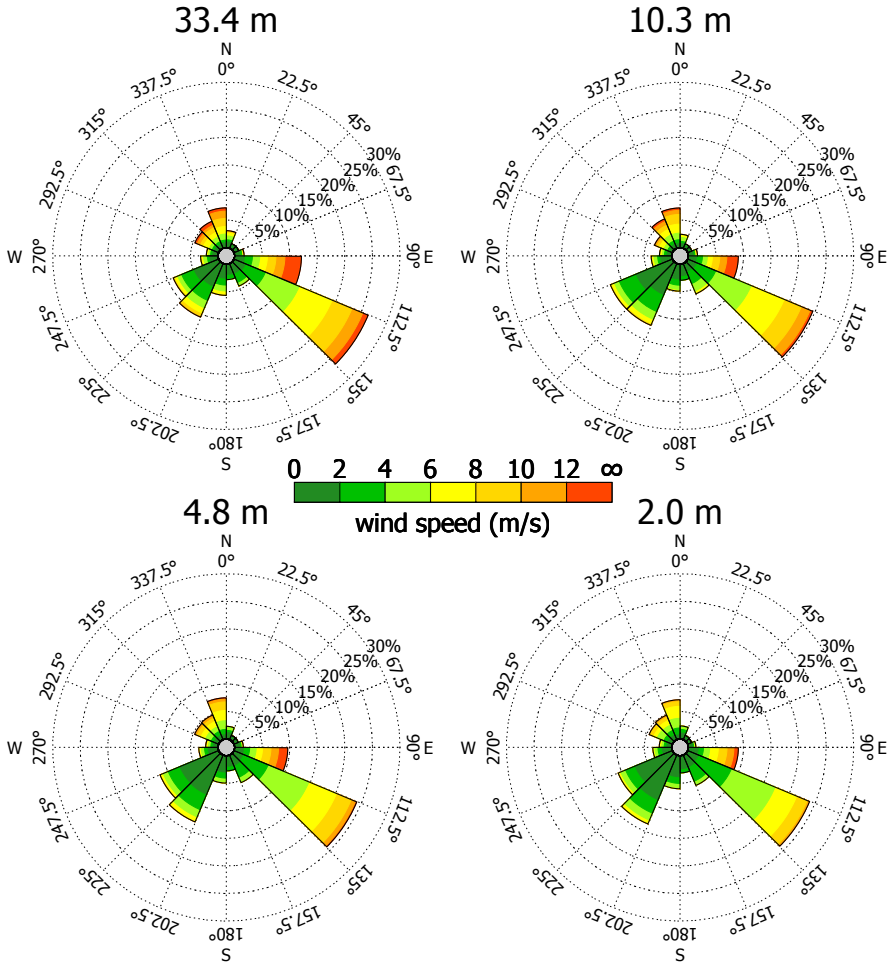

Figure 2.4: Wind roses at the four propeller anemometers levels of the CCT for the considered dataset.

Spitzbergen, are the result of the channeling of the flow by the fjord structure during most frequently synoptic conditions. The same mechanism is responsible also for north-westerly flows, less frequent than south-easterly ones. Anemometers should be optimally oriented for these two directions. Winds from south-west, i.e. 200°-240°, are related to katabatic flow from inland glaciers (fig. 2.1). However, for this sector, characterized mostly by weak winds, anemometers are downstream to the tower structure. Wind directions from this sector were then neglected in the present analysis.

2.3 Instrumentation and measurements

Meteorological and micrometeorological observations have been taken on CTT since the end of 2009. The data taken on the CTT are then transmitted in real-time to the Institute of Atmospheric Sciences and Climate (ISAC) of the National Research Council (CNR) in Bologna, Italy. From the end of May 2012 to the end of November 2012 and from June 2013 to April 2014 (excluding December 2013) nearly continuous boundary-layer measurements were taken on the CCT at Ny-Ålesund.

The CCT is a 33 m high rectangular tower, of the open lattice type, composed by 17 modules 1.4 m×1.8 m wide and 1.8 m high (Figs. 2.3 and 2.5). The main axis of the tower is oriented along the direction of prevailing winds (about 120° from north). Propeller-vane and sonic anemometers are mounted on booms oriented to north-est to minimize flow distortion by the tower structure for the prevailing wind direction. The booms were fixed along the south-eastern side of the tower, extending ∼2 m outside the tower. Thermo-hygrometers were placed on propeller booms (Fig. 2.5(b)) closer to the tower structure. Sonic anemometers are slightly more distant from the tower than propeller ones (Fig. 2.5(b)).

Observations of mean meteorological variables were carried out at four levels by propeller-vane anemometers and thermo-hygrometers at nominal heights (i.e. height above snow-free ground) of 2.0, 4.8, 10.3 and 33.4 m. Turbulence measurements were performed by sonic anemometers-thermometers at three levels, in the middle of low-response probes, at 3.7, 7.5 and 20.5 m. Other instruments were present on the CCT, including two radiometers and a sonic sensor for the retrieval of snow height. However, snow height measurements were seldom available during the considered period and, when available, some doubts were present about their reliability. Atmospheric pressure was also measured by a barometer at 5 m above ground. As a reference, snow height observations reported by the station of the Norwegian Meteorological Institute in Ny-Ålesund were considered[1]. The station is about 2 km east far from the tower. However, as long as possible, the study was limited to cases in the summer/early-autumn period, when snow-covered ground can be present but snow depth can be neglected in the estimation of the height above ground of observational levels.

Vane-propeller anemometers (Young) and slow-response thermo-hygrometers (Vaisala HMP45) provided measurements of horizontal wind speed ($S = \sqrt{u^2 + v^2}$), wind direction, temperature and relative humidity at four levels with a sampling rate of 1 sample per minute.

The sonic anemometers-thermometers (two Gill Solent instruments, R2 and R50, at 3.7 and 7.5 m and one Campbell CSAT3 instrument at 20.5 m) provided measurements of the three wind components in the meteorological system (u–westerly, v–southerly and w–vertical) and sonic temperature (T_s) at three levels. The sampling rates were 20 Hz for the two lowest levels an 10 Hz for the highest one.

[1] http://eklima.met.no/

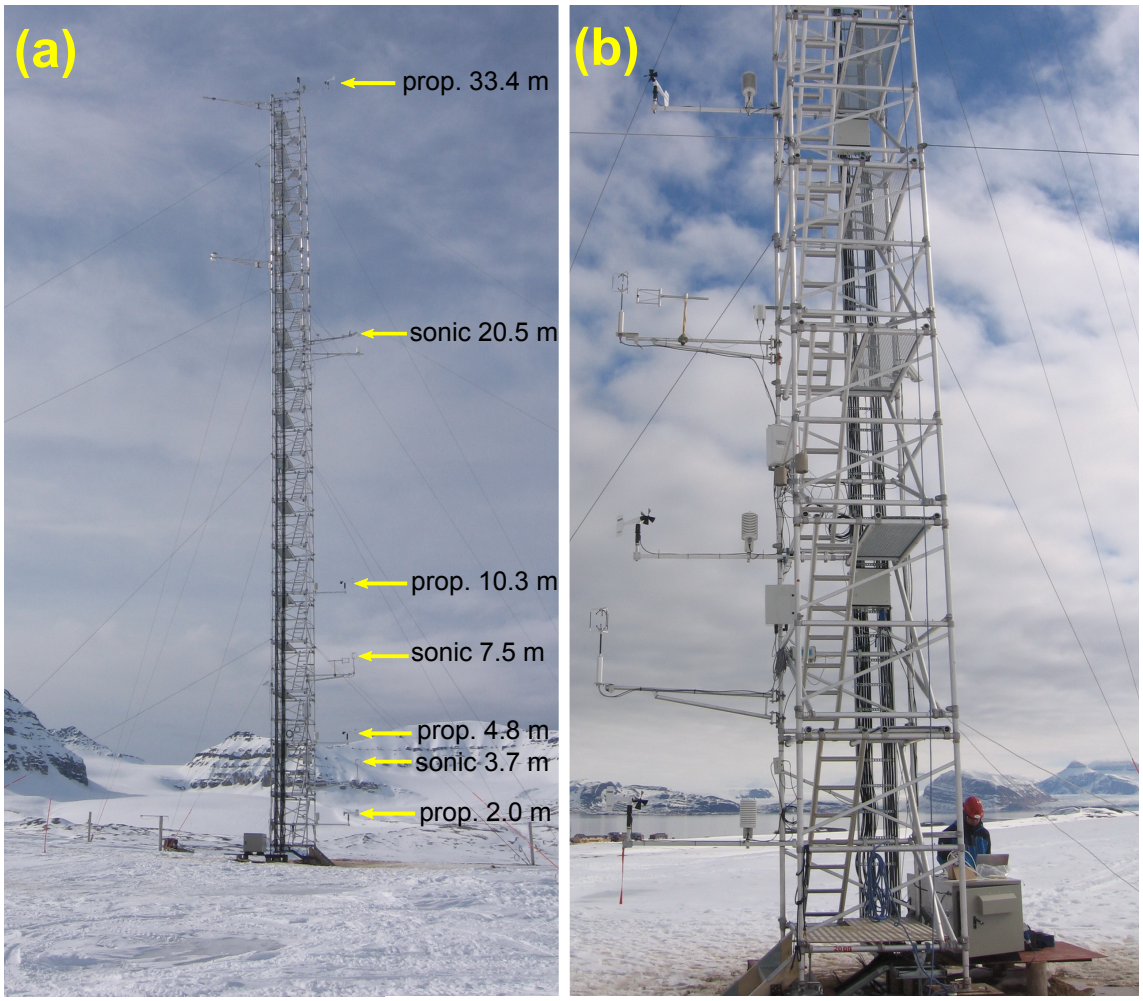

Figure 2.5: The CCT setup as viewed from the east side (a) and a close view of the lowest five measurement levels from the west side (b) (ISAC–CNR (2014)). The photos were taken in May 2012 but the setup remained unchanged during the whole considered period.

The considered dataset was composed by 10-min statistics computed from the row dataset. Mean variables were derived as simple averages between the samples (10 for slow-response probes, about 12000, for fast response ones) contained in each 10-min interval. Variances are also given for slow-response sensors. For fast-response ones, turbulent fluxes (i.e. covariances) were derived with the eddy correlation method. For example, for each 10-min interval, containing N samples, the averages

$$\overline{u} \equiv \frac{1}{N}\sum_{i=1}^{N} u_i \quad \text{and} \quad \overline{w} \equiv \frac{1}{N}\sum_{i=1}^{N} w_i$$

were computed and the covariance (the kinematic momentum flux) derived as

$$\overline{u'w'} \equiv \frac{1}{N}\sum_{i=1}^{N}(u_i - \overline{u})(w_i - \overline{w}).$$

No corrections for trends, spikes or other effects were applied.

Comparing time series of 10-min average wind speed, a time lag of 10 min was observed between the propeller data and the sonic ones: in particular, the sonic readings were in advance of 10 min with respect to the propeller ones. The same shift was observed in wind direction time series. Assuming that the same lag affected all the measured variables, a new dataset was obtained from the original one with a 10 min shift. A new synchronized dataset was obtained from the original with a shift of 10 min between the sonic and the propeller-thermo-hygrometer dataset.

Chapter 3

The wind shear sensitivity to the evaluation method

This chapter deals about observations reliability and methods. Observations regard mostly wind speed, measured by the seven anemometers on the CCT. Methods regard computation of wind speed gradients, which are the main focus of the whole work.

After a brief parenthesis about the difference between the scalar average (wind speed) and the vectorial average (wind velocity) of the horizontal wind vector (section 3.1), a calibration test is carried out between the wind speed measured by all propeller and sonic anemometers on the CCT (section 3.2). The calibration test was carried out comparing observations from different anemometers disposed in the operative CCT setup. The problem of the estimation of expected deviations between instruments because of their vertical separation was also addressed, although in a simplified manner. Finally, the behaviour of measured speed with respect to the wind direction was analyzed, comparing observations from different levels, and effects of the CCT structure on the probed flow were also discussed.

The next sections deal to the main topic of this chapter: i.e. gradients. Gradients are needed for the computation of the dimensionless wind shear, ϕ_m and then it is important to understand how much gradients are sensitive to the method of estimation. The sensitivity of gradients to the evaluation method receive usually little attention in boundary layer studies although some authors (Forrer and Rotach, 1997; Klipp and Mahrt, 2004) have made some investigations on this question.

The study dimensionless gradients, ϕ_m, instead of dimensionless wind speed, Ψ_m, avoid the determination of the roughness length, z_0, which is more complicated over complex terrain (variations with wind direction) and surface changing, for example between snow-covered and snow-free ground (variations with time). Furthermore, in the framework of local similarity theory where both friction velocity and Obukhov length can vary with height, the study of ϕ_m is easier than that of Ψ_m.

Gradients have the drawback of computational errors since they are not directly measured quantities. However, as will be shown, some doubts arose about the reliability of sonic speeds and turbulence measurements are available only at sonic levels. Then, to study wind speed, instead of gradients, an interpolation of wind speed at sonic levels or of turbulent fluxes at propeller ones would have been necessary anyway.

In section 3.3, the considered methods for the interpolation of the wind profile are presented and the other techniques employed for the calculations of gradients, for the CCT instrumental setup, are described in section 3.4. Using observations from the CCT dataset,

a comparison between results from different methods (i.e. log-linear and log-log[2] fits, Bessel and log-Bessel splines, finite and log-finite differences) is carried out in section 3.5.

In section 3.6 and section 3.7 the sensitivity of gradients and of dimensionless gradients to errors in the determination of the height above ground of observational level (i.e. to the presence of a displacement height), for example because of snow height, are estimated for the CCT setup.

3.1 Mean wind speed and mean wind velocity

Propeller-vane anemometers data are composed by 10-min averaged wind speed, direction and their variances. Sonic data contain also mean wind velocity. Boundary layer equations originally refer to mean wind velocity which differ, in general, from mean wind speed: although they do not differ very much for sufficiently strong winds driven by synoptic scale systems.

To use both propeller and sonic-data, we will derive an expression for obtaining mean wind velocity from mean wind speed and direction variance. The wind velocity is

$$\mathbf{U} = \mathbf{i}u + \mathbf{j}v \tag{3.1}$$

The wind speed is the modulus of the wind velocity:

$$S \equiv |\mathbf{U}| = [u^2 + v^2]^{1/2}. \tag{3.2}$$

The wind direction, γ, is the direction of the wind velocity measured clockwise from North. In the meteorological reference system (x-axis in E-W direction, positive westerly winds; y-axis in the N-S direction, positive southerly winds) the wind components are

$$u = -S\sin\gamma \quad \text{and} \quad v = -S\cos\gamma. \tag{3.3}$$

Splitting all the variables in eq.s (4.2) in a mean value and a fluctuation as

$$u = \overline{u} + u', \quad v = \overline{v} + v', \quad S = \overline{S} + S', \quad \gamma = \overline{\gamma} + \gamma', \tag{3.4}$$

and averaging we obtain

$$\overline{u} = -\overline{(\overline{S} + S')(\sin\overline{\gamma}\cos\gamma' + \cos\overline{\gamma}\sin\gamma')}, \tag{3.5a}$$

$$\overline{v} = -\overline{(\overline{S} + S')(\cos\overline{\gamma}\cos\gamma' - \sin\overline{\gamma}\sin\gamma')}. \tag{3.5b}$$

Then, supposing that $\gamma' \ll 1$, substituting the approximations $\cos\gamma' \approx 1 - \frac{\gamma'^2}{2}$ and $\sin\gamma' \approx \gamma'$ in (3.5), and retaining only perturbations products (neglecting higher order terms) we have

$$\overline{u} \approx -\overline{S}\sin\overline{\gamma}\left(1 - \frac{\overline{\gamma'^2}}{2}\right), \tag{3.6a}$$

$$\overline{v} \approx -\overline{S}\cos\overline{\gamma}\left(1 - \frac{\overline{\gamma'^2}}{2}\right), \tag{3.6b}$$

where we have assumed uncorrelated wind speed and direction fluctuations: i.e. $\overline{S'\gamma'} = 0$. From (3.6) we have an approximated relation between the modulus of the mean wind

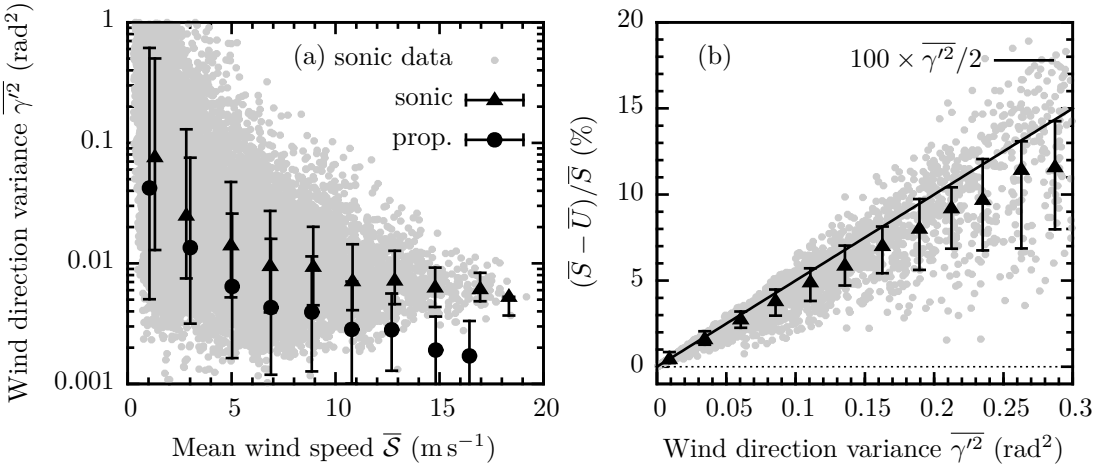

Figure 3.1: (a) Wind direction variance against wind speed for one sonic (level 4, 7.5 m) and one propeller (level 3, 4.8 m) anemometer on the CCT: bin medians and 15th-85th percentile ranges are shown for both, single data points for the sonic one only. (b) Wind speed-wind velocity deviations against wind direction variance for the sonic level 4: data points, bin medians and 15th-85th percentile ranges along with expected deviations from eq. (3.7) are shown.

velocity, $\overline{U} = [\overline{u}^2 + \overline{v}^2]^{1/2}$, the mean wind speed, $\overline{S} = \overline{[u^2 + v^2]^{1/2}}$, and the wind direction variance $\overline{\gamma'^2}$:

$$\overline{U} \approx \overline{S}\left|1 - \frac{\overline{\gamma'^2}}{2}\right| \tag{3.7}$$

that holds for $\overline{\gamma'^2} \ll 1$.

Relation (3.7) strictly resembles eq. (6) of Businger et al. (1971):

$$\overline{S} = \overline{U}\left(1 + \frac{\overline{v'^2}}{2\overline{U}^2}\right), \tag{3.8}$$

from which

$$\overline{U} \approx \overline{S}\left(1 - \frac{\overline{v'^2}}{2\overline{U}^2}\right), \tag{3.9}$$

for $\overline{v'^2} \ll \overline{U}^2$. In (3.8) and (3.9) $\overline{v'^2}$ is the variance of the lateral (transversal) horizontal wind speed in a reference frame aligned with the mean wind and not the variance of the northward component. In particular, taking $\gamma' \approx v'/\overline{U}$ we have $\overline{\gamma'^2} \approx \overline{v'^2}/\overline{U}^2$ that, substituted in (3.9), gives (3.7).

Figure 3.1(a) shows the wind direction variance against the mean wind speed (10-min averages) for one propeller and one sonic anemometer on the CCT. As we can see, $\overline{\gamma'^2} < 1$ for all data except in very light wind conditions ($\overline{S} < 1\,\mathrm{m\,s^{-1}}$). Note also that sonic direction variances tends to be greater than propeller-vane ones, particularly for light winds, when propeller-vane inertia is not negligible. Furthermore $\overline{\gamma'^2} < 0.1$ for almost all data with wind speeds greater than $5\,\mathrm{m\,s^{-1}}$. Thus, beyond this threshold, we will not expect appreciable differences between mean wind speed and mean wind velocity.

For wind direction variances $\overline{\gamma'^2} \leq 0.07$ rad^2 (which corresponds to a standard deviations of about 15°), the normalized differences between observed and computed velocity (using eq. (3.7)) are lesser than 1% for almost all data (figure 3.1(b)). About 80% of data in the dataset are below this threshold.

Table 3.1: Wind speed comparison tests. From left to right: below, central and above levels considered in the comparison; anemometer type of below, central and above levels: "p" stays for "propeller" and "s" for "sonic"; central level nominal height; above-below levels geometric mean height; logarithmic profile deviation term.

levels	anemometer type	z_ℓ (m)	$\sqrt{z_{\ell-1}z_{\ell+1}}$ (m)	$\kappa^{-1}\ln(z_\ell/\sqrt{z_{\ell-1}z_{\ell+1}})$
1–3–5	p–p–p	4.8	4.5	0.1
3–5–7	p–p–p	10.3	12.7	−0.5
2–4–6	s–s–s	7.5	8.7	−0.4
1–2–3	p–s–p	3.7	3.1	0.4
3–4–5	p–s–p	7.5	7.0	0.2
5–6–7	p–s–p	20.5	18.5	0.25

3.2 Comparison between wind speed observations

No calibration tests in controlled or environmental conditions were available for the seven anemometers installed on the CCT. Thus, a comparison between 10-min horizontal wind speeds measured by propeller-vane and sonic anemometers was carried out. Wind speed was chosen because is directly measured by both instrument types.

Calibration tests are usually made in controlled conditions (wind tunnel) or in environment, positioning the instruments as close as possible. Comparisons between vertically separated instruments, as in the CCT setup, are more complicated.

However, the wind speed from one anemometer was compared with the average between the speeds measured by the two neighbor anemometers: one located above and one below the considered level. This was done between propeller anemometers only, sonic anemometers only and between the two instrument types.

If the three anemometers, positioned at heights $z_{\ell-1}$, z_ℓ and $z_{\ell+1}$, with $z_{\ell-1} < z_\ell < z_{\ell+1}$, are perfectly calibrated and are probing a logarithmic wind profile,

$$\overline{S}_\ell = \frac{\overline{S}_{\ell-1} + \overline{S}_{\ell+1}}{2} + \frac{u_*}{\kappa}\ln\left(\frac{z_\ell}{\sqrt{z_{\ell-1}z_{\ell+1}}}\right), \tag{3.10}$$

where $\overline{S}_\ell$ is the mean wind speed at height z_ℓ. Hence, if the central anemometer height equals the geometric mean height of the others two anemometers, $z_\ell = \sqrt{z_{\ell-1}z_{\ell+1}}$, the logarithm in (3.10) vanishes and the central anemometer speed equals the above-below average.

On the CCT, anemometers were not located exactly at the geometric mean of the above and below anemometers heights, as table 3.1 shows. This could produce bias also between perfectly calibrated instruments when above-below average and local speed are compared. However, the modeling of this effect require the knowledge of the wind profile, which is what we searching for. Anyway, an attempt was made to estimate its contribution at least for a logarithmic profile: i.e. the last term of the right side of eq. 3.10. An expression between u_* and the wind speed was obtained fitting the *local* friction velocity, $\tau^{1/2}$, with a linear relation for the three sonic levels. As an intermediate expression between the three levels was chosen $u_* = 0.05\overline{S}$: this should be viewed only as an "order of magnitude" estimate.

Figure 3.2 shows the results of the comparison between instruments of the same type: (a)-(f) for propeller anemometers, (g)-(i) for sonic ones. Data are classified by the stability

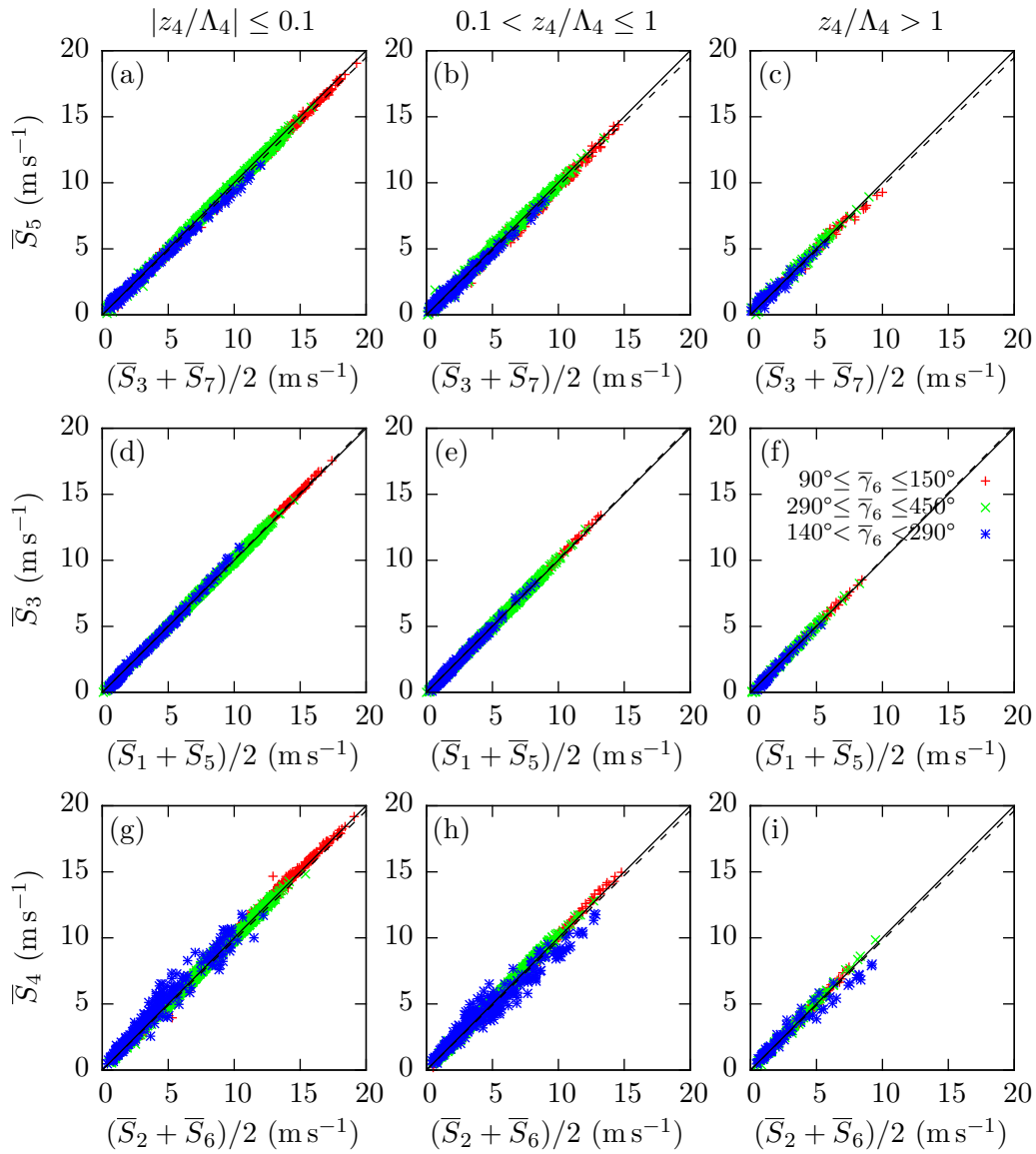

Figure 3.2: Same type anemometers comparison tests: first and second rows, propeller anemometers, third row, sonic anemometers. Wind speed from one anemometer (10-min average) is plotted against above-below same type anemometers average. Data are subdivided by z/Λ observed at level 4, $z = 7.5\,m$, (columns) and wind direction at the central level. Indexes indicate anemometer level.

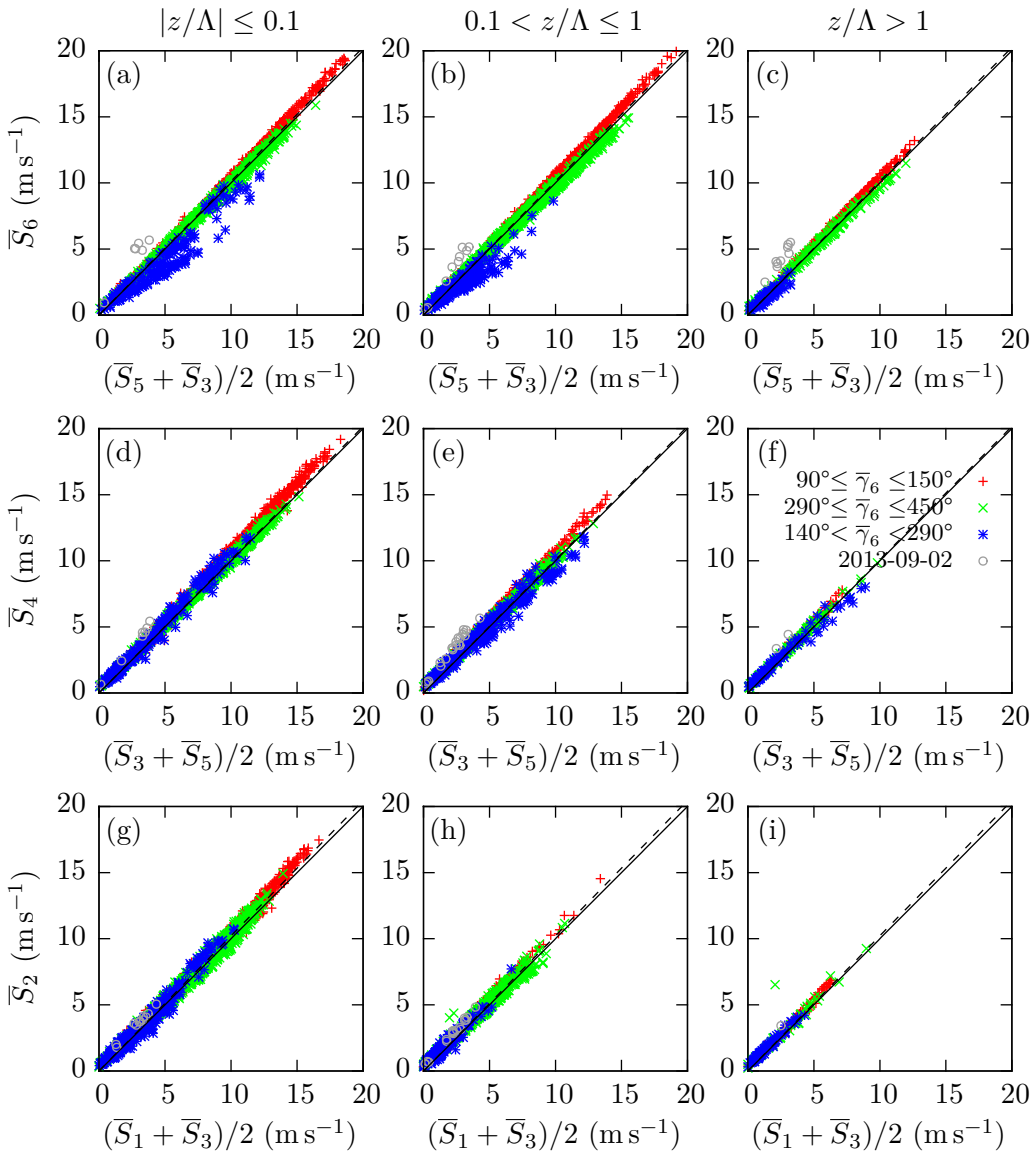

Figure 3.3: Sonic-propeller anemometer comparison tests: 10-min mean horizontal wind speed measured by sonic anemometers are plotted against averages between the above and below propeller anemometers. Data are subdivided by stability (columns) and sonic wind direction at the considered level.

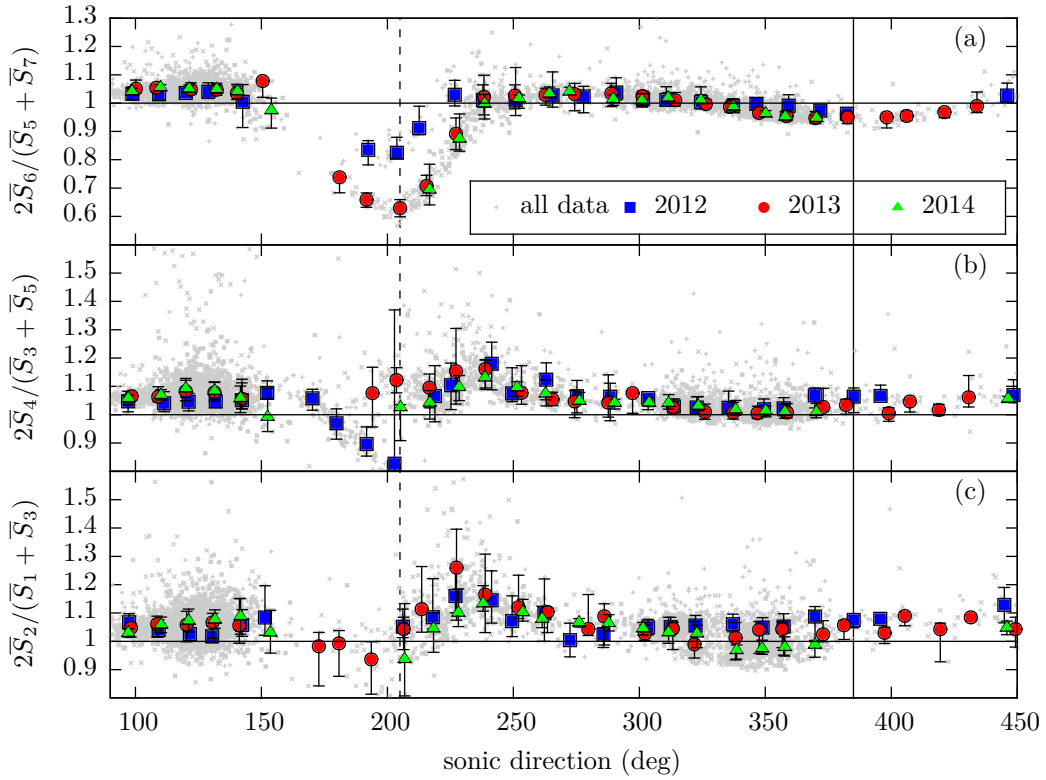

Figure 3.4: Ratios between sonic and below-above propeller average wind speeds against sonic wind direction (degrees from north) for the three sonic levels. Points are 10-min data, open symbols are bin medians. Data are classified by year. Vertical lines indicate the two wind directions for which anemometers are upwind (solid) and downwind (dashed) to the tower.

parameter z/Λ and wind direction at the central level. Propeller levels are 1 (2.0 m), 3 (4.8 m), 5 (10.3 m) and 7 (33.4 m). Sonic ones are 2 (3.7 m), 4 (7.5 m) and 6 (20.5 m). The dashed lines represent eq. (3.10), in which was substituted the above expression for u_* with $\overline{S} = (\overline{S}_{\ell-1} + \overline{S}_{\ell+1})/2$. The deviation from the 1:1 relation is negligible in all cases.

For the wind directions lesser influenced by the tower structure, $90° \leq \overline{\gamma} \leq 150°$ and $290° \leq \overline{\gamma} \leq 450°$, the agreement between same type anemometers is good, for all stabilities, even if sonic data are slightly more scattered than propeller ones. For wind directions more influenced by the tower structure, $150° < \overline{\gamma} < 290°$, propeller data show a small bias [figure 3.2(a)-(b)] and sonic data are very scattered [figure 3.2(g)-(i)]. The small bias between level 5 and levels 7 and 3 average could be do to a lesser influence of the tower structure on level 7 anemometer which is positioned on tower top.

The comparison between sonic speed and propeller speed is shown in figure 3.3. The scatter is greater with respect to figure 3.2, especially for level 2 and 4 [figure 3.3(d)-(e) and (g)-(h)]. Some outliers are present for wind speeds lesser than $\sim$5 m s^{-1}: those of figure 3.3(a)-(c) all refer to 2 September 2013. A positive bias between sonic and propeller speeds is present for E-SE winds for all the three sonic levels. A variable negative bias between level 6 sonic speed and levels 5-7 average for tower influenced flows ($150< \overline{\gamma} <290$) was also observed [figure 3.3(a)-(b)].

To further investigate the bias dependence on wind direction observed in the sonic-propeller comparison, sonic-propeller speeds ratios were plotted against sonic direction (figure 3.4). All 10-min runs with sonic wind speeds greater than 2 ms^{-1} are considered.

This threshold was adopted in order to reduce scattered points. This time, runs are subdivided by year: 2012 runs were acquired from May to November, 2013 runs from June to November and 2014 runs from January to April.

Level 6 ratios show a well defined wind direction dependence with two distinct minima [figure 3.4(a)]: one, more pronounced, around 200°, and another, less pronounced, around 385°. The two directions are, respectively, the opposite and the pointing direction (25°) of the anemometers booms and correspond to anemometers downwind and upwind with respect to the tower. The magnitude of the absolute minimum is greater for 2013-2014 than for 2012 runs, with speed differences increasing (in absolute value) from $\sim -20\%$ to $\sim -40\%$. Two nearly flat regions with small biases extend from 90° to 140° and from about 240° to 320°, corresponding to S-SE and W-NW flows for which the anemometers exposition should be optimal. Median speed differences in these two region are around 5% or lesser, but deviations greater than 10% are observed.

The behavior of levels 4 and 2 ratios [figure 3.4(b)-(c)] is less clear and an increased scatter is present, with a predominance of positive biases. No absolute minima are still easy recognizable around 200°, but large negative differences, $\sim -20\%$, were observed for level 4 2012 runs [figure 3.4(b)]. Instead, a maximum was observed for westerly flows, around 220°-230°, with median speed differences greater than 10%.

Concluding we can say that:

- Good agreement was observed between anemometers of the same type, at least for wind directions no strongly influenced by the tower structure; however, propeller readings appeared more coherent than sonic ones.
- Wind direction dependent biases and poorer correlation are present between sonic and propeller data. In particular, level 6 sonic anemometer readings showed more correlation with propeller speed and a clearer directional dependence with respect to the others two sonic anemometers.
- The dependence of sonic-propeller bias on wind direction and the coherence between readings from instruments of the same type suggest that the observed systematic deviations are due to anemometers arrangement (sonic booms are longer than propeller ones) rather than calibration errors.
- Wind directions between 150° and 250° are the more influenced by the tower structure but also for E-SE winds, for which the anemometers arrangement should be optimal, on average, sonic-propeller speed differences of about, or more, than 5% were observed.

3.3 Interpolation of wind speed observations

Usually, in atmospheric boundary layer studies, vertical gradients of mean variables are calculated fitting observations with a chosen profile (e.g., Businger et al., 1971; Nieuwstadt, 1984; Högström, 1988; Grachev et al., 2007b) and then computing derivatives. The most popular fitting profile is a second order polynomial in $\ln z$ (Businger et al., 1971; Högström, 1988; Grachev et al., 2007b) but also a log-linear profile is used (Howell and Sun, 1999; Yagüe et al., 2006). Forrer and Rotach (1997) and Nieuwstadt (1984) fitted wind speed and temperature observations with a log-quadratic profile. Businger et al. (1971) and Klipp and Mahrt (2004) derive gradients from a local fit: i.e. fitting only observations near to the level of interest. Finite differences are also sometimes used (Cheng and Brutsaert, 2005a; Ha et al., 2007) both in their linear or logarithmic form.

3.3.1 Fits

All the most used fitting profiles can be obtained, with particular choices of the coefficients, from the general one:

$$y(z) = a_0 + a_1 z + a_2 z^2 + a_3 \ln z + a_4 \ln^2 z, \tag{3.11}$$

z is the height above ground and y can be any atmospheric variable (typically wind speed and temperature). Deriving (3.11) with respect to z we obtain the general vertical gradient

$$\frac{dy}{dz} = a_1 + 2a_2 z + \frac{a_3}{z} + 2a_4 \frac{\ln z}{z}. \tag{3.12}$$

For the log-linear profile $a_2 = a_4 = 0$; for the log-log[2] profile $a_1 = a_2 = 0$; for the Nieuwstadt wind speed and temperature profiles $a_4 = 0$. All these profiles are generalizations of the logarithmic one, which is the accepted surface layer profile for almost neutral conditions.

Fits can be *local* (Businger et al., 1971; Klipp and Mahrt, 2004) or *global* (Nieuwstadt, 1984; Högström, 1988; Yagüe et al., 2006; Grachev et al., 2007b). In the first case many fits for many levels are made considering only the nearest observations. In the second , one fit is made with observations from all levels. Local fits require many measurement levels.

Fits lead to smooth profiles and then less erratic gradients. However, especially with global fits and goodness of fit selections, results could be biased toward the chosen fitting profile. Some authors have investigated on the sensitivity of their results to the chosen fitting-profile founding that it is generally negligible (Businger et al., 1971; Grachev et al., 2007a). However, the question "How much are (non-dimensional) gradients sensitive to the evaluation method?" receive usually little attention.

3.3.2 Bessel splines

Splines are more robust than fits: no *a priori* assumption on the expected profile is necessary. They are also a local method. On the other hand, interpolation could lead to less smother profiles. Bessel cubic splines are among interpolation methods that give smoother profiles. Furthermore, the interpolated profile has continuous first derivatives (gradients).

Given N x-ordered interpolation points, $(x_1, y_1), \ldots, (x_N, y_N)$, where x and y are the independent and dependent variables, respectively, the Bessel cubic spline for the n-th interval $x_n \leq x \leq x_{n+1}$, with $2 \leq n \leq N-2$, is (de Boor, 2001)

$$y_n(x) = c_{0,n} + c_{1,n}(x - x_n) + c_{2,n}(x - x_n)^2 + c_{3,n}(x - x_n)^3 \tag{3.13}$$

with

$$\begin{aligned} c_{0,n} &= y_n, \\ c_{1,n} &= s_n, \\ c_{2,n} &= ([x_n, x_{n+1}]y - s_n)/\Delta x_n - c_{3,n}\Delta x_n, \\ c_{3,n} &= (s_n + s_{n+1} - 2[x_n, x_{n+1}]y)/(\Delta x_n)^2, \end{aligned}$$

where

$$[x_n, x_{n+1}]y = \frac{y_{n+1} - y_n}{x_{n+1} - x_n},$$

for $1 \leq n \leq N-1$, is the first divided difference for the n-th interval, $\Delta x_n = x_{n+1} - x_n$ and

$$s_n = \frac{\Delta x_n [x_{n-1}, x_n] y + \Delta x_{n-1} [x_n, x_{n+1}] y}{\Delta x_n + \Delta x_{n-1}}, \tag{3.14}$$

for $2 \leq n \leq N-1$, is the spline slope at the n-th interpolation point. Eq. (3.14) is the slope of the parabola interpolating the point and its two neighbors and can be viewed also as a generalization of the centered differences formula for unevenly spaced points. Bessel splines were chosen because of their easy implementation and since only three points are required for computing one slope (e.g., Akima splines require five points).

No cubic Bessel splines can be computed at the two end-intervals, $x_1 \leq x \leq x_2$ and $x_{N-1} \leq x \leq x_N$, because Bessel slopes at the end-points, s_1 and s_N, are not defined [eq. (3.14)]. However, the first and the last intervals are interpolated with parabolic splines matching Bessel slopes at the second and the last but one points, respectively. The splines for the first and the last intervals are

$$y_1(x) = c_{0,1} + c_{1,1}(x - x_2) + c_{2,1}(x - x_2)^2 \quad \text{for} \quad x_1 \leq x \leq x_2 \tag{3.15}$$

and

$$y_{N-1}(x) = c_{0,N-1} + c_{1,N-1}(x - x_{N-1}) + c_{2,N-1}(x - x_{N-1})^2 \quad \text{for} \quad x_{N-1} \leq x \leq x_N, \tag{3.16}$$

where

$$\begin{aligned} c_{0,1} &= c_{0,2} = y_2, & c_{0,N-1} &= y_{N-1}, \\ c_{1,1} &= c_{1,2} = s_2, & c_{1,N-1} &= s_{N-1}, \\ c_{2,1} &= (s_2 - [x_1, x_2] y)/\Delta z_1, & c_{2,N-1} &= ([x_{N-1}, x_N] y - s_{N-1})/\Delta x_{N-1}. \end{aligned}$$

Eq. (3.15) and (3.16) are also the expressions for the arc of parabolas interpolating the first three and the last three points.

Taking as independent variable $\ln x$ instead of x, logarithmic profiles are perfectly interpolated. Bessel-log splines are obtained from Bessel splines expressions substituting $\ln x$ to and $\ln x_n$ to z_n. Whit this choice, interpolation points are approximately evenly spaced.

3.4 Gradients computation

Wind speed gradients were computed at the three sonic levels (3.7, 7.5 and 20.5 m) from propeller observations only (2.0, 4.8, 10.3 and 33.4 m). Indeed, the observed deviations between propeller and sonic wind speed can produce wildly oscillations in the interpolated profile when local methods, such as splines, are employed.

As a sensitivity test, vertical gradients of mean wind speed computed with different methods were compared. The considered methods were log-linear and log-log^2 fits, Bessel and log-Bessel splines, finite and log-finite differences. Wind profiles were obtained from propellers data only. Derivatives were then computed at the sonic levels. All the stable dataset were considered, without any selection. Thus, cases with light winds or strongly perturbed flows (by the tower structure) were also present. With this choice, the behavior of each method was studied on a wide range of wind profiles.

Firstly, 10-min average wind speeds from the four propeller anemometers were fitted with the log-linear profile [eq. (3.11) with $a_2 = a_4 = 0$] and with the log-log^2 [eq. (3.11) with

$a_1 = a_2 = 0$] using a linear unweighted least squares method (Press et al., 1997, p. 665): linear, because the problem is linear in the unknown coefficients a_i; unweighted, because χ^2 was computed simply as the sum of the squares of the residuals between expected and observed values. Then, having the coefficients of the fitting profiles, slopes at the three sonic levels were obtained from (3.12). Nieuwstadt profile was not tested because it needs the determination of four coefficients but only four observational levels were considered.

Observations from the four propeller anemometers are then interpolated with cubic Bessel splines [eq. (3.13)] in the central interval (between the second and the third propeller levels) and with quadratic splines matching Bessel slopes [eq.s (3.15) and (3.16)] in the the two end intervals (between the first and the second, and between the third and the fourth propeller levels). Interpolation was carried out in two ways. The first taking as independent variable the height above ground and, the second, taking its logarithm. Hereafter the two interpolation methods will be called Bessel and log-Bessel splines, respectively.

Bessel splines are obtained from (3.13), (3.15) and (3.16) (and from the relative coefficients expressions) taking $x = z$, $x_n = z_n$ and $y_n = \overline{S_n}$, where z is the height above ground and $\overline{S_n}$ is the wind speed measured by the propeller anemometer at height z_n. Gradients are then computed from the obtained splines coefficients, evaluating the derivatives of (3.13), (3.15) and (3.16) at the sonic anemometer heights.

Analogously, the expressions for log-Bessel splines are obtained taking $x = \ln z$ and $x_n = \ln z_n$ in (3.13), (3.15) and (3.16). For example, for the central interval (between the second and the third propeller anemometers) we have

$$y_2(z) = c'_{0,2} + c'_{1,2} L_2(z) + c'_{2,2} L_2^2(z) + c'_{3,2} L_2^3(z), \tag{3.17}$$

where the coefficients $c'_{i,j}$ are computed as for Bessel splines but taking $x_n = \ln z_n$ and $L_n(z) \equiv \ln(z) - \ln(z_n)$ was introduced for sake of brevity. Deriving (3.17) by z and considering that $dL_n/dz = 1/z$ we have the vertical gradient for the central interval:

$$\frac{dy_2}{dz} = \frac{c'_{1,2} + 2c'_{2,2} L_2(z) + 3c'_{3,2} L_2^2(z)}{z}. \tag{3.18}$$

It is interesting to note that log-Bessel slopes at the n-th interpolation point [eq. (3.14) for $x_n = \ln z_n$], with $2 \le n \le N$, is the slope of the parabola

$$p_n(z) = A_n + B_n \ln z + C_n \ln^2 z \tag{3.19}$$

that interpolate the point itself and its two neighbors. Looking at (3.19), one can think that some analogies exist between log-Bessel splines and log-log^2 fit even if the first is a *local* interpolation method and the second is a *global* fit. The advantages of log-Bessel against Bessel splines are that interpolation points are approximately equally spaced in $\ln z$ and logarithmic profiles are exactly interpolated.

Finally, vertical gradients are computed with finite differences taking both z and $\ln(z - d)$ as independent variables. This is the same as an interpolation with a piecewise linear and a piecewise logarithmic profile, respectively. The slope is continuous (constant for linear splines) in each layer delimited by two near propeller levels but it is generally discontinuous at the propellers heights.

In the linear case, the speed gradient in each layer is constant:

$$\frac{d\overline{S}}{dz} = \frac{\overline{S}_{n+1} - \overline{S}_n}{z_{n+1} - z_n} \quad \text{for} \quad z_n < z < z_{n+1}, \tag{3.20}$$

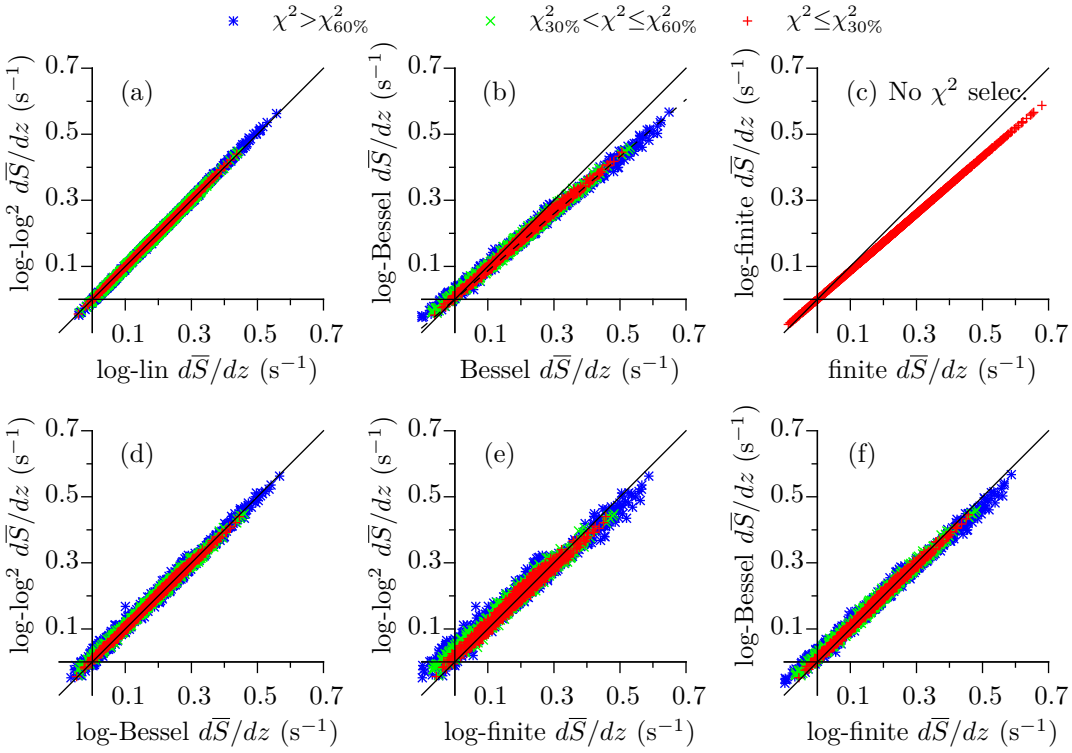

Figure 3.5: Level 2 (3.7 m) wind speed vertical gradients intercomparison: (a) log-log^2 fit vs. log-linear fit; (b) log-Bessel vs. Bessel splines; (c) log-finite differences vs. linear-finite differences; (d) log-Bessel splines vs. log-log^2 fit; (e) log-log^2 fit vs. log-finite differences; (f) log-Bessel splines vs. log-finite differences. Dots are 10-min data, solid lines are 1 : 1 relation, dashed lines in (b) is eq. (3.22). Profiles classification: most logarithmic, red points; intermediate, green points; least logarithmic, blue points. No profile classification is made in (c).

where $\overline{S}_n$ and $\overline{S}_{n+1}$ are the two propeller speeds and z_n, z_{n+1}, the two propeller heights. The gradient at the sonic level is that of the layer.

For the logarithmic case, the gradient in each layer is

$$\frac{d\overline{S}}{dz} = \frac{\overline{S}_{n+1} - \overline{S}_n}{\ln z_{n+1} - \ln z_n} \frac{1}{z} \quad \text{for} \quad z_n < z < z_{n+1}. \tag{3.21}$$

where symbols are as in (3.20). The slope at the sonic levels can be obtained from (3.21) substituting in z the sonic anemometers heights.

As for log-Bessel splines, log-finite differences gives exact slopes for logarithmic profiles. Although finite differences are a quit rough method for gradients evaluation, easy implementation and robustness make it a useful in intercomparison tests.

3.5 Gradients intercomparison

Vertical gradients of 10-min average horizontal wind speed were calculated at the three sonic levels heights (level 2 at 3.7 m, level 4 at 7.5 m and level 6 at 20.5 m) for all the stable dataset. Runs acquired on 2 September 2013 were discarded since considered not reliable.

Log-linear and log-log^2 fits, Bessel and log-Bessel splines, linear and log-finite differences were used for the computation. No snow depth corrections were adopted for anemometers

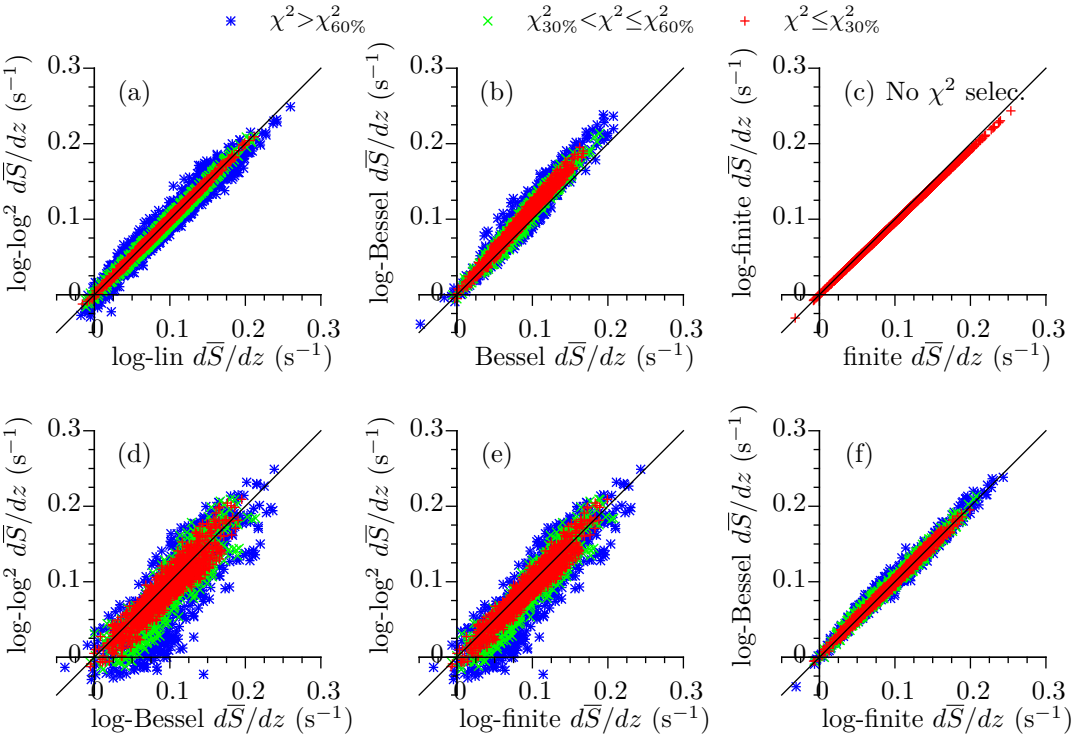

Figure 3.6: Level 4 (7.5 m) wind speed vertical gradients intercomparison (see figure 3.5).

heights taken equal to their nominal values. Vertical gradients of 10-min mean wind from the different methods are shown in figure 3.5, 3.6 and 3.7 for level 2, 4 and 6, respectively. Results are presented plotting slopes from one method against those from one other.

Furthermore, a profile classification of gradients was made. For each run, propeller observations were fitted with a logarithmic profile $y(z) = A + B\ln(z - d)$ and $\chi^2 = \sum_{i=1}^{4}(y(z_i) - \overline{S}_i)^2$ computed (the sum in over propeller levels). Two values of χ^2, $\chi^2_{30\%} = 0.015\,\mathrm{m^2 s^{-2}}$ and $\chi^2_{60\%} = 0.04\,\mathrm{m^2 s^{-2}}$, were then chosen such that about 30% and 60% of the observed profiles showed a χ^2 lower than the first and the second value, respectively. Runs, and hence gradients, are then subdivided in three classes: $\chi^2 \leq \chi^2_{30\%}$, $\chi^2_{30\%} < \chi^2 \leq \chi^2_{60\%}$ and $\chi^2 > \chi^2_{60\%}$ (red, green and blue points, respectively, in figures 3.5, 3.6 and 3.7). The first and the third classes contain, in order, the most and the least logarithmic profiles.

Several conclusions can be drawn from the intercomparison. All methods showed a decrease in gradients magnitude with increasing height (from fig. 3.5 to fig. 3.7), as expected. Negative gradients were observed both from fit and interpolation methods at all levels. They are associated mostly with weak winds ($\overline{S} \lesssim 3\,\mathrm{m\ s^{-1}}$) and flows strongly perturbed by the tower structure ($150° \lesssim \overline{\gamma} \lesssim 300°$) [figure 3.8(c)]. However these two conditions are related because lighter winds blew mostly from this sector (see figure 2.4).

The agreement between log-linear and log-log^2 gradients was generally high [figures 3.5-3.7, plot (a)] except at level 4 [figure 3.6(a)] where an increased scatter was observed for least logarithmic profiles.

Instead, biases and more scatter were observed between log-Bessel and Bessel splines slopes [figures 3.5-3.7, plot (b)]. Biases are greater for the most logarithmic profiles: this is particularly evident in figures 3.6(b) and 3.7(b) where red points show greater systematic

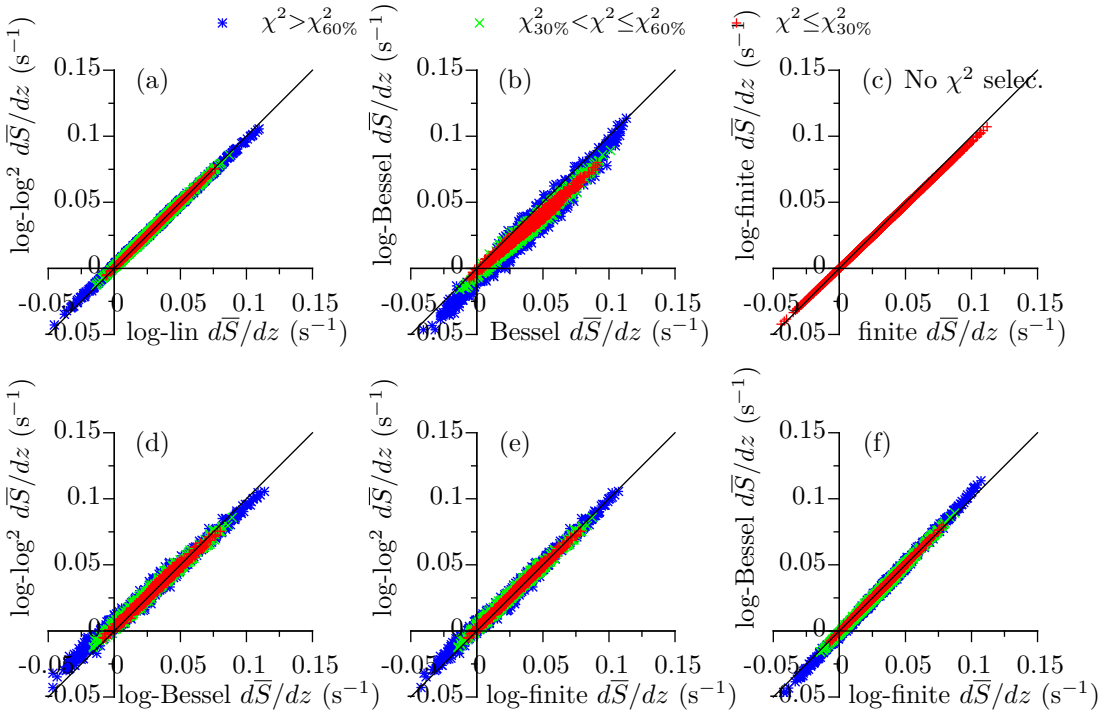

Figure 3.7: Level 6 (20.5 m) wind speed vertical gradients intercomparison (see figure 3.5).

deviations from the 1 : 1 relation line. Biases between log-Bessel and Bessel splines were obtained fitting (red) points belonging to most logarithmic profiles ($\chi^2 \leq \chi^2_{30\%}$) with the linear relation $y = ax$. Levels 2 and 6 log-Bessel slopes were, on average, 13% and 20% lower, respectively, than Bessel ones. Instead, level 4 log-Bessel slopes were, on average, 17% greater than Bessel ones. Large Bessel slopes at the higher sonic level (20.5 m) are due to the Bessel splines bump between the two higher propeller levels visible in all the three profiles of figure 3.8 and in about 100 randomly chosen profiles too.

The relation between log-finite and (linear) finite differences slopes depends only on anemometers heights. For this reason, no profile classification was adopted in plot (c) of figures 3.5, 3.6 and 3.7. Indeed, from (3.21) , log-finite slope at sonic height z, located between two observational levels n and $n+1$, can be expressed as

$$\frac{dS}{dz} = \frac{z_{n+1} - z_n}{z \ln(z_{n+1}/z_n)} \frac{S_{n+1} - S_n}{z_{n+1} - z_n}, \tag{3.22}$$

where the last factor in the right hand side of (3.22) is just the finite differences slope for the layer.

In plot (c) of fig. 3.5-fig. 3.7, points follow eq. (3.22). Deviations between log-finite and finite differences, which are 14% for level 2, become 4% for level 4 [figure fig. 3.6(c)] and level-6 [figure fig. 3.7(c)].

Eq. 3.22 is also plotted in figure fig. 3.7(b) because points that refer to most logarithmic profiles seem to follow it, suggesting a common behavior between log-Bessel splines and log-finite differences, and between (linear) Bessel splines and (linear) finite differences at least at this height.

In plots (d), (e) and (f) of fig. 3.5, fig. 3.6 and fig. 3.7 a comparison is made between gradients from methods that share a logarithmic behavior. Due to the very similar behavior

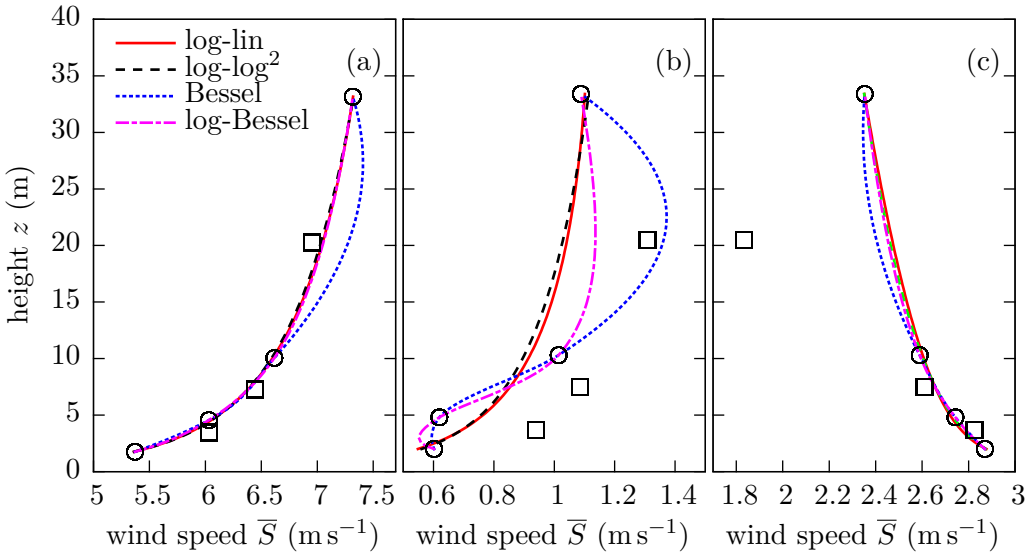

Figure 3.8: Three wind speed profiles for: (a) moderate NW winds (31 May 2012, 05.00, local time); (b) light SW winds strongly perturbed by the tower structure (8 June 2012, 6.20); (c) weak SW perturbed winds with a snow height of ∼1 m (3 April 2014, 15.00). Height, z, is above snow-free ground. Circles are propeller observations, squares, sonic ones. Lines are profiles obtained fitting or interpolating propeller observations.

between log-log^2 and log-linear fits, only results from the first method are shown. However, considerations made for the first method can be fairly extended to the second.

The agreement between log-methods is in general good and increases as the observed profile follows more closely the logarithmic one. The large scatter between fit and splines gradients observed at level 4 [figure 3.6(d)-(e)] is due, very likely, to the sensitivity of fit-slopes to the fitting profile already observed at this level in the intercomparison between log-log^2 and log-linear fits [figure 3.6]. Quite remarkable is the consistency of log-log^2 and log-Bessel gradients at level 2 [figure 3.5(d)] and that of log-Bessel and log-finite gradients at level 6 [figure 3.7(f)], even if a very slightly positive bias (<1%) was noted, at this level, between log-Bessel and the others two methods for least logarithmic profiles [blue points in figure 3.7(d) and (f)].

Klipp and Mahrt (2004) compared gradients obtained from a local log-linear fit with those from finite and log-finite differences. Their data came from 12 observational levels from 1.5 to 55 m, the 11 levels from 5 to 55 m were equally spaced by 5 m. The local fit used observations from 4 adjacent levels. They found systematic differences (both positive or negative, depending on the level) between gradients from local fit and finite differences for the lowest levels ($z \leq 10$ m) and comparable results above. Smaller differences were also observed between log-finite differences and local fit gradients. Results from CCT data show biases between linear methods (Bessel splines and finite differences) and log-methods (fits, log-finite differences and log-Bessel splines) for the lowest levels ($z \leq 7.5$ m) in agreement with those of Klipp and Mahrt (2004).

Now we turn on observed deviations between log-linear and log-log^2 slopes at the intermediate sonic level [figure 3.6(a)]. Given a set of observations, the two fitting profiles are

$$y_a(z) = a_0 + a_1 z + a_3 \ln z \quad \text{and} \quad y_b(z) = b_0 + b_3 \ln z + b_4 \ln^2 z. \tag{3.23}$$

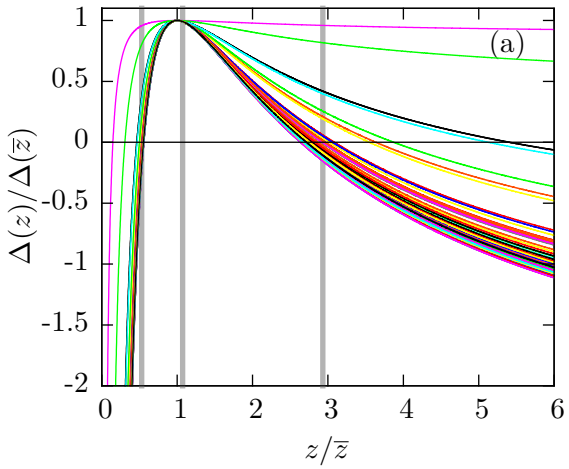

Figure 3.9: Normalized Δ-functions, $\Delta(z)/\Delta(\overline{z})$, against normalized height, $z/\overline{z}$, for 115 randomly selected profiles. Vertical lines are normalized heights of the three sonic levels.

Vertical gradients are obtained deriving (3.23) with respect to z:

$$\frac{dy_a}{dz} = a_1 + \frac{a_3}{z} \quad \text{and} \quad \frac{dy_b}{dz} = \frac{b_3 + 2b_4 \ln z}{z} \tag{3.24}$$

We define then a function, $\Delta(z)$, as the difference between log-linear and log-log^2 slopes:

$$\Delta(z) \equiv \frac{dy_a}{dz} - \frac{dy_b}{dz} = a_1 + \frac{a_3 - b_3 - 2b_4 \ln z}{z}. \tag{3.25}$$

For a logarithmic profile $a_1 = b_4 = 0$ and $a_3 = b_3$ from which $\Delta = 0$ for every z. In practice, however, this never happen although a_1 and b_4 can be very small and a_3 and b_3 very similar. $\Delta(z)$ has a stationary point in

$$\overline{z} = \exp\left(1 + \frac{a_3 - b_3}{2b_4}\right) \quad \text{such that} \quad \left.\frac{d\Delta}{dz}\right|_{\overline{x}} = 0 \quad \text{and with} \quad \Delta(\overline{z}) = a_1 - \frac{2b_4}{\overline{z}}.$$

From (3.25), Δ-functions were obtained from the coefficients of 115 randomly selected profiles belonging to the snow free stable dataset. In figure 3.9 these functions, normalized by their value at the stationary point, $\Delta(\overline{z})$, are plotted against the height normalized by the stationary point height, $z/\overline{z}$. All the normalized functions show a common behavior: $\Delta(z)/\Delta(\overline{x}) \to -\infty$ for $z \to 0$ as $\mathrm{O}(\ln z/z)$, reaches a maximum in $z = \overline{z}$ and then levels off around a negative value of the order of 1 for $x \to \infty$. For not normalized functions, $\Delta(x)$, the stationary point can be a positive maximum ($\Delta(\overline{x}) > 0$) or a negative minimum ($\Delta(\overline{x}) < 0$): in the latter case, the normalization implies a vertical reflection of the graph around the zero axis.

The median value of $\overline{z}$ considering all the 2900 profiles is about 7 m and for 70% of them, $\overline{z}$ fall into the range 6-8 m. Thus, maximum deviations between log-linear and log-log^2 slopes occur mostly near level 4 height (7.5 m). In figure 3.9, the heights of the three sonic levels (3.7, 7.5 and 20.5 m), normalized by $\overline{z} = 7$ m, are reported for comparison. Level 4 height falls indeed very near the height of maximum deviations (that can be both negative or positive). Instead, in general, much smaller deviations correspond to level 2 and level 6 heights. This explain the increased scatter observed in figure 3.6(a).

Δ-functions become more flat with less pronounced maximums (or minimums) as the observed profile follows more closely the logarithmic one: i.e. $a_1 \simeq 0$, $b_4 \simeq 0$ and $a_3 \simeq b_3$. The uppermost curves in figure 3.9, like the magenta and green ones, which display a very different behavior from the others, correspond just to this case. However, the behavior of normalized Δ-functions in such limit is very sensitive to the relative magnitude of a_1, b_4 and $a_3 - b_3$ leading to less similar curves.

3.6 Gradients sensitivity to displacement height

Snow height measurements at the CCT were intermittent and not always reliable making the height of observational levels above snow surface not known with sufficient accuracy.

In section 3.5 gradients were computed fitting or interpolating observations with the height above snow free ground (i.e. the nominal height of levels) as independent variable, without any correction for snow height. However, the analysis was carried out considering only those runs for which the snow height (at the CCT or at NMI's station) was below 20 cm. In this way, the obtained results should be almost free from snow height effects.

The best choice would have been to retain only those runs for which no snow cover was observed at CCT or at NMI's station: i.e., runs acquired from June to September. However too few runs satisfy this condition because stable conditions occur mostly during the permanent snow cover season: i.e., from October to May. Moreover, for subsequent analyses, also the threshold of 20 cm for snow height turned to be too restrictive. It was then decided to retain all runs acquired from June to November (included) and those acquired from 25 to the end of May 2012: during these periods, the snow height at CCT or at Ny-Ålesund's station was below 50 cm.

A shift in the height of all observational levels has not effect on gradients obtained from Bessel splines and linear finite differences because only the height differences between levels are considered in these two methods.

Instead, gradients obtained from methods that have a nonlinear behaviour in z (i.e., log-finite differences, log-Bessel splines, log-linear and log-log^2 fits) are affected by a shift in the vertical coordinate. This can be seen for a logarithmic profile. Let us suppose that the true profile is

$$y(z) = A + B \ln(z - d), \tag{3.26}$$

where z is the independent variable of interpolation (i.e., the height above snow free ground) and d is a displacement height (e.g., the snow height). Log-methods interpolate perfectly the true profile only when $d = 0$. Otherwise, deviations between the true and the interpolated profile and, then, the true and the computed gradients are expected.

Deviations between true and computed derivatives for a logarithmic profile as that in eq. (3.26) can be obtained easily for log finite differences. Given two observational levels at z_{n+1} and z_n, the computed gradient with log-finite differences at height $z_n \leq z \leq z_{n+1}$ is

$$\left(\frac{dy}{dz}\right)_{\text{comp}} = \frac{y_{n+1} - y_n}{\ln z_{n+1} - \ln z_n} \frac{1}{z} \tag{3.27}$$

where $y_n = y(z_n) = A + B \ln(z_n - d)$. Then

$$\left(\frac{dy}{dz}\right)_{\text{comp}} = \frac{\ln(z_{n+1} - d) - \ln(z_n - d)}{\ln z_{n+1} - \ln z_n} \frac{z - d}{z} \left(\frac{dy}{dz}\right)_{\text{true}} \tag{3.28}$$

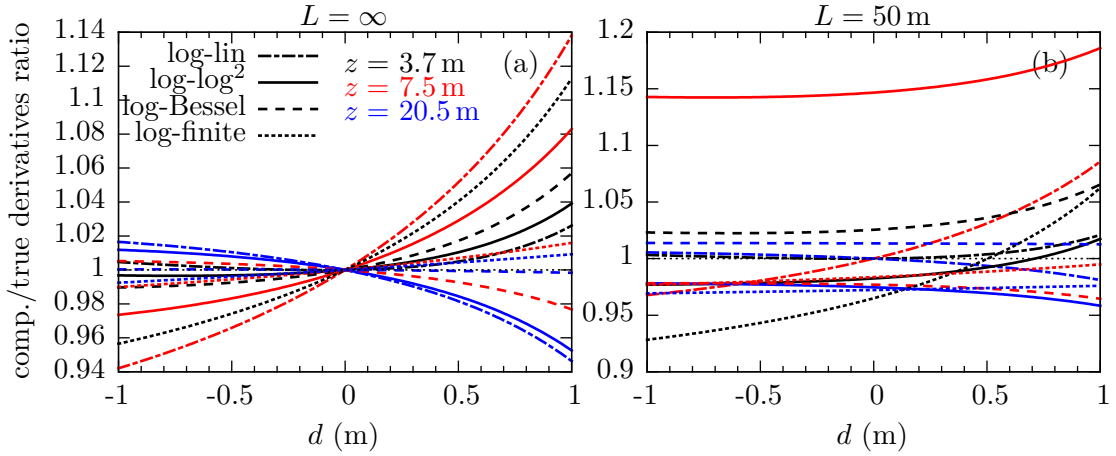

Figure 3.10: Ratios between computed and true derivatives for a logarithmic profile against displacement height for a logarithmic (a) and a log-linear (b) profile.

where

$$\left(\frac{dS}{dz}\right)_{\text{true}} = \frac{B}{z-d} \tag{3.29}$$

is the true gradient from eq. (3.26).

Even for a logarithmic profile, a relation similar to (3.28) cannot be easily derived for the other log-methods. However, as a sensitivity test, a comparison between computed and true gradients from a known profile with variable displacement height was carried out.

Observations at the four propeller levels ($z = 2$, 4.8, 10.3, 33.4 m) were generated from the log-linear profile

$$y(z) = \ln(z-d) + \alpha z. \tag{3.30}$$

Then gradients were computed at the three sonic levels ($z = 3.7$, 7.5, 20.5 m) fitting observations with log-linear and log-log^2 profiles, interpolating them with log-Bessel splines and with log-finite differences. This was done for values of d in the range $-1\,\mathrm{m} \le d \le 1\,\mathrm{m}$.

Taking $\alpha = \beta/L$, L the Obukhov length, (3.30) is the normalized wind speed profile for the horizontally homogeneous, stationary, weakly stable surface layer over flat terrain (except for a constant, but computed gradients do not depend on constants in the interpolated profile):

$$y(z) = \frac{\kappa}{u_*}\overline{U}(z) + \text{const.} \tag{3.31}$$

Then derivatives of (3.30) are related to normalized wind shears for nearly-neutral or weakly stable conditions:

$$\frac{dy}{dz} = \frac{\kappa}{u_*}\frac{d\overline{U}}{dz} = \frac{1}{z-d} + \alpha. \tag{3.32}$$

Two cases were analyzed: a logarithmic profile, obtained for $\alpha = 0$ in (3.30) and a log-linear profile, obtained from $\alpha = \beta/L$, $\beta = 4.7$ (Businger et al., 1971) and $L = 50\,\mathrm{m}$ in (3.30). The ratio between the computed gradients with the four log-methods and the true ones (3.32) for the three sonic level heights and the two profiles are presented in fig. 3.10.

For the sake of simplicity, hereafter $z - d$ will be called "true height" and z "nominal height". In fig. 3.10 also the case for which the true height is greater than the nominal one ($d < 0$) is shown. However, for the snow height effect $d > 0$. For both the logarithmic

(fig. 3.10(a)) and the log-linear profile (fig. 3.10(b)) deviations between the computed and the true gradients are below $\sim 5\%$ for $d < 0.5\,\mathrm{m}$ for all log-methods and at all sonic levels. An exception are gradients computed with log-log^2 fit at the middle sonic level ($z = 7.5\,\mathrm{m}$) for the log linear profile which showed deviations of more tha 15%: uppermost red solid curve in fig. 3.10(b). This is another manifestation of the deviations between log-log^2 and log-linear profiles that were already observed at this height during the gradients intercomparison in section 3.5.

For logarithmic profiles (fig. 3.10(a)) differences between computed and true gradients are greater for $d > 0$: i.e., when the nominal height underestimates the true height. The sensitivity of the computed gradients to the displacement height decreases with decreasing d for both log and log-linear profiles. However this is much more evident for the log-linear one (fig. 3.10(b)) because as d becomes more and more small (or even negative) the linear behaviour, which does not depend on d, dominates on the logarithmic one (eq. (3.32)).

Log-Bessel gradients are almost identical to the true ones for the highest sonic levels ($z = 20.5\,\mathrm{m}$) and the logarithmic profile for the whole range of displacement height considered: blue dashed line in fig. 3.10(a). Considering all the three levels, among the four methods, log-Bessel splines seem to perform better.

Obviously, for log-linear profiles, better performances are obtained with a log-linear fit although a greater sensitivity to the displacement height was observed for the middle level ($z = 7.5\,\mathrm{m}$): dot-dashed red curve in fig. 3.10(b). Also in this case performances of log-Bessel splines are overall good.

Snow height measurements at the CCT were intermittent and considered not reliable since October 2013. When the snow measurements at the CCT were not available, daily observations from the station of the Norwegian Meteorological Institute (NMI) in Ny-Ålesund were employed. The station is located west of the village at about 2 km from the CCT's site. When both observations were available, differences of the order of 10 cm were observed between the snow height measured at the CCT and at NMI's station. These differences are of the order of the accuracy with which can be determined the height above the snow-free ground, z, due to the irregularity of the terrain near the CCT. Higher differences of about 40 cm were observed in March 2014. However, very few snow height measurements were taken at the CCT in winter 2013-2014 and doubts are present on their reliability.

The best choice would have been to exclude all runs with snow covered ground and then computes gradients taking as independent variable the height above snow-free ground (the nominal height). However, this would have excluded too many stable runs which occur mostly during the permanent snow cover season.

It was decided then to compute gradients (and fit or interpolation coefficients) taking as independent variable the height above snow-free ground, without any correction for the snow depth, and limiting the analysis to runs for which the snow height (at the CCT or at NMI's station) was below 50 cm. For doing this, all runs acquired from January to May 2014 were excluded from the analysis.

3.7 Sensitivity of dimensionless gradients to displacement height

The true and the computed dimensionless wind shears are

$$\phi_m^{\text{true}} = \frac{\kappa(z-d)}{\tau^{1/2}}\left(\frac{d\overline{U}}{dz}\right)_{\text{true}} \quad \text{and} \quad \phi_m^{\text{comp}} = \frac{\kappa z}{\tau^{1/2}}\left(\frac{d\overline{U}}{dz}\right)_{\text{comp}} \tag{3.33}$$

where z is the nominal height (used in the computation of the gradients), d is the difference between the nominal and the "true height" above ground (i.e., the displacement height) and, for the sake of brevity, we have put $\Omega \equiv d\overline{U}/dz$. From (3.33), the relative error in the computed dimensionless shear is

$$\epsilon_{\phi_m} = \epsilon_z + \epsilon_{d\overline{U}/dz} + \epsilon_z\epsilon_{d\overline{U}/dz}, \tag{3.34}$$

where

$$\epsilon_{\phi_m} = \frac{\phi_m^{\text{comp}} - \phi_m^{\text{true}}}{\phi_m^{\text{true}}}, \quad \epsilon_z = \frac{d}{z-d} \quad \text{and} \quad \epsilon_{d\overline{U}/dz} = \frac{(d\overline{U}/dz)_{\text{comp}} - (d\overline{U}/dz)_{\text{true}}}{(d\overline{U}/dz)_{\text{true}}}$$

are relative errors in dimensionless gradients, height above ground (or above zero plane) and gradients, respectively. Supposing that both the relative error for the height above ground and that for the wind shear are small ($\ll 1$) we can neglect the product in the right side of (3.34) and write

$$\epsilon_{\phi_m} \approx \epsilon_z + \epsilon_{d\overline{U}/dz}. \tag{3.35}$$

In ϕ_m vs. z/Λ plots, errors in the estimation of the height above ground (or above zero-plane) have different effects depending on the similarity relationship followed by the true gradients (supposing that they follow one) and hence on stability.

Let us suppose that the true dimensionless wind shear follows a similarity relation and can be expressed as a function of the true stability parameter: $\phi_m^{\text{true}} = \phi_m^{\text{emp}}((z-d)/\Lambda)$, where ϕ_m^{emp} is some empirical function. When the estimated height and the true height coincide, $d = 0$, $\phi_m^{\text{comp}} = \phi_m^{\text{true}}$ and the computed points collapse onto the empirical function

$$\phi_m^{\text{comp}} = \phi_m^{\text{emp}}(z/\Lambda).$$

However, when a displacement height is present, in the ϕ_m–z/Λ plane (where z is the incorrect height) the computed points moves from $(z/\Lambda, \phi_m^{\text{emp}}(z/\Lambda))$ to $(z/\Lambda+\delta(z/\Lambda), \phi_m^{\text{emp}}(z/\Lambda)+\delta\phi_m)$ where

$$\delta(z/\Lambda) = \epsilon_z(z/\Lambda) \quad \text{and} \quad \delta\phi_m = \epsilon_{\phi_m}\phi_m^{\text{emp}}(z/\Lambda). \tag{3.36}$$

This means that because of errors in estimated height, the computed point moves along straight lines passing through the origin ($z/\Lambda = 0, \phi_m = 0$) and with slope

$$\frac{\delta\phi_m}{\delta(z/\Lambda)} = \frac{\phi_m^{\text{emp}}(z/\Lambda)}{z/\Lambda}\left(1 + \frac{\epsilon_{d\overline{U}/dz}}{\epsilon_z}\right) \tag{3.37}$$

obtained from (3.36) and (3.34).

Supposing that the true (empirical) similarity function is linear,

$$\phi_m^{\text{emp}}(z/\Lambda) = 1 + \beta_m(z/\Lambda), \tag{3.38}$$

from (3.36) we have that

$$\frac{\delta\phi_m}{\delta(z/\Lambda)} = \left(\frac{\Lambda}{z} + \beta_m\right)(1+\alpha) \tag{3.39}$$

where $\alpha = \epsilon_{d\overline{U}/dz}/\epsilon_z$ is the ratio between relative errors in gradients and height. From (3.39) we see that when errors in gradients are much smaller that errors in height, i.e. $\alpha \simeq 0$, the computed point moves in a direction which becomes more and more aligned with true relation as stability increases. Then in this special case errors have lesser influence on the similarity relation as stability increases. This is not surprising because (3.38) predicts the existence of a z-less regime for $z/\Lambda \gg 1$ for which the height above ground is not a scaling variable anymore. The fact that errors in the height above ground can have not any effect on similarity relationships is another manifestation of self correlation that affects ϕ_m vs. z/Λ plots, this time because of the shared variable z.

For a linear similarity function as that of eq. (3.38) and $\alpha = 0$

$$\phi_m^{\text{comp}} = \frac{z}{z-d}\phi_m^{\text{emp}}\left(\frac{z-d}{\Lambda}\right) = \frac{z}{z-d} + \beta_m\frac{z}{\Lambda}. \tag{3.40}$$

It must be noted that d can change between computed points, as snow height changes between different runs, making its effect on similarity relationships more difficult to detect.

At the lowest sonic level, $z = 3.7\,\text{m}$, for $d = 0.5\,\text{m}$ $\epsilon_z = 16\%$ and, for a logarithmic profile (see fig. 3.10) α ranges from about 0.05 to 0.25, depending on the used methods in the gradients calculation; at the same height, but for $d = 1\,\text{m}$, $\epsilon_z = 37\%$ and α is between about 0.1 and 0.3. At the middle sonic level, $z = 7.5\,\text{m}$, $\epsilon_z = 7\%$ for $d = 0.5\,\text{m}$ and α varies between about -0.1 to 0.9; α varies almost in the same range for $d = 1\,\text{m}$, $\epsilon_z = 15\%$. At the highest level, $z = 20.5\,\text{m}$, $\epsilon_z = 2.5\%$ and α is between -0.8 and 0.4 for $d = 0.5\,\text{m}$; for $d = 1\,\text{m}$, $\epsilon_z = 5\%$ and α is about in the same range. Therefore, considering errors in gradients due only to errors in the estimation of the height above snow-covered ground (or zero plane) the assumption that $\alpha \simeq 0$ is not fulfilled at all heights and for all computation methods. This complicates further the estimation of errors in dimensionless gradients due to snow height.

Chapter 4

Wind speed flux-gradient relationships for the CCT dataset

This chapter is about the main argument of the work: the relation between the dimensionless wind speed gradient, ϕ_m, and the local stability parameter, z/Λ, for the CCT dataset for the stably stratified boundary layer. Several formulations were proposed since the 1968 Kansas experiment (Businger et al., 1971; Haugen et al., 1971),where for the first time flux-gradient relationships were obtained from direct measures of turbulent fluxes, to the present (e.g. Beljaars and Holtslag, 1991; Businger et al., 1971; Cheng and Brutsaert, 2005a; Grachev et al., 2007b; Högström, 1988, 1996; Sorbjan and Grachev, 2010). These formulations (empirical functions) differ significantly only for very stable conditions (i.e. $z/\Lambda \gtrsim 1$). Furthermore, they are derived from observational campaigns made over almost-flat and homogeneous terrains, which are among assumptions contained in Monin-Obukhov similarity theory and in its local equivalent, that is adopted in this study.

However, most real surfaces are not flat nor homogeneous. The question arise then if local similarity theory still works above complex terrains and heterogeneous surfaces. The CCT is located in an arctic fjord surrounded by mountains few kilometers far from the tower, i.e. the perfect site to test the limits of validity of local similarity theory. In this chapter, result from the CCT dataset are presented in attempt to answer this question.

After a brief discussion in section 4.1 about the choice of considering wind speed gradients instead of wind shear (in the rest of the chapter the terms "wind shear" and "wind gradient" will be used almost equivalently), criteria for data selection to reduce the scatter in similarity plots are presented in section 4.1. In particular, wind direction, to exclude tower perturbed flows, and wind speed, to exclude weak turbulence, are considered.

In section 4.3, plots of ϕ_m against z/Λ are presented for all selected runs, with a further subdivision in wind direction sector, each of which having its own peculiar topographic and surface characteristics. In section 4.4, the possible origin of observed deviations of ϕ_m for low z/Λ are analyzed and, finally, in section 4.5 the apparent failure of local similarity theory for the CCT dataset is discussed.

4.1 Wind shear and wind speed gradient

The dimensionless wind shear is defined as (e.g., Sorbjan, 1986; Sorbjan and Grachev, 2010; Stull, 1988):

$$\phi_m \equiv \frac{\kappa z}{\tau^{1/2}} \left[\left(\frac{d\overline{u}}{dz} \right)^2 + \left(\frac{d\overline{v}}{dz} \right)^2 \right]^{1/2}, \tag{4.1}$$

where $\tau = [(\overline{u'w'})^2 + (\overline{v'w'})^2]^{1/2}$ is evaluated at the surface or at the height z if surface or local scaling is adopted, respectively. Definition (4.1) can be rewritten in term of the vertical gradient of the wind velocity modulus, $d\overline{U}/dz$, and the directional shear, $d\overline{\gamma}/dz$, considering that

$$\overline{u} = -\overline{U}\sin\overline{\gamma} \quad \text{and} \quad \overline{v} = -\overline{U}\cos\overline{\gamma}, \tag{4.2}$$

where $\overline{U} = (\overline{u}^2 + \overline{v}^2)^{1/2}$ and $\overline{\gamma}$ is the mean wind direction measured clockwise from north. Indeed, substituting (4.2) in (4.1) we have

$$\phi_m = \frac{\kappa z}{\tau^{1/2}}\left[\left(\frac{d\overline{U}}{dz}\right)^2 + \overline{U}^2\left(\frac{d\overline{\gamma}}{dz}\right)^2\right]^{1/2}. \tag{4.3}$$

Many authors (eg., Businger et al., 1971; Grachev et al., 2007b; Högström, 1988; Yagüe et al., 2006) use the definition

$$\phi_m \equiv \frac{\kappa z}{\tau^{1/2}}\frac{d\overline{U}}{dz} \tag{4.4}$$

that coincides with (4.1) or (4.3) when the directional shear is negligible. These authors usually rotate the reference frame along the wind direction taking $\tau = |\overline{u'w'}|$ (e.g., Grachev et al., 2007b) or $\tau = [(\overline{u'w'})^2 + (\overline{v'w'})^2]^{1/2}$ (e.g., Yagüe et al., 2006) where now u' and v' are the fluctuations of the velocity components along and transverse to the mean wind direction, respectively. The first choice is motivated by the assumption that $|\overline{u'w'}| \gg |\overline{v'w'}|$.

Always in the present work, because no axes rotation was carried out, the definition $\tau = [(\overline{u'w'})^2 + (\overline{v'w'})^2]^{1/2}$ is used, being u' and v' the fluctuations of the eastward and northward wind components, respectively. Furthermore, the mean wind speed $\overline{S} = \overline{[u^2 + v^2]^{1/2}}$ instead of the mean wind velocity, $\overline{U}$, was used for the computation of wind shear both in (4.1) or in (4.3), because only the first was available from propeller anemometers. However, as was demonstrated in section 3.1, $\overline{U} \approx \overline{S}$ is a good approximations in many cases eventually leading to slightly overestimations ($< 5\%$) of dimensionless gradients.

4.2 Data selection by wind speed and direction

Dimensionless wind shears were derived at all the three sonic levels ($z = 3.7$, 7.5, 20.5 m) using (4.4) and calculating wind speed gradients with the four log-methods: log-linear and log-log^2 fits, log-Bessel splines and log-finite differences. Interpolated profiles, gradients ($d\overline{S}/dz$), dimensionless wind shears (ϕ_m) and stability parameters (z/Λ) were all derived using the nominal height of each level, without any correction for the snow depth. The analysis was carried out on runs belonging to the 1h-truly-stable dataset, excluding those acquired from January to May 2014, in order to limit the effect of snow height. Local scaling is adopted: both ϕ_m and Λ were derived from fluxes obtained with the eddy correlation method and 10-min averages at the considered sonic level.

To reduce scatter in ϕ_m vs. z/Λ plots, runs were selected considering wind speed and direction. The improvement from this selection is evident in fig. 4.1 where runs are subdivided in three classes:

1. "tower perturbed", if the wind direction at one or more propeller levels was in the range 150°–300°;

2. "weak winds", if the wind direction was outside the range 150°–300° at all propeller levels and $\overline{S} < 3\,\mathrm{m\ s^{-1}}$ at one or more propeller levels;

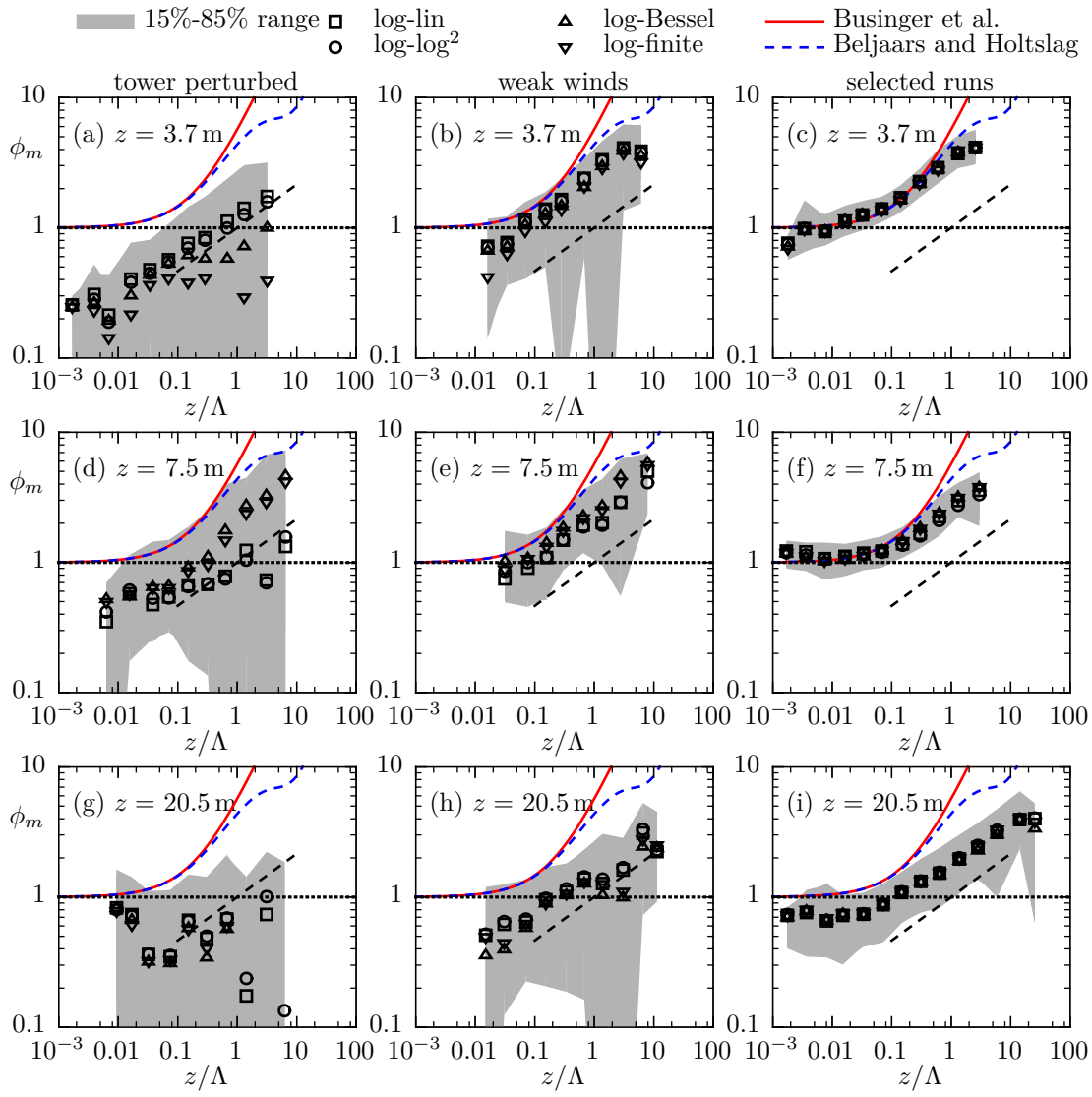

Figure 4.1: Dimensionless wind shears computed with the four log-methods against stability parameter for the three sonic levels. Data are stratified by wind direction and speed. Open symbols are bin medians, shaded areas represent the maximum 15th-75th percentile range considering all methods. Also shown are similarity functions from Businger et al. (1971) and Beljaars and Holtslag (1991). Dashed lines indicate the $(z/\Lambda)^{1/3}$ behaviour.

3. "selected runs", if wind direction was outside the sector 150°–300° and $\overline{S} \geq 3\,\mathrm{m\ s^{-1}}$ at all propeller levels.

For each class (columns), sonic level (rows) and log-method, data are collected in intervals of stability (z/Λ): three intervals per decade of z/Λ of equal width in $\log(z/\Lambda)$. For each interval, "bin", the median values of ϕ_m and z/Λ, and the 15th–85th percentiles of ϕ_m were derived. In fig. 4.1, open symbols are bin medians (for both z/Λ and ϕ_m) for each method. The shaded areas extend from the minimum 15-th percentile to the maximum 85th percentile among all methods for the same bin. This area is an indication of the spread of the data. Also shown in fig. 4.1 are similarity relationships from Businger et al. (1971) and Beljaars and Holtslag (1991). In all plots both axes have logarithmic scales.

The starting dataset was composed by 3598 10-min runs, 520 (14%) of them were classified as tower-perturbed, 383 (11%) as weak-wind conditions and the remaining 2695 (75%) were the selected ones. It must be noted that tower-perturbed runs were mostly characterized by weak-wind conditions because weak winds were dominant in that direction sector (see fig. 2.4). Hence, these two classes are not mutually exclusive.

The agreement between methods is high for selected runs at all three sonic heights and for the whole observed stability range (fig. 4.1(c),(f) and (i)). Greater deviations were observed for weak-winds (fig. 4.1(b),(e) and (h)) and, especially, for tower-perturbed flows (fig. 4.1(a),(d) and (g)). Generally, large differences among methods are associated with an increase of data scatter (shaded areas in fig. 4.1). Furthermore, particularly in these two classes, the agreement is better between methods of the same type: log-lin and log-log[2] fits; log-Bessel splines and log-finite differences. The different behaviour of global vs. local methods (i.e., fits vs. interpolations) indicates that complex structures appear in the wind profile in weak-wind and tower-perturbed conditions (see fig. 3.8(b), for an example). This can leads to poorly determined, very small or even negative wind speed gradients.

A reduction in the scatter of data was observed for the selected runs with respect to both tower-perturbed and weak-winds conditions for all the three sonic levels: this is indicated by lesser vertical extension of the shaded area in plots (c), (f) and (i) of fig. 4.1. Lesser scatter in ϕ_m vs. z/Λ plots suggests a greater correlation between dimensionless gradients and stability parameter. However this does not automatically mean that a flux-gradient relationship exists because of self-correlation that affects ϕ_m vs. z/Λ plots (Baas et al., 2006; Klipp and Mahrt, 2004).

The behaviour of bin medians observed for weak-wind conditions (fig. 4.1(b), (e) and (h)) can just be explained by self-correlation due to the shared variable τ which is present in both ϕ_m and Λ. Indeed, $\phi_m \propto \tau^{1/2}$ and $\Lambda \propto \tau^{3/2}$. Then, if the wind shear, $d\overline{S}/dz$, is uncorrelated with the local friction velocity, $\tau^{1/2}$, the behaviour $\phi_m \sim (z/\Lambda)^{1/3}$ is observed (this behaviour is represented by the dashed straight lines in fig. 4.1). A similar behaviour can be observed also for tower-perturbed flows in fig. 4.1(a) and, although with a slightly smaller slope, for selected runs at the highest level, in fig. 4.1(i).

Although the threshold of $3\,\mathrm{m\ s^{-1}}$ for the wind speed is quite arbitrary and chosen from a trade-off between scatter reduction and number or retained runs, it seems to discriminate quite well between cases when a flux-gradient relation exists and those when it does not. Argentini et al. (2012) observed that when the wind speed overpassed $3\,\mathrm{m\ s^{-1}}$ a transition between a wavy stratified nocturnal surface layer with light turbulence to a more mixed turbulent layer occurred. Liang et al. (2014) found that a wind speed of $3\,\mathrm{m\ s^{-1}}$ separates a regime with stationary turbulence, for which MOST holds, from a regime where nonstationary motions are dominant, turbulence is independent of the mean flow and MOST may not holds.

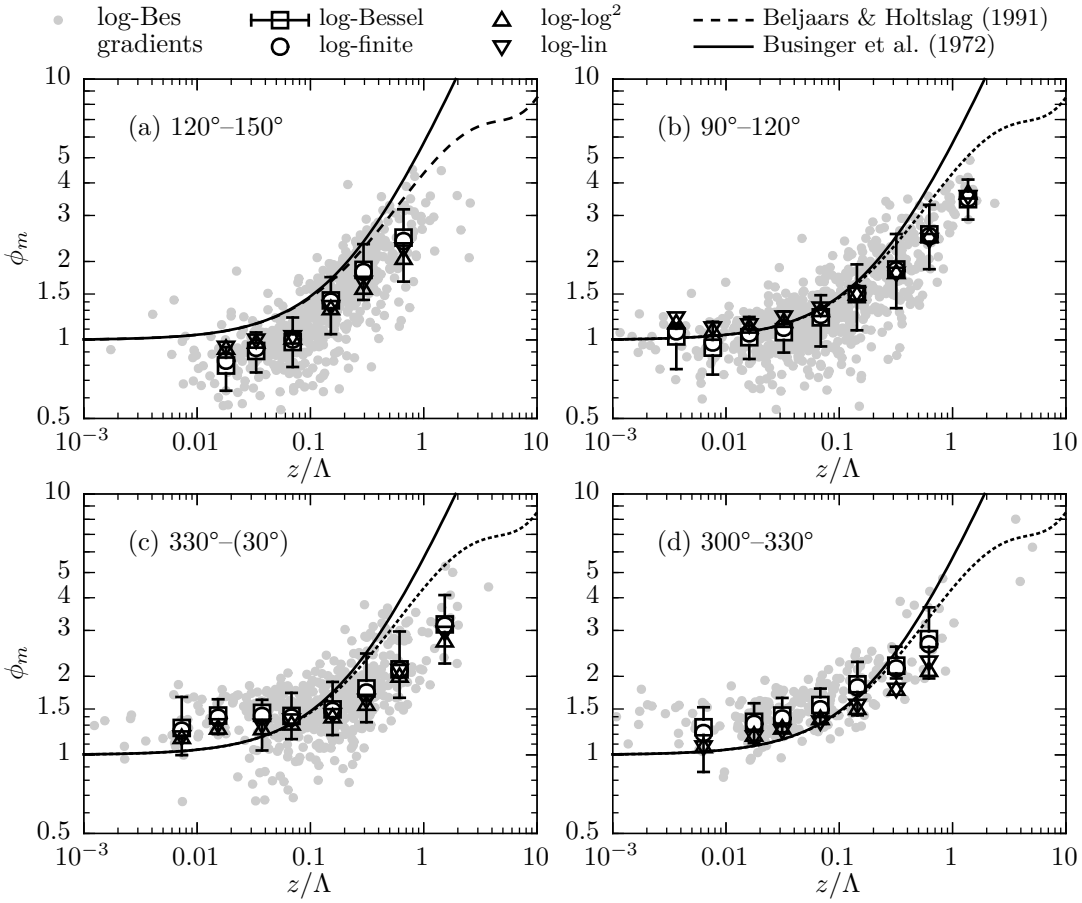

Figure 4.2: Comparison between ϕ_m obtained evaluating gradients with the four log-methods at $z = 7.5\,\mathrm{m}$ and for each wind direction sector: open symbols are bin medians; single data points and 15th–85th percentile range (error bars) refer to log-Bessel splines only.

Klipp and Mahrt (2004) retained only cases for which $d\overline{S}/dz \geq 0.001\,\mathrm{m\ s^{-1}}$ because small gradients are usually poorly determined (Salesky and Chamecki, 2012). In this study, all selected runs satisfy this condition at the lowest two sonic levels. At the highest one, very few negative gradients ($\sim 0.1\%$ of the total, depending on computation method), of the order of $-0.01\,\mathrm{m\ s^{-1}}$, were observed. Anyway, no data selection by wind speed gradients was adopted.

4.3 ϕ_m vs. z/Λ plots for different wind direction sectors

Selected runs were furthermore subdivided into four wind direction sectors: 120°–150°, 90°–120°, 30°–330° and 300°–330°. The original idea was to subdivide the less tower-perturbed sector (300°-150°) into 7 sectors, each 30°-wide. However, too few runs would have fallen into sectors around north. For this reason, only one sector 60°-wide from 30° to 330° was considered. Wind directions from 60° to 90° were excluded from the analysis because too few runs belonged to this sector and because some of them shows anomalous results at the lowest sonic level, maybe due to the influence of the small house hosting computers connected with the CCT's instrumentation. A separate analysis for each sector is advisable in a complex terrain as that of the CCT's site, because fetch and topography change as

direction change. The north-sector is characterized by sea-land transitions and terrain slopes oriented along the cross-wind direction (see section 2.2.1). In the east-southeast and northwest sectors, topographic effects should dominate because of the presence of mountains some kilometers far from the tower.

On average, no significant deviations between dimensionless gradients computed with the four log-methods were observed at the lowest ($z = 3.7\,\mathrm{m}$) and the highest ($z = 20.5\,\mathrm{m}$) sonic levels. Differences of the order of 10%–20% were instead observed for the middle sonic level ($z = 7.5\,\mathrm{m}$) between global (log-log^2 and log-linear fits) and local methods (log-Bessel splines and log-finite differences). This level as yet shown to be the most sensitive to the computation method (section 3.5).

The sensitivity of ϕ_m to the computation method for the middle sonic level is shown in fig. 4.2. For each wind direction sector results are presented as bin medians: as for fig. 4.1, data were subdivided in three intervals (bins) per decade of z/Λ and median values computed for both ϕ_m and z/Λ. Only median values for bins containing at least 5 data points are shown. Single data points and the 15th-85th percentile range for each bin are shown for gradients computed with log-Bessel splines only, to give an idea of the typical spread of data, which is quite similar for the other methods.

For the 90°-120°-sector (fig. 4.2(b)) and $z/\Lambda \lesssim 0.04$, gradients from log-linear fit cluster slightly above ($\lesssim 10\%$) and those from log-Bessel splines slightly below the theoretical relation, with better agreement for log-log^2 fit and log-finite differences. For higher stabilities ($z/\Lambda \lesssim 0.04$) gradients from all methods collapse on the same curve. Differences between methods in near-neutral conditions reflect deviations of the true profile from the logarithmic one. In the case of fig. 4.2(b), differences between methods are in agreement with the presence of a small positive displacement height (see fig. 3.10(a)). For the 300°-330°-sector (fig. 4.2(d)), gradients from splines or log-differences are always above those from fits. Relative deviations between global and local methods are almost constant with stability. The presence of a positive displacement height to explain observed differences between computed and theoretical ϕ_m for near neutral conditions (i.e. $\phi_m(z/\Lambda = 0) > 1$) seem to be discarded by between-methods differences, that are opposite to those expected in this case (see fig. 3.10(a)).

For other sectors (fig. 4.2(a)-(c)), between-methods differences are lesser systematic although a slightly better agreement among computed and theoretical ϕ_m for $z/\Lambda \lesssim 0.03$ is observed when fits, instead of local methods, are employed.

In general, dimensionless gradients from global fits collapse nearer to theoretical relationships that those from local methods (splines or log-differences) for near neutral conditions (i.e. $z/\Lambda \lesssim 0.03$). This can be explained by a smaller sensitivity of global methods (fits) to deviations of the observed profile to the logarithmic one, maybe due to the formation of internal boundary layers because of complex terrain. Klipp and Mahrt (2004) observed that $\phi_m(z/\Lambda = 0) \neq 1$ when finite or log-finite differences were employed for the calculation of gradients, with both positive or negative biases, depending on level, for $z \lesssim 10\,\mathrm{m}$.

In fig. 4.3, dimensionless wind speed gradients, from log-Bessel splines, against stability parameter are shown for selected runs at the three sonic levels and for each wind direction sector as bin medians and 15th-85th percentile range. For comparison, statistics for data from all sectors (which were yet presented in fig. 4.1(c), (f) and (h)) are also reported along with similarity functions from Businger et al. (1971) and Beljaars and Holtslag (1991).

A comparison between local scaling (fig. 4.3(a)-(c)) and "surface" scaling (fig. 4.3(d) and (e)) is also carried out: in the first case ϕ_m and Λ are computed from fluxes measured

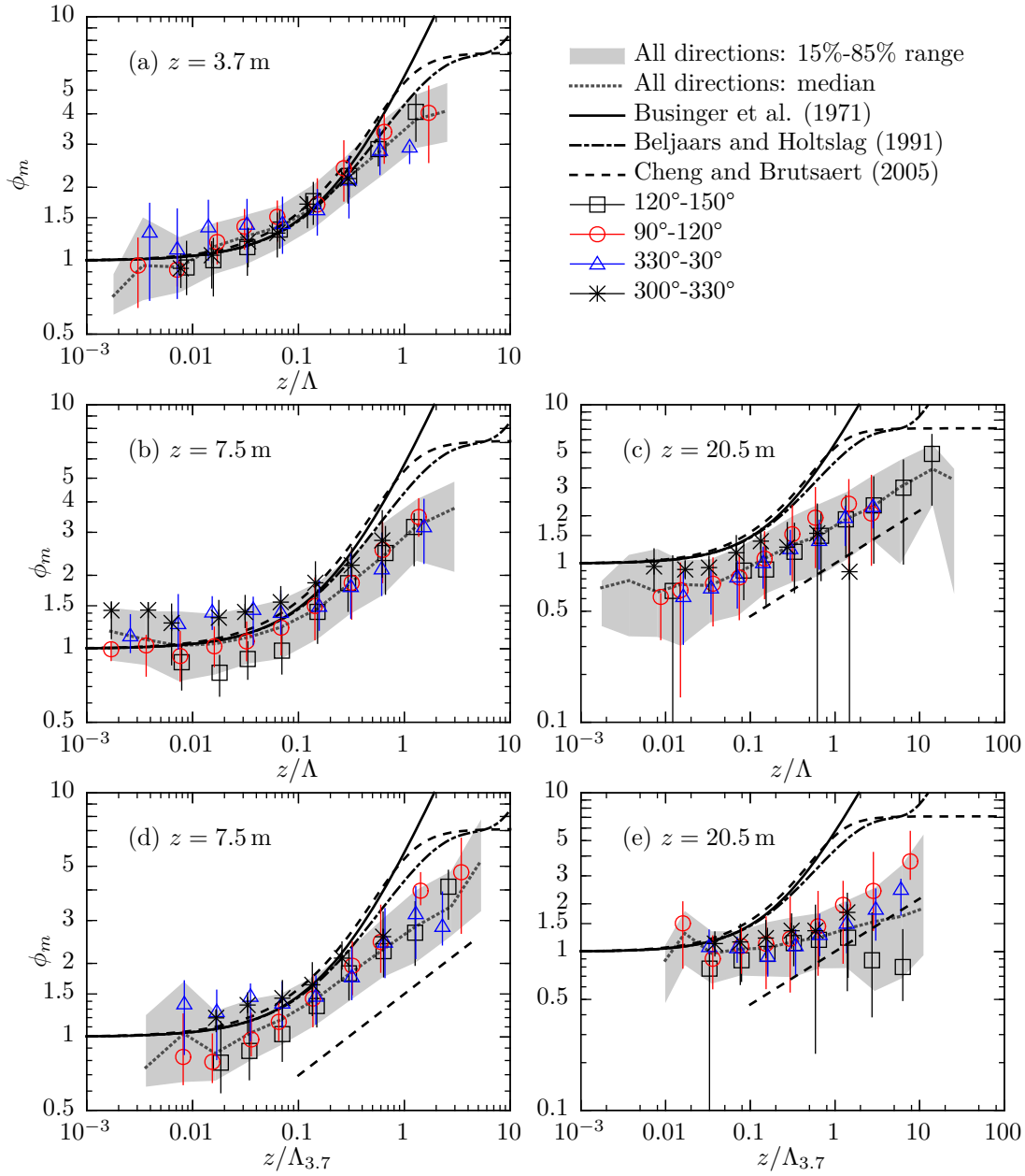

Figure 4.3: ϕ_m against z/Λ for each sonic level and wind direction sector: along with bin medians (open symbols) and 15th-85th percentile ranges (error bars) for each sectors, those for all sectors (dotted lines and shaded areas) are shown for comparison. In (d) and (e) surface scaling is adopted. The dashed straight line in (c), (d) and (e) indicates the $\phi_m \propto (z/\Lambda)^{1/3}$ behaviour.

at the considered level, in the second, from fluxes at the lowest sonic level ($z = 3.7\,\mathrm{m}$). It must be stressed, however, that the use of the word "surface" can be misleading because the lowest level can be or not be in the surface-layer which can even not be present at all.

Differences between ϕ_m from different direction sectors were observed in the weakly stable and near neutral range, i.e. for $z/\Lambda \lesssim 0.1$, particularly at the middle sonic level (fig. 4.3(b)) and, to a lesser extent, at the lowest one (fig. 4.3(a)). For $z/\Lambda \gtrsim 0.1$, instead, data from different sectors collapse almost on the same curve. At the highest level (fig. 4.3(b)), observations from different sectors lie almost on the same curve for the whole stability range, with the exception of the 300°-330°-sector.

The greatest agreement between observed and expected ϕ_m from most employed empirical curves (i.e. Beljaars and Holtslag (1991) and Businger et al. (1971)) was found for the lowest level (fig. 4.3(a)) and the 300°-330°-sector, which showed also the smallest range of variation of z/Λ. For south-east sectors (i.e. 120°-150° and 90°-120°), at the same level, the agreement is good up to $z/\Lambda \lesssim 0.5$. Beyond, observed ϕ_m increases slower with z/Λ and seems to level-off around the value of 4. However, too few data points with $z/\Lambda > 1$ do not permit a fairly assessment of this level-off, as that proposed by Cheng and Brutsaert (2005a) although around a smaller value of ϕ_m. In the near-neutral limit, i.e. for $z/\Lambda \to 0$, observed dimensionless gradients are both smaller or greater than the theoretical value of 1, depending on the direction sector: south-eastern sectors showed values of ϕ_m below the theoretical one, around 0.9; for the northern sector (330°-30°), instead, ϕ_m leves-off around 1.5 for $z/\Lambda \lesssim 0.05$.

Between-sectors differences in the near-neutral and weakly-stable range increases at the middle sonic level (fig. 4.3(b)) with south-eastern sectors showing values below, and northern and north-western sectors above, the expected ones. With the exception of the 90°-120°-sector for $z/\Lambda \lesssim 0.1$, observed ϕ_m from any of the sectors do not follow closely expected similarity functions. Other interesting features at this level are the systematically higher ϕ_m observed for the 300°-330°-sector in the weakly-stable-near-neutral range, and the minimum in observed ϕ_m around $z/\Lambda \simeq 0.01$-0.02 for south-eastern sectors. As for the lowest level, between-sectors differences decrease when $z/\Lambda \gtrsim 0.1$ and observed ϕ_m is lower and increases slower with z/Λ than expected ones although differences are smaller for the 300°-330°-sector.

With the exception of the 300°-330°-sector, observed values of ϕ_m are much smaller than expected ones for the whole stability range and follow more or less the relation $\phi_m \propto (z/\Lambda)^{1/3}$, although with a slightly smaller slope (fig. 4.3(c)). This behaviour indicates that self-correlation is present (chapter 5), that a flux-gradient relationship does not exist and that the observed correlation is a mathematical artifact due to the fact that the friction velocity enters in both the definition of ϕ_m and Λ. The fact that observed slope is slightly smaller than 1/3 is probably due to the higher range of variation of heat fluxes observed at this level (section 5.1) which increases the horizontal scatter of data points. Observations from the sector 300°-330° follow more closely expected similarity functions at least up to $z/\Lambda \simeq 0.1$.

4.4 Deviations between observed and expected ϕ_m for small z/Λ

The origin of between-sectors differences in the near-neutral range were inquired. Firstly, the hypothesis of the need of a displacement height was considered. In fig. 4.4, mean wind speed differences $\overline{S}(z) - \overline{S}(2\,\mathrm{m})$ for all runs such that $z/\Lambda \leq 0.02$ at the middle sonic level,

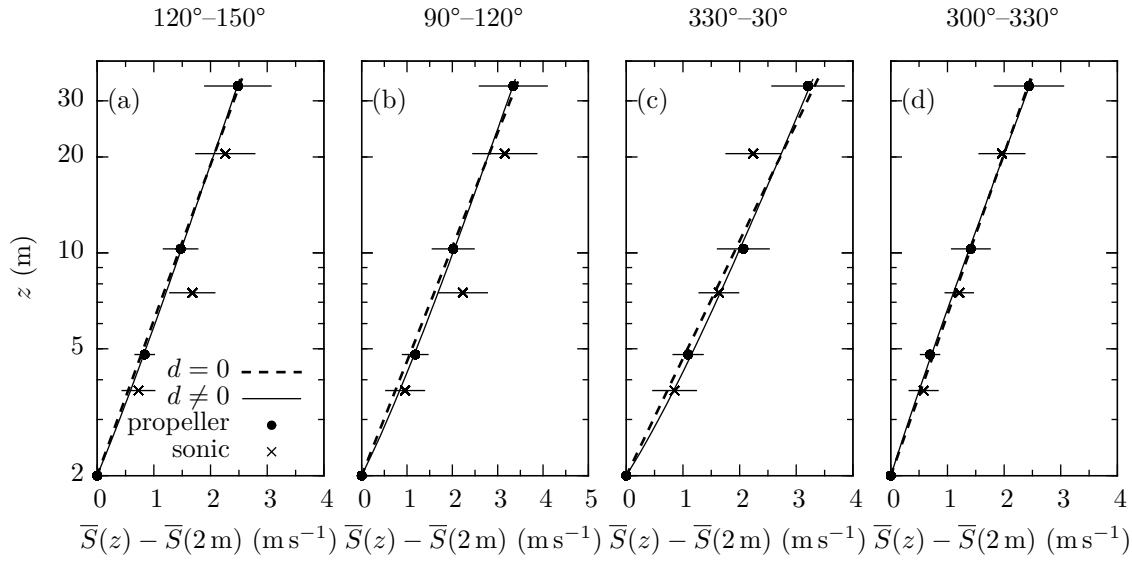

Figure 4.4: Vertical profiles of mean wind speed differences for all runs such that $z/\Lambda \leq 0.02$ at $z = 7.5\,\mathrm{m}$: mean values and between-runs standard deviations (error bars) along with log-fits for propeller means with and without a displacement height are shown.

which showed the largest deviations, are reported for all propeller and sonic levels on the CCT. Furthermore, propeller mean differences were fitted with a logarithmic profile with and without a displacement height and with the constraint of zero intercept a $z = 2\,\mathrm{m}$.

Propeller observations are well fitted by the logarithmic profile for each sector, with or without a displacement height (fig. 4.4). The fit-derived displacement heights are $d = 0.4 \pm 0.1\,\mathrm{m}$ for the sector 120°-150°, $d = 0.6 \pm 0.1\,\mathrm{m}$ for 90°-120°, $d = 0.7 \pm 0.3\,\mathrm{m}$ for 330°-30° and $d = -0.4 \pm 0.3\,\mathrm{m}$ for 300°-330°.

Observed deviations can be at least partially explained by a displacement height, maybe due to snow cover, only for the sector 330°-30°. Indeed, for this sector, most of near-neutral runs were acquired in November with snow-covered ground, although the snow height observed at Ny-Ålesund remained below 0.4 m. For $d = 0.7$, ϕ_m can be overestimated of about 20% and 10% at $z = 3.7\,\mathrm{m}$ and $z = 7.5\,\mathrm{m}$, respectively (eq. (3.35)). Differences between observed and expected ϕ_m in the near-neutral range are larger, of the order of 30%-40% (fig. 4.3(a)-(b)).

For the other sectors, observed deviations cannot be explained in term of a displacement height, both because they are larger for the middle sonic level (fig. 4.3(b)) than for the lowest one (fig. 4.3(c)) and because they have opposite sign with respect to the derived displacement heights.

The hypothesis that observed deviations were caused by turbulent fluxes that enter in the definition of both ϕ_m and Λ was also verified. Profiles for fluxes of momentum and heat, normalized by the value at 3.7 m, were derived in two cases: when $z/\Lambda \leq 0.04$ at 3.7 m and when $z/\Lambda \leq 0.04$ at 7.5 m (fig. 4.5).

For fluxes of momentum, the characteristics of an almost-constant-flux layer (i.e. of a surface layer) are better encountered for the wind sectors 90°-120° and 300°-330° (fig. 4.5(b) and (d)) although variations of more than 50% in 10-min fluxes occur for about 20% of the selected runs at $z = 20.5\,\mathrm{m}$,. For the sector 120°-150° (fig. 4.5(a)), fluxes at 7.5 m are, on average, 50% larger than those at 3.7 m when the selection at 7.5 m is considered (black circles). This can be responsible for the smaller than expected values of ϕ_m observed for

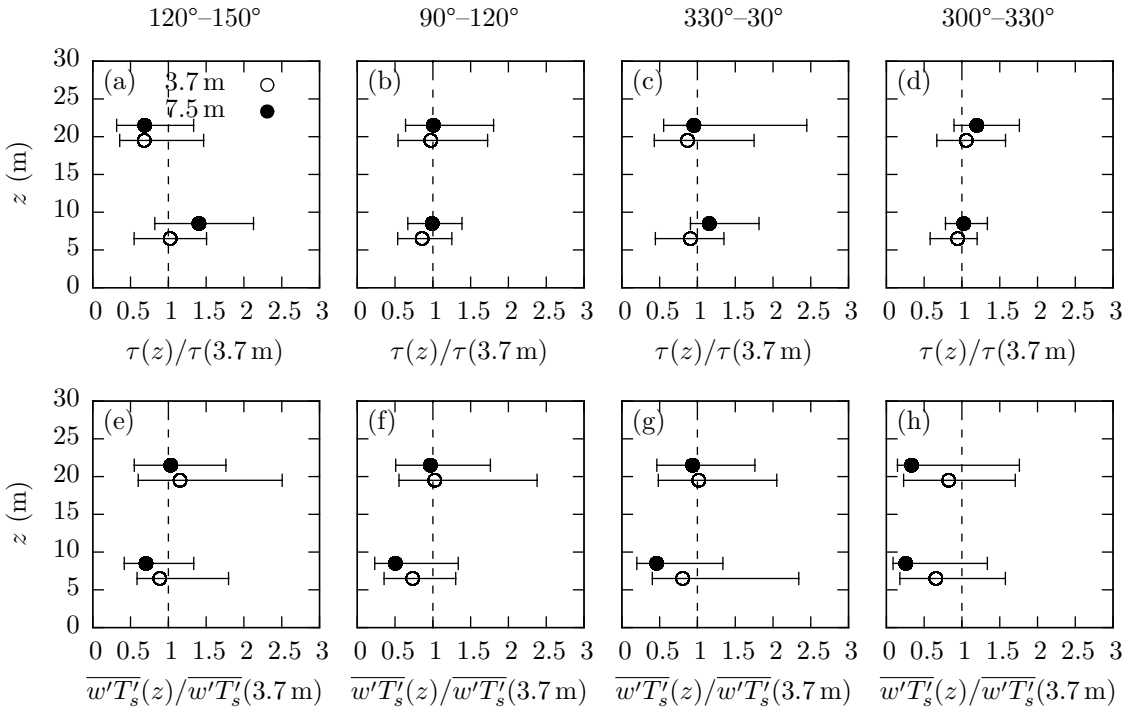

Figure 4.5: Vertical profiles for fluxes of momentum (first row) and heat (second row) normalized by the value at 3.7 m for all the runs such that $z/\Lambda \leq 0.04$ at 3.7 m (open circles) and at 7.5 m (filled circles): median values and 15th-85th percentile ranges (error bars) are shown. Symbols referring to the same level are slightly vertically displaced for a clearer representation.

this sector (fig. 4.3(b)).

For fluxes of heat, the signatures of an almost-constant-flux layer are encountered, on average, only for the sector 120°-150° (fig. 4.5(e)), although a large variability is present for 10-min values, with 30% of runs showing fluxes at 7.5 m 50%-below and 50 or 75%-above the 3.7-m value. Heat fluxes at 7.5 m are always smaller than those at 3.7 m for each direction sector indicating a possible underestimation at this sonic level, that has also shown large deviations in temperature measurements.

With respect to momentum fluxes, the variability of normalized heat fluxes (error bars) is greater, indicating a poorer correlation between values from different levels. This is because near-neutral conditions are characterized by small poorly determined heat fluxes and large better determined momentum fluxes (Baas et al., 2006; Salesky and Chamecki, 2012). The observed correlation between heat fluxes at 7.5 and 3.7 m is particularly low for the northern and north-western sectors (fig. 4.5(g) and (h)). A better correlation was instead observed between heat fluxes at 7.5 and 20.5 m when near-neutral runs were selected from z/Λ at 7.5 m (fig. 4.5(h), open circles).

For the sector 300°-330° (fig. 4.5(h)), heat fluxes at 7.5 and 20.5 m are a small fraction (25-30%, on average) of those measured at 3.7 m, when the condition $z/\Lambda \leq 0.04$ is imposed at the middle sonic level. This is also true when runs are selected from z/Λ at the highest sonic level (not shown). Fluxes of momentum, however, do not shown the same sensitivity to selection criteria (fig. 4.5(d)).

This means that near-neutral data points for this sector at both the middle (fig. 4.3(b)) and the highest (fig. 4.3(c)) sonic levels are characterized by anomalously low heat fluxes (fig. 4.6(a) and (c)). At 7.5 m, deviations of observed ϕ_m from the empirical curves arise

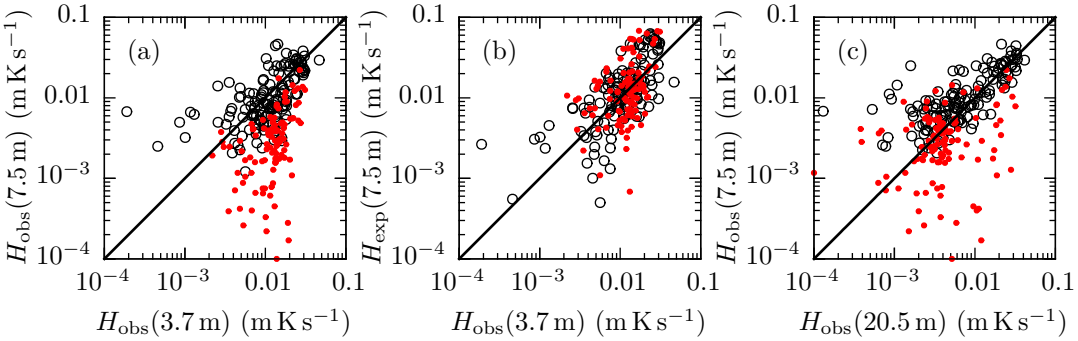

Figure 4.6: Comparison between observed heat fluxes at different sonic levels ((a), 7.5 m vs. 3.7 m, and (c), 7.5 m vs. 20.5 m) and between expected fluxes at 7.5 m and observed ones at 3.7 m (b) for the sector 300°-330° and for $z/\Lambda(7.5\,\mathrm{m}) \leq 0.04$ (red dots) and $z/\Lambda(7.5\,\mathrm{m}) > 0.04$ (open circles).

because the local stability parameter, z/Λ, does not represent anymore the stability of this points. Indeed, if a point lies near the empirical curve, an underestimation of z/Λ (i.e. of the heat flux) leads to an horizontal displacement of the point, in the ϕ_m-z/Λ plane, toward lower values of z/Λ and, then, an higher than expected ϕ_m. This mechanism can explain the observed behaviour also at 20.5 m although, in this case, points move far from curves for other sectors instead of empirical ones. Indeed, when surface scaling is adopted (fig. 4.3(d) and (e)), i.e. when Λ at 3.7 m is used as stability parameter instead of the local one, points from this sector do not extend anymore toward so small z/Λ and collapse closest to empirical curves (for $z = 7.5$ m) or to ϕ_m from other direction sectors (for $z = 20.5$ m).

In fig. 4.6(a) and (c) a comparison between heat fluxes, $H = -\overline{w'T'_s}$, measured at the three sonic levels for the sector 300°-330° is made for the whole dataset but retaining the stratification for z/Λ at 7.5 m yet adopted in fig. 4.5. In fig. 4.6(c) a comparison between heat fluxes expected at 7.5 m and those observed at 3.7 m is also shown. Expected fluxes, H_{exp} are those fluxes such that if substituted into empirical functions return the observed dimensionless gradients. That is:

$$\phi_m^{obs} = \phi_m^{emp}(z/\Lambda_{exp}) \quad \text{where} \quad \Lambda_{exp} = \Lambda_{obs}\frac{H_{obs}}{H_{exp}}.$$

The similarity relation from Businger et al. (1971) was used as empirical function, $\phi_m^{emp}(z/\Lambda) = 1 + 4.7(z/\Lambda)$, and the expected heat flux computed as

$$H_{exp} = \frac{\phi_m^{obs} - 1}{4.7 z/\Lambda_{obs}} H_{obs}.$$

When expected fluxes at 7.5 m are plotted against observed ones at 3.7 m (fig. 4.6(b)), most of the points related to anomalously small observed flux (red points) dispose around the 1:1 relation indicating that, for these runs, heat fluxes at 3.7 m are more representative of stability at 7.5 m than local ones.

It was speculated that this anomalously low heat fluxes at 7.5 and 20.5 m, which causes the failure of local similarity theory at these heights, were a manifestation of a two-layer structure. One surface layer which extends below 7.5 m and an outer layer above, thermally decoupled with the former. This seems further supported by the greater correlation between fluxes at 7.5 m and at 20.5 m (red points, fig. 4.6(d)) than with those at 3.7 m (red points, fig. 4.6(a)). This two-layer structure, however, involves only thermal characteristics of the

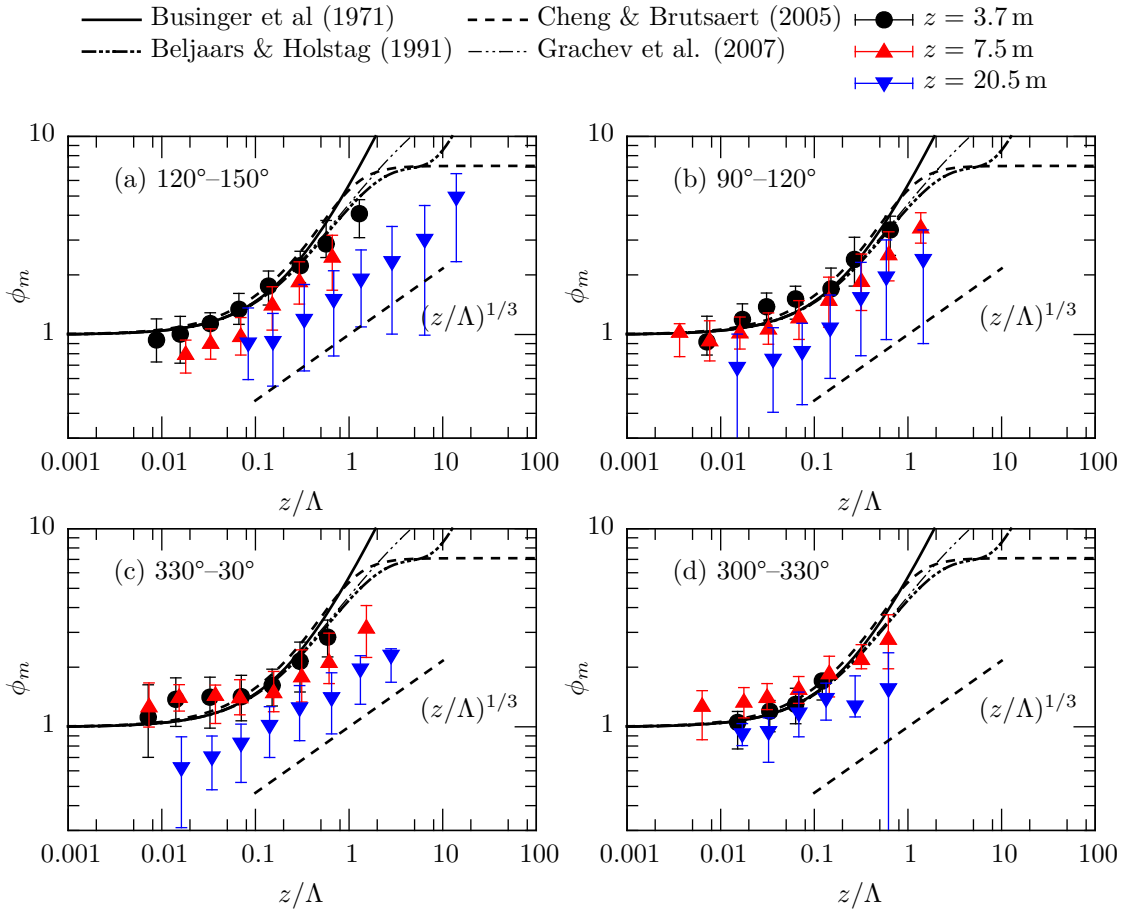

Figure 4.7: Similarity relationships for the CCT dataset (symbols), for the three sonic levels and for each direction sector, along with some empirical functions from other authors.

boundary layer and it is not found in dynamical ones: for this sector, vertical profiles of fluxes of momentum showed the maximum resemblance to those expected for a surface layer (fig. 4.5(d)) and no peculiar structures were observed in the wind profile (fig. 4.4).

Because for the sector 300°-330° sea-land transitions occur, at a distance of few kilometers from the CCT, it is possible that internal boundary layers form when on-shore flows are present. The advected boundary layer may adjusts dynamically with local properties but not thermally. A similar mechanism can explains observed near-neutral deviations between expected and observed ϕ_m for the sector 330°-30°, for which the sea-land transition is about 1 km far from the tower. In this case, however, also fluxes at 3.7 m are poorly representative of stability conditions, maybe because of the shorter land-fetch, that does not permit the achievement of thermal equilibrium to the advected layer. Also for the sector 90°-120° sea-land transitions can occur although dominant winds are from land (**??**). Some anomalously high values of ϕ_m were observed for this sector at the lowest sonic level in the interval $0.01 \lesssim z/\Lambda \lesssim 0.1$ (fig. 4.3(a)) but not at the higher level (fig. 4.3(b)).

As a final remark on deviations in near-neutral conditions, it was observed that higher than expected values of ϕ_m were associated mostly with strong winds, $\overline{S} > 9\,\mathrm{m\ s^{-1}}$. This however has not simple interpretations because near-neutral conditions occur mostly with strong winds and it is just in this range that greatest deviations occur.

Deviations between observed and expected ϕ_m at the middle sonic level for the two

south-eastern sectors can have also an instrumental origin. Indeed, the sonic speed at this level for these two sectors deviates significantly (about 30%) from the propeller's profile (fig. 4.4(a) and (b)) which is in better agreement, instead, with the sonic speed at 3.7 m. This deviations can be produced by the influence of the tower structure, as suggested by their directional dependence. Also the wind speed at the highest sonic level can differ significantly from propeller one (fig. 4.4(b) and (c)) suggesting that tower-perturbed flows can have a role in the strong deviations between observed and expected ϕ_m at this level.

4.5 Variation of ϕ_m with height above ground

Local similarity theory predicts that, when properly scaled, turbulence quantities should be (universal) functions of the stability parameter z/Λ only (Nieuwstadt, 1984; Sorbjan, 1986). For the wind shear this meas that when ϕ_m is plotted against z/Λ, data from different levels should collapse on the same curve. Some authors (Forrer and Rotach, 1997; Grachev et al., 2005, 2007a,b, 2013; Yagüe et al., 2006) found that this is indeed the case, at least for $z/\Lambda \lesssim 1$. Zilitinkevich and Esau (2007) proposed that, beyond Λ, the introduction of other length scales accounting for earth's rotation (i.e. $L_f = \tau^{1/2}/|f|$, f the Coriolis' parameter) and static stability (i.e. $L_N = \tau^{1/2}/N$, N the Brunt-Väisälä frequency) improves similarity. Salesky and Chamecki (2012) observed a diurnal cycle in the deviation between observed and expected ϕ_m that they attributed to a dependence of ϕ_m on the boundary layer height. Ha et al. (2007) observed influences of the speed of large-scale flow on flux-gradient relationships that are not captured by z/Λ suggesting that also wind speed should be accounted for.

Most of these studies refer to almost flat and uniform terrains, which is one of the hypothesis on which local similarity relies (the other is stationarity). In a complex and heterogeneous terrain (mountains, slopes, snow-free and snow-covered ground, sea-land transitions etc.) such as that where the CCT is, this hypothesis breaks down. Furthermore, the influence of surface heterogeneities changes as the height above ground changes and therefore also a dependence of ϕ_m on z, beyond z/Λ, is expected.

In fig. 4.7 a comparison between ϕ_m for the three sonic levels of the CCT ($z = 3.7$, 7.5 and 20.5 m), for each wind direction sector, is shown (as usual, data are reported as bin medians and 15th-85th percentile ranges). Also indicated are similarity functions from other experiments.

As a global answer: local similarity theory does not hold for the considered CCT dataset because values of ϕ_m from different levels do not collapse on the same curve. This does not happen, for the whole stability range, also for observations from the two lowest levels ($z = 3.7$ and 7.5 m) although they showed the closest values of ϕ_m. Deviations for the highest level ($z = 20.5$ m) are large, both in magnitude and in behaviour with z/Λ. However, it is suspected that some non-physical mechanism, such as instrumental errors or tower perturbations, is at least partially responsible for they.

Mechanisms that lead to the failure of local similarity theory, however, seem to change depending on wind direction sector (and then morphology and surface characteristics) and stability range (low stability, i.e. $z/\Lambda \lesssim 0.1$, against high stability, i.e. $z/\Lambda \gtrsim 0.1$).

For the near-neutral and weakly stable range (i.e. $z/\Lambda \lesssim 0.1$) and for sectors that contain sea-land transitions, deviations between levels (i.e. $z = 3.7$ m and $z = 7.5$ m) and between expected and observed ϕ_m are due to heat fluxes. In particular, anomalously low heat fluxes that make the Obukhov length, Λ, unrepresentative of local stability. This traduces in higher than expected values of ϕ_m in the near-neutral limit. This effect was

observed for the sector 330°-30° (fig. 4.7(c)) at both the lowest levels, for the sector 300°-330° (fig. 4.7(d)) at both the highest levels (although ϕ_m remains smaller than expected at 20.5 m) and, maybe, for the sector 90°-120° (fig. 4.7(b)) in the weakly stable range ($0.01 \lesssim z/\Lambda \lesssim 0.1$). At this regard is quite remarkable the agreement between anomalously high values of ϕ_m in the weakly stable range for the northern sector (fig. 4.7(c)). The origin of these anomalously small heat fluxes is unknown but it was supposed related to internal boundary layers formation in strong wind conditions and on-shore flows.

For the sector 120°-150° (fig. 4.7(a)), which does not contain sea-land transitions, the failure of local similarity in the near neutral range for $z = 7.5$ m is unknown. Although tower or instrumental effects cannot be ruled out (fig. 4.4(a)), topographic effects are also possible since mountain ranges are few kilometers far from the tower for this sector (fig. 2.1). Furthermore, as it will be shown in section 5.3, for $z = 7.5$ m, this sector is the most affected by self-correlation (table 5.3) and this explain why the observed behaviour of ϕ_m vs. z/Λ resembles that for $z = 20.5$ m.

For $z/\Lambda \gtrsim 0.1$ ϕ_m decreases systematically with z for all sectors. As yet done for the near-neutral range, profiles of normalized fluxes of heat and momentum were analyzed for the moderately stable range considering all runs for which $0.1 \leq z/\Lambda \leq 1$ at 3.7 m and all that satisfied the condition at 7.5 m.

The correlation between heat fluxes at 3.7 and 7.5 m is improved with respect to the near-neutral case (compare fig. 4.8(e)-(f) with fig. 4.5(e)-(f)) particularly for the northern and north-western sectors. This is in agreement with the fact that more stable conditions are generally characterized by larger better determined heat fluxes (Salesky and Chamecki, 2012). Although on average heat fluxes decrease with height for moderately stable conditions as expected (Nieuwstadt, 1984), fluxes at 20.5 m much larger than values at 3.7 m still remain when runs are selected with z/Λ at 3.7 m (filled circles).

Normalized fluxes of momentum show a larger scatter (fig. 4.8(a)-(d)) both at 7.5 and at 20.5 m. On average, signatures of an upside-down boundary layer are present for the sector 330°-30° (fig. 4.8(c)) independently on the selection criteria and, although less clearly, for the sectors 90°-120° and 300°-330° (fig. 4.8(b) and (d)). The sector 120°-150°, instead, show the expected profile for the stable boundary layer (Nieuwstadt, 1984). However, also Forrer and Rotach (1997) observed increasing fluxes of momentum with height for moderately stable conditions.

Heat fluxes indicate the existence of a surface layer extending at least up to 7.5 m (fig. 4.8(e)-(h)) for most of the moderately stable runs. This indication is much more weak looking at momentum fluxes (fig. 4.8(e)-(h)) showing instead that, for many runs, an almost-constant flux layer does not exist or extends below 7.5 m.

It was not observed a direct correlation between profiles of turbulent fluxes and deviations of observed ϕ_m to expected one. For example, no better agreement between expected and observed ϕ_m at 30.5 m for the sector 120°-150° (fig. 4.7), which showed the fluxes profiles most similar to expected ones in stable conditions.

The best agreement between observed and most used empirical similarity functions was observed for the lowest sonic level, $z = 3.7$ m, and among all, with that proposed by Beljaars and Holtslag (1991), although for the stability range of the CCT dataset at this level ($z/\Lambda \lesssim 1$) differences between formulations are quite small. Then, a decrease of ϕ_m with z was observed. For $z = 3.7\,m$, values of ϕ_m systematically lower than those at 3.7 m were observed mostly for $z/\Lambda \lesssim 1$ (fig. 4.7), with the exception of the sector 300°-330°.

The cause of this lower than expected ϕ_m at 7.5 m seems related to higher than expected fluxes of momentum (fig. 4.8(a)-(d)) and this is probably true, at leas partially, at 20.5 m

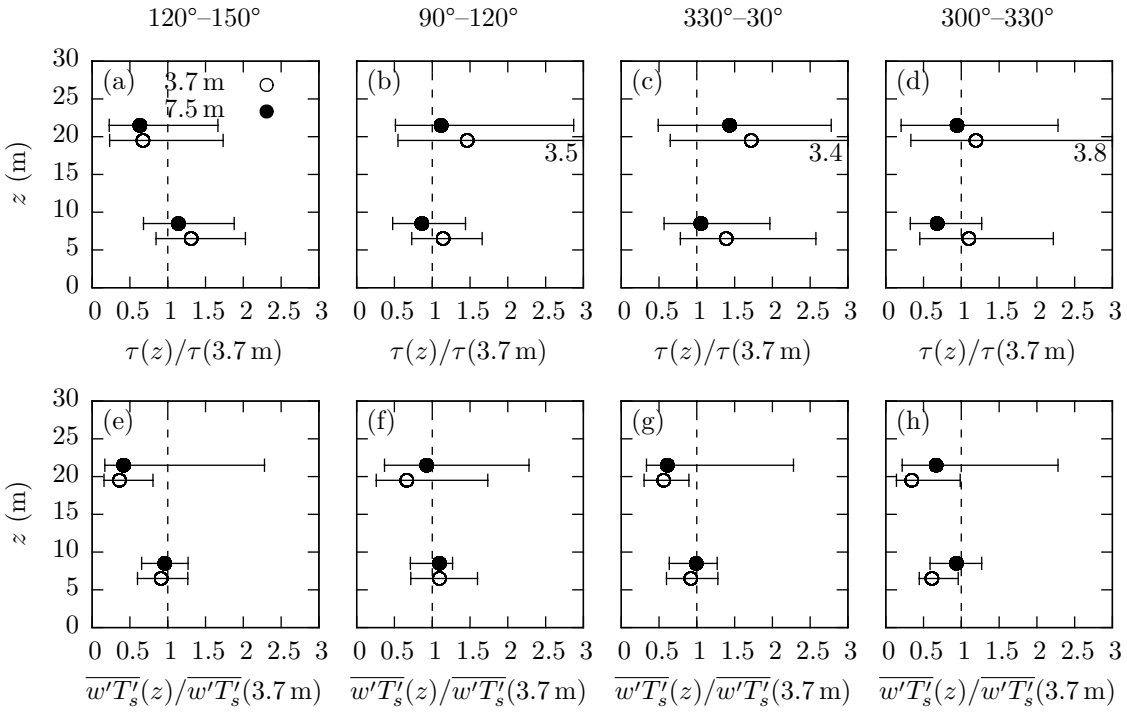

Figure 4.8: Fluxes of momentum and heat at 7.5 and 20.5 m, normalized by the value at 3.7 m, for all runs such that $0.1 \leq z/\Lambda \leq 1$ at 3.7 m (open circles) and at 7.5 m (filled circles): medians and 15th-85th percentile ranges are shown. In plots (b), (c) and (d) out-of-scale values are indicated.

where, the large variability of heat fluxes (fig. 4.8(e)-(h)) also contributes to the observed behaviour. However, if these high and variable fluxes are physics or instrumental effects or tower perturbations is unknown. The use of surface scaling does not improve similarity (fig. 4.3(d) and (e)) even if reduce self-correlation at the highest level.

Also Liang et al. (2014), from observations taken on the Loess Plateau (China), over complex terrain, obtained smaller values of ϕ_m than those predicted by universal similarity functions derived for almost flat surfaces (e.g. Beljaars and Holtslag, 1991; Businger et al., 1971; Cheng and Brutsaert, 2005a; Grachev et al., 2007b). Indeed, complex terrains enhance turbulence which reduces wind shear; whereas, over almost flat terrains turbulence is generated primarily by the wind shear. This means also that over complex terrain flux-gradient relationships can break-down. It is interesting to note that the sector showing lesser enhanced turbulence at 20.5 m is 120°-150° (fig. 4.5(a) and fig. 4.8(a)), for which Zeppelin mountain is present few kilometers far from the tower. Instead, maximum enhanced turbulence is showed by the sector 330°-30° (fig. 4.5(c) and fig. 4.8(c)) which has not so high obstacles. However it is possible that nearest terrain heterogeneities, although smaller, have more influence on the local turbulence field than farther mountains.

In fig. 4.9 the flux Richardson number against the local stability parameter for each direction sector and sonic level is shown along the expected behavior from empirical functions proposed by other authors. These plots are strictly related to those of fig. 4.7 since $\mathrm{R}_f = (z/\Lambda)\phi_m^{-1}$. Grachev et al. (2013) proposed that a critical value of the flux Richardson number $\mathrm{R}_{fc} \simeq 0.2$-$0.25$ can be used to discriminate between those cases for which local similarity theory holds ($\mathrm{R}_f \leq \mathrm{R}_{fc}$) and those for which does not ($\mathrm{R}_f > \mathrm{R}_{fc}$). They used also a threshold on the gradient Richardson number but that on R_f was more efficient to separate the two regimes.

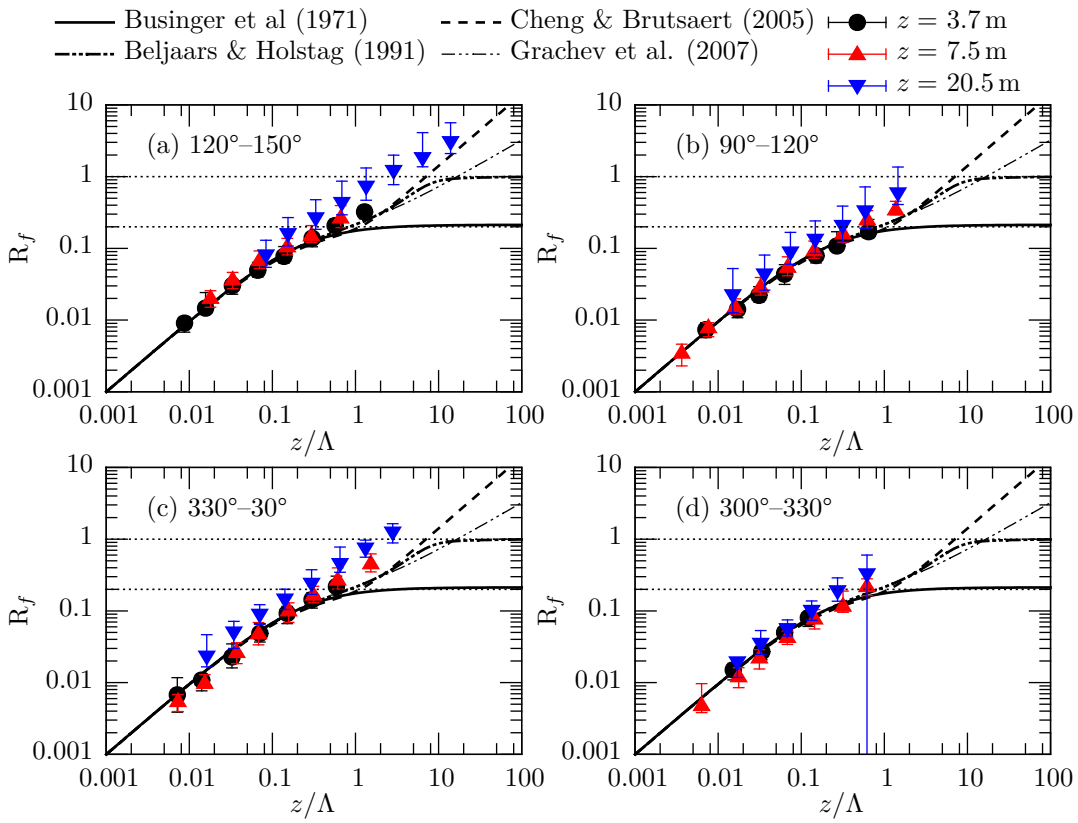

Figure 4.9: Flux Richardson number, R_f, against local stability parameter, z/Λ, for the CCT dataset (bin medians and 15th-85th percentile ranges) and from some empirical functions.

Some empirical formulations (Beljaars and Holtslag, 1991; Businger et al., 1971) predict the existence of a critical Richardson flux number but others do not (Cheng and Brutsaert, 2005a; Grachev et al., 2007b). For the existence of a critical R_f, ϕ_m must be proportional to z/Λ as the local stability parameter goes to infinity. Data from the CCT dataset do not indicate the existence of a critical value, at least of the order of 0.2 (fig. 4.9). Instead, for the highest sonic level, in particular for the sector 120°-150° (fig. 4.9(a)), were also observed values of R_f greater than 1, which is the theoretical limit for the stationary and horizontally homogeneous stable boundary layer. Assuming no instrumental artifacts, this indicates that conditions with decaying turbulence or transport mechanisms were present.

Chapter 5

Exploring self-correlation in ϕ_m vs. z/Λ plots

Self-correlation, also known as spurious or artificial correlation, is a mathematical artifact for which non-zero correlation is observed when two variables are compared, each of which obtained as a combination of uncorrelated random variables, that share a dependence on one (or more) of these random variables (Kim, 1999). For ϕ_m vs. z/Λ plots, self-correlation arises because of the shared variable u_* since $\phi_m \propto u_*^{-1}$ and $z/\Lambda \propto u_*^{-3}$ (Baas et al., 2006; Grachev et al., 2007a; Klipp and Mahrt, 2004; Liang et al., 2014). The height above ground, z, that enters in both the definition of the dimensionless wind shear and the stability parameter does not generate self-correlation because is usually taken constant and equal to the observation level's height.

Overestimation of the strength of the observed correlation can arise because of self-correlation when observed and self-correlation have the same sign (Baas et al., 2006; Klipp and Mahrt, 2004; Vickers et al., 2009). This is indeed the case for ϕ_m vs. z/Λ plots in stable conditions ($z/\Lambda \geq 0$), since the empirical relation derived from observation is usually a linear function, eg. $\phi_m = 1 + \beta_m(z/\Lambda)$ (e.g. Businger et al., 1971; Högström, 1988), or a more complicated monotonic non-decreasing function of z/Λ (e.g. Beljaars and Holtslag, 1991; Cheng and Brutsaert, 2005a; Grachev et al., 2007b), and that from self-correlation is $\phi_m \sim (z/\Lambda)^{1/3}$.

Baas et al. (2006) observed that the effect of self-correlation of ϕ_m vs. z/Λ plots increases as the ratio between relative errors in momentum fluxes ($\delta\tau/\tau$, with $\tau = u_*^2$) and those in heat fluxes ($\delta H/H$, with $H = \overline{w'T'}$) increases and as that stability increase. However, the strength of self-correlation does not depend directly on measurement errors but, instead, on the distributions of the variables (fluxes, wind shear etc.) in the considered dataset: i.e. the strength of self-correlation increases as the variation of the shared variable with respect those of non-shared variables increases (Kim, 1999).

In this chapter, the importance of self-correlation in the observed flux-gradient relationships from the CCT's dataset is estimated. As estimator was considered the Pearson's linear correlation coefficient. Pro and cons of this choice are discussed through the chapter. The widely observed linear behaviour $\phi_m = 1+\beta_m(z/\Lambda)$ at least for $z/\Lambda \lesssim 1$ (e.g. Businger et al., 1971; Grachev et al., 2007a; Högström, 1988, 1996; Yagüe et al., 2006; Zilitinkevich and Esau, 2007) was among the reasons that motivated this choice. In section 5.1, generalizing the results of Kim (1999) an expression for the linear coefficient of self-correlation between ϕ_m and z/Λ was derived and its results for the CCT's dataset discussed. In section 5.2, estimations of self-correlation from the generation of random datasets, both with random

permutations and sampling with replacement are presented. Finally, the significance of the observed correlation derived trough empirical distributions of the random linear correlation coefficient and from the fraction of explained variance is the subject of section 5.3.

5.1 The linear self-correlation coefficient between ϕ_m and z/Λ

When the plotted variables share a common term (as z and τ in ϕ_m vs. z/Λ plots) spurious correlation can arise due, in particular, to the shared variable with greatest coefficient of variation, i.e. $\sigma_X/\langle X\rangle$, where X is a stochastic variable and $\langle X\rangle$ and σ_X are its mean and standard deviation computed considering all points and that should not be confused with time averages (Kim, 1999). Kim (1999) derived an expression for the linear-correlation coefficient due to spurious correlation for between two variables that share a common divisor or a common factor. The height above ground, z is a common factor between ϕ_m and z/λ. The local friction.

Considering four stochastic independent variables, X, Y, A and B except that a correlation exists between A and B (both linear or not). The coefficient of linear correlation between the products AX and BY is

$$r_{(AX)(BY)} = \frac{\operatorname{cov}(AX, BY)}{\sqrt{\operatorname{var}(AX)\operatorname{var}(BY)}}$$

where $\operatorname{var}(X) = \langle X - \langle X\rangle\rangle^2$ is the variance of X and $\operatorname{cov}(X,Y) = \langle (X - \langle X\rangle)(Y - \langle Y\rangle)\rangle$ the covariance of X, Y and $\langle\cdot\rangle$ indicates the expectation value. From the independence we have

$$r_{(AX)(BY)} = \frac{\operatorname{cov}(A,B)\operatorname{sgn}(\langle X\rangle)\operatorname{sgn}(\langle Y\rangle)}{|\langle A\rangle||\langle B\rangle|\sqrt{[V_X^2(1+V_A^2)+V_A^2][V_Y^2(1+V_B^2)+V_B^2]}} \tag{5.1}$$

where $\operatorname{sgn}(x) = x/|x|$ is the "sign" function and were introduced the coefficients of variation, e.g. $V_Y = \sqrt{\operatorname{var}(Y)}/|\langle Y\rangle|$. Supposing that both the expectation values $\langle X\rangle$ and $\langle Y\rangle$ are positive or, more generally, that have the same sign and introducing the linear correlation coefficient

$$r_{AB} = \frac{\operatorname{cov}(A,B)}{\sqrt{\operatorname{var}(A)\operatorname{var}(B)}}$$

we have

$$r_{(AX)(BY)} = \frac{r_{AB}V_AV_B}{\sqrt{[V_X^2(1+V_A^2)+V_A^2][V_Y^2(1+V_B^2)+V_B^2]}} \tag{5.2}$$

which is the coefficient of linear correlation between the variables AX and AY due only to the correlation between A and B and their statistical variations V_A and V_B. When $A = B$, $r_{AB} = 1$, $V_A = V_B$ and eq. (2.2) of Kim (1999) is obtained:

$$r_{(AX)(AY)} = \frac{V_A^2}{\sqrt{[V_X^2(1+V_A^2)+V_A^2][V_Y^2(1+V_A^2)+V_A^2]}}. \tag{5.3}$$

The relationship between A and B affects not only the linear correlation index r_{AB} but also the relative magnitude of the coefficients of variation V_A and V_B.

Table 5.1: Linear self-correlation between ϕ_m and z/Λ due to u_* for each wind direction sector at $z = 3.7\,\mathrm{m}$: N is the number of data points, $\phi_m \equiv AX$, $z/\Lambda \equiv BY$, $A = u_*^{-1}$, $B = u_*^{-3}$, $X = \kappa z(d\overline{S}/dz)$, $Y = -g\kappa z\overline{w'T_s'}/\overline{T}_s$, V_{u_*} and V_H are the coefficients of variation for the friction velocity and the heat flux.

(a) $z = 3.7\,\mathrm{m}$

Sector	N	$r_{(AX)(BY)}$	r_{AB}	V_A	V_B	V_X	V_Y	V_H	V_{u_*}
120°–150°	656	0.61	0.80	0.47	2.3	0.22	0.56	0.57	0.41
90°–120°	717	0.54	0.77	0.57	3.7	0.32	0.62	0.62	0.40
30°–330°	530	0.58	0.87	0.45	1.8	0.33	0.53	0.53	0.38
300°–330°	256	0.61	0.82	0.45	3.5	0.24	0.56	0.55	0.33

(b) $z = 7.5\,\mathrm{m}$

Sector	N	$r_{(AX)(BY)}$	r_{AB}	V_A	V_B	V_X	V_Y	V_H	V_{u_*}
120°–150°	656	0.63	0.87	0.44	1.7	0.23	0.58	0.58	0.40
90°–120°	717	0.48	0.69	0.50	3.3	0.29	0.66	0.66	0.40
30°–330°	530	0.59	0.86	0.45	2.1	0.30	0.56	0.56	0.36
300°–330°	256	0.50	0.83	0.57	6.3	0.27	1.0	1.0	0.34

(c) $z = 20.5\,\mathrm{m}$

Sector	N	$r_{(AX)(BY)}$	r_{AB}	V_A	V_B	V_X	V_Y	V_H	V_{u_*}
120°–150°	656	0.39	0.78	0.61	3.0	0.49	1.0	1.0	0.55
90°–120°	717	0.31	0.70	0.65	5.5	0.49	1.3	1.3	0.43
30°–330°	530	0.52	0.75	0.61	5.1	0.36	0.64	0.64	0.43
300°–330°	256	0.45	0.80	0.71	7.4	0.41	1.0	1.0	0.37

The shared variables between ϕ_m and z/Λ are the height above ground, z, (i.e. $\phi_m \propto z$ and $z/\Lambda \propto z$) and the local friction velocity, u_* (i.e. $\phi_m \propto u_*^{-1}$ and $z/\Lambda \propto u_*^{-3}$).[1]

At each sonic level the height above ground was taken constant and equal to its nominal value, i.e. $V_z = 0$. Thus, no spurious correlation arises from the shared variable z.

The contribution from self-correlation to the observed linear correlation between ϕ_m and z/Λ due to u_* can be estimated from (5.1) or (5.2) taking $\phi_m \equiv AX$, with $A = u_*^{-1}$, $X = \kappa z(d\overline{S}/dz)$ and $z/\Lambda \equiv BY$, with $B = u_*^{-3}$ and $Y = -g\kappa z\overline{w'T_s'}/\overline{T}_s$. Furthermore, we can take $V_X = V_{d\overline{S}/dz}$ and $V_Y = V_{H/\overline{T}_s}$, where $H = -\overline{w'T_s'}$, because variables differing only by a constant factor have the same coefficient of variation. The passage from (5.1) to (5.2) is allowed since $\langle X\rangle > 0$ ($\langle d\overline{S}/dz\rangle > 0$) and $\langle Y\rangle > 0$ ($-\overline{w'T_s'} > 0$), in stable conditions (in unstable conditions, $\langle Y\rangle < 0$ and a minus sign appears in front of (5.2)).

Statistics for the wind shear, $d\overline{S}/dz$, the normalized heat flux $H/\overline{T}_s$ and the two u_*-functions $A = u_*^{-1}$ and $B = u_*^{-3}$ were computed for all data points. Expectation values, variances and covariances were substituted with their sample estimations: e.g.,

$$\langle A\rangle_N = \frac{1}{N}\sum_{i=1}^{N} A_i, \quad \mathrm{var}(A)_N = \frac{\sum_{i=1}^{N}(A_i - \langle A\rangle_N)^2}{N-1}$$

[1]Here, u_* is used instead of $\tau^{1/2}$ for the local friction velocity to avoid cumbersome notation, however this does not mean that the surface value instead of the local one is used.

and

$$\mathrm{cov}(A,B)_N = \frac{\sum_{i=1}^{N}(A_i - \langle A\rangle_N)(B_i - \langle B\rangle_N)}{N-1},$$

where N is the number of data points. Then, the coefficient of spurious correlation was derived from (5.1).

Results are reported in table 5.1 for all the three sonic levels and the four wind direction sectors. Besides the spurious correlation statistics, the coefficient of variation for the heat flux V_H and the local friction velocity V_{u_*} are also showed. At each level and direction sector $V_Y \approx V_H$ indicating that the temperature relative variation is negligible with respect that of the heat flux.

High spurious correlation arises when r_{AB} is high, $V_A \gg V_X$ and $V_B \gg V_Y$ (see eq. (5.2)). For the considered dataset, the coefficient of variation for $u_*^{-1/3}$, V_B, was between 3 and 7 times greater than that for the heat flux, V_Y, and the greatest among all variables. Instead, even if $V_A > V_X$ in all cases, the observed relative differences are much smaller that those between V_B and V_Y, with the variation of u_*^{-1} which is at most twice that of the wind shear.

The two variables $A = u_*^{-1}$ and $B = u_*^{-3}$ are exactly correlated, although non-linearly. The observed variations of r_{AB} between levels, for the same sector (same number of points), are due to differences in the distribution of u_* (and then of u_*^{-1} and u_*^{-3}), probably in their width. This was suggested by the smaller values of r_{AB} observed for the highest sonic level (table 5.1(c)) with respect to the lower ones (table 5.1(a)-(b)), which are accompanied with an higher variability of the friction velocity, V_{u_*}. Anyway, further investigations are needed about the effects of the u_*-distribution on r_{AB}. The between-sector variations of r_{AB}, at the same level, can be explained also by the sensitivity of the coefficient on the number of data points.

The coefficient of spurious correlation $r_{(AX)(BY)}$ is high for all levels and wind direction sectors, indicating that a significant amount of the observed correlation between ϕ_m and z/Λ can be explained by the shearing of u_*. Furthermore, it is interesting to note that the smallest spurious correlation is observed at the highest sonic level (table 5.1(c)), the same level that showed the most evident effects of self-correlation in ϕ_m vs. z/Λ plots. This is due by two reasons.

Firstly, self-correlation is only partially traduced into linear correlation since the non-linear behaviour $\phi_m \propto (z/\Lambda)^{1/3}$, the traduced part being expressed by r_{AB}, which is smaller at the highest level probably because of a greater variability in u_*.

Secondly, beyond variations in r_{AB}, spurious correlation becomes stronger as V_X and V_Y becomes smaller and V_A and V_B becomes bigger: i.e. as the variation of the friction velocity increases and those of wind shear and heat flux decrease. Indeed, from (5.2) we have

$$r_{(AX)(BY)} = \frac{r_{AB}}{\sqrt{[V_X^2 + (V_X/V_A)^2 + 1][V_Y^2 + (V_Y/V_B)^2 + 1]}}.$$

At the highest sonic level (table 5.1(c)) an increase of all coefficients of variation was observed with respect to those at the lower ones (table 5.1(a)-(b)). However, the relative increase of those for wind shear and heat flux, V_X and V_Y, is greater than those for friction velocity, V_A and V_B. The increase of V_X, V_Y and of the ratios V_X/V_A and V_Y/V_B leads to a decrease of $r_{(AX)(BY)}/r_{AB}$ from the lowest levels to the highest one. An exception is represented by the sector 30°–330° which indeed shows similar values of $r_{(AX)(BY)}/r_{AB}$ between the three levels.

5.2 Self-correlation estimation by random datasets generation

To establish the degree of linear correlation between two variables, say x and y, the coefficient r is computed and its value compared with the distribution of r for two completely uncorrelated variables. In particular, the probability for two uncorrelated variables to obtain an $|r|$ greater than that observed, $|r_{\text{obs}}|$, is considered. The smaller this probability, the stronger the correlation is. Usually, if this probability is lesser than 5% the correlation is considered *significant*, if lesser than 1%, *very significant* (Taylor, 2000). Whereas, if values greater than 5% or 10% are obtained, the null hypothesis that the two variables are not correlated and the observed value of r is due only to chance cannot be safely rejected.

The question now is: How can be computed the probability to obtain $|r| \geq |r_{\text{obs}}|$ due to chance, i.e. the level of significance of the observed correlation? Or, equivalently: Which is the probability distribution function of r in the null hypothesis, i.e. that x and y are perfectly uncorrelated variables? From Press et al. (1997), sec. 14.5, p. 630, changing slightly the notation:

> [...] About the only general statement that can be made is this: If the null hypothesis is that x and y are uncorrelated, and if the distributions for x and y each have enough convergent moments ("tails" die off sufficiently rapidly), and if N is large (typically > 500), then r is distributed approximately normally, with a mean of zero and a standard deviation of $1/\sqrt{N}$. In that case, the (double-sided) significance of the correlation, that is, the probability that $|r_{xy}|$ should be larger than its observed value in the null hypothesis, is
>
> $$P(|r| \geq |r_{\text{obs}}|) = \operatorname{erfc}\left(\frac{|r_{\text{obs}}|\sqrt{N}}{\sqrt{2}}\right)$$
>
> [...]

where N is the number of data points and

$$\operatorname{erfc}(x) = \frac{2}{\sqrt{\pi}} \int_x^\infty e^{-t^2} dt$$

is the complementary error-function.

However we are dealing with two variables, ϕ_m and z/Λ, that cannot be never perfectly uncorrelated, because of the shared variable u_*. Thus, the null hypothesis changes and the question become: Which is the probability distribution of the linear correlation coefficient, r, between two variables, x and y, each obtained as a combination of perfectly uncorrelated variables, when one of these variables enter into the definition of both x and y? Answer this question leads to the probability density function (pdf) for r, in the null hypothesis, when self correlation is present. The significance of the observed correlation is then estimated comparing r_{obs} with this pdf: i.e. the pdf of the self-correlation coefficient, i.e. the linear correlation coefficient between x and y when only self-correlation are acting.

Of this distribution we know only that the expected value of r is $\langle r \rangle = r_{(AX)(BY)}$ from eq. (5.2) and that becomes the new level of zero-correlation, instead of $r = 0$ (Kim, 1999).

At this point a clarification is needed. Spurious correlation does not mean that the observed correlation between ϕ_m and z/Λ does not exist but, instead, that it is only a mathematical artifact. In other words, an observed correlation coefficient too near to the spurious correlation value, $r_{(AX)(BY)}$, could mean that no useful physics can be inferred

n	Original dataset			
1	$d\overline{S}/dz_1$	u_{*1}	$\overline{w'T'_{s1}}$	$\overline{T}_{s1}$
2	$d\overline{S}/dz_2$	u_{*2}	$\overline{w'T'_{s2}}$	$\overline{T}_{s2}$
⋮	⋮	⋮	⋮	⋮
N	$d\overline{S}/dz_N$	u_{*N}	$\overline{w'T'_{sN}}$	$\overline{T}_{sN}$

n	Random dataset			
1	$d\overline{S}/dz_{37}$	u_{*2}	$\overline{w'T'_{s24}}$	$\overline{T}_{s15}$
2	$d\overline{S}/dz_{98}$	u_{*32}	$\overline{w'T'_{s7}}$	$\overline{T}_{s6}$
⋮	⋮	⋮	⋮	⋮
N	$d\overline{S}/dz_5$	u_{*12}	$\overline{w'T'_{s44}}$	$\overline{T}_{s18}$

Figure 5.1: An example of random dataset generation.

from data. Another possibility, however, is that the compared variables are truly related but via a strongly non-linear law: this could lead to an observed correlation coefficient even below the level of spurious correlation.

Beyond $\langle r \rangle$, which can only be estimated via (5.2) because statistics in (5.2) are substituted with their sample estimation, we do not know further about the pdf of the self correlation coefficient. We can suppose that it should be centered around this value. However we even do not know if it is symmetric. Indeed, despite the large number of points ($N > 500$) in the considered datasets (with the exception of the 300°–330° sector) no much can be said about the condition that « "tails" die off sufficiently rapidly» (Press et al., 1997) for the distributions of ϕ_m and z/Λ.

A way for estimating the pdf of r in the null hypothesis is the generation of many datasets containing random data, to compute random ϕ_m's and z/Λ's from random fluxes and random wind shears, to derive r for each random dataset and observe how it distributes.

Attention must be paid that the distributions of random variables in the random dataset are the same of observed variables in the original dataset because the coefficient of self-correlation depend on how variables are distributed (section 5.1; Kim, 1999; Klipp and Mahrt, 2004;Vickers et al., 2009).

Random datasets preserving the distributions of the original one can be obtained through random permutations of the elements in the original dataset (Baas et al., 2006; Vickers et al., 2009). Uniformly distributed random integers between 1 and N, where N is the length of the dataset, are created with a random number generator. Random permutations of the original dataset are performed with Knuth shuffle algorithm in this way:

1. the n-th element in the dataset is considered: $x(n)$, for $1 \leq n \leq N$;

2. a random integer is generated: I, with $1 \leq I \leq N$;

3. a permutation between $x(n)$ and $x(I)$ is carried out.

This three steps are repeated for all the elements of the dataset, i.e., for $1 \leq n \leq N$. Random permutations were carried out separately on the wind shear array $d\overline{S}/dz(N)$, the friction velocity array, $u_*(N)$, the heat flux array $\overline{w'T'_s}(N)$ and the temperature array $\overline{T}_s(N)$. Random permutations were carried out also on temperature even if the self correlation index has shown to be almost insensitive to this variables (section 5.1) for the shake of generality and because no much more computational effort was needed. In fig. 5.1 an example of random dataset generation is shown. 1000 random datasets were created for each sonic level and wind direction sector and the linear correlation coefficient computed between the random ϕ_m's and z/Λ's for each dataset.

Klipp and Mahrt (2004) generated their random datasets with a different method: i.e. random sampling with replacement. That is, random integers are used as indexes to draw an element from the original dataset:

1. a random integer is generated: I, with $1 \leq I \leq N$;

2. the element of the random dataset is drawn from the pool of observed values: $x_{\text{rand}}(n) = x_{\text{orig}}(I)$, for $1 \leq n \leq N$;

the process is repeated until all N random elements were attributed. And this is done for all the variables separately. Vickers et al. (2009) define their method as random permutations although from their description it resembles more sampling with replacement.

Whereas datasets generated with random permutations have exactly the same variables distributions that the original ones (elements are the same, only in a different order), in general, those generated via sampling with replacement have not. Indeed, in sampling with replacement, one element of the original dataset can be drawn one or more times, or even can not be drawn at all.

The probability to generate a sequence of length N which does not contain repeated indexes is $P = N!/N^N$ which can be approximated as $P \approx \sqrt{2\pi N}e^{-N}$ just for $N \gtrsim 10$, using Stirling's formula, $N! \sim \sqrt{2\pi N}N^N e^{-N}$ as $N \to \infty$. For $N \sim 100$, as it is (at least) for the considered datasets, $P \sim 10^{-43}$. Then, we expect that almost all randomly generated sequences contain repeated indexes and, then, all random datasets differ (because of the contained elements) from the original one.

As a comparison test, 1000 random datasets for each sonic level and wind direction sector were generated by mean of the sampling with replacement method. In table 5.2 are reported, for each sonic level and wind direction secor, the number of data points, N, the observed linear correlation coefficient between ϕ_m and z/Λ for the original dataset, r_{obs}, the self-correlation coefficient from eq. (5.2), $r_{(AX)(BY)}$, the self correlation coefficients estimated from randomized datasets by random permutations, r_{perm}, and sampling with replacement, r_{swr}. For random permutations and sampling with replacement, the coefficient of self-correlation was estimated as the average of r among all the 1000 random datasets, the uncertainty of this estimation computed as the uncertainty of the average (Taylor, 2000), $\sqrt{\text{var}(r)_M/M}$ where $\text{var}(r)_M$ is the sample-variance between datasets and $M = 1000$.

For all levels and wind direction sectors, the coefficient of self-correlation is a substantial fraction of the observed value: between 60% and 90%, depending on level and sector table 5.2. For the highest sonic level (table 5.2(c)), observed correlations lower than spurious ones were obtained (sectors 90°–120° and 300°–330°). The near zero coefficient obtained for the 300°–330°-sector, well below the self-correlation level, indicates that the observed independence of the dimensionless gradients on the stability parameter (**??**(d)) is not generated by self-correlation but by some mechanism, maybe of physical nature.

The self-correlation coefficients estimated by sampling with replacement are systematically higher than those estimated with random permutations (with the exception of $z = 20.5\,\text{m}$, table 5.2(c), 300°–330°-sector) although differences are sometimes of the order of statistical uncertainties. These deviations reflect changes in the distributions of variables, because random permutations conserve the original ones and sampling with replacement does not.

Self-correlation estimates from randomized datasets, both with random permutations or sampling with replacement, are always higher than those obtained from (5.2). Two reasons can explain these differences.

Table 5.2: Comparison between observed linear correlation coefficient and self-correlation coefficients estimated with different methods for the three sonic levels and each wind direction sector.

(a) $z = 3.7\,\mathrm{m}$

Sector	N	r_{obs}	$r_{(AX)(BY)}$	r_{perm}	r_{swr}
120°–150°	656	0.85	0.61	0.640 ± 0.002	0.645 ± 0.002
90°–120°	717	0.58	0.54	0.581 ± 0.003	0.587 ± 0.002
30°–330°	530	0.72	0.58	0.592 ± 0.002	0.593 ± 0.002
300°–330°	256	0.64	0.62	0.657 ± 0.002	0.661 ± 0.003

(b) $z = 7.5\,\mathrm{m}$

Sector	N	r_{obs}	$r_{(AX)(BY)}$	r_{perm}	r_{swr}
120°–150°	656	0.70	0.63	0.634 ± 0.001	0.639 ± 0.001
90°–120°	717	0.67	0.48	0.557 ± 0.003	0.569 ± 0.003
30°–330°	530	0.68	0.59	0.604 ± 0.002	0.604 ± 0.002
300°–330°	256	0.80	0.50	0.647 ± 0.004	0.624 ± 0.004

(c) $z = 20.5\,\mathrm{m}$

Sector	N	r_{obs}	$r_{(AX)(BY)}$	r_{perm}	r_{swr}
120°–150°	656	0.60	0.40	0.439 ± 0.003	0.438 ± 0.003
90°–120°	717	0.28	0.31	0.445 ± 0.003	0.459 ± 0.003
30°–330°	530	0.53	0.52	0.568 ± 0.003	0.575 ± 0.003
300°–330°	256	0.05	0.45	0.602 ± 0.005	0.579 ± 0.005

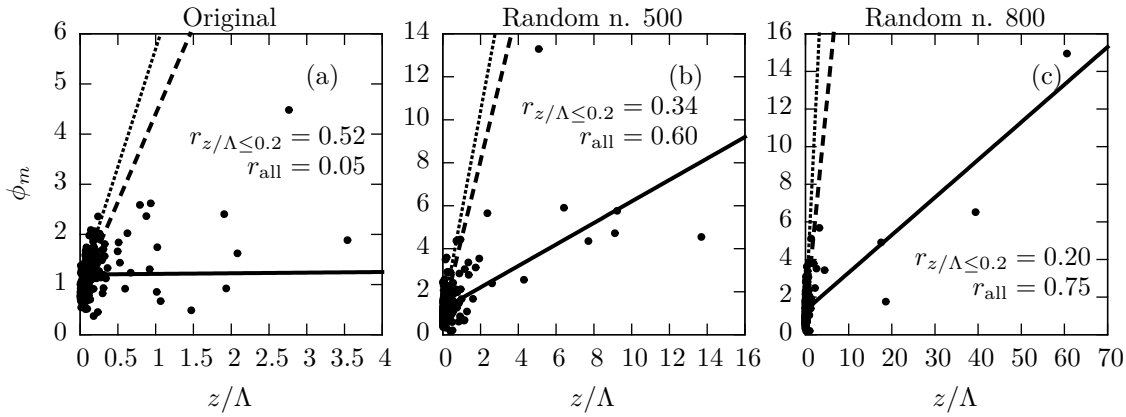

Figure 5.2: Dimensionless gradient, ϕ_m, against stability parameter, z/Λ, for the original dataset (a) and two randomized datasets, (b) and (c), for $z = 20.5$ m and 300°-330°-sector. Linear fits for all data (solid lines) and $z/\Lambda \leq 0.2$ data only (dashed lines) are shown along with their respective linear correlation coefficients. The similarity relationship from Businger et al. (1971) (dotted line) is also shown for comparison.

The first one is that, in general, randomized datasets are not composed by truly random data points and a fraction of true correlation present in the original dataset can be retained also in the randomized ones. However, the importance of this contribution is questioned by the observed behaviour at the highest sonic level (table 5.2(c)) and, particularly, for 300°–330°-sector. Indeed, because of the near-zero observed correlation in the original dataset, if some of this non-correlation is retained in the random ones, then random correlations lower than $r_{(AX)(BY)}$ are expected. Instead, the greatest positive deviations between r_{perm} and $r_{(AX)(BY)}$ were observed just for this case.

The second reason is the sensitivity of the linear correlation coefficient to outliers. Indeed, few data points with anomalously high values of z/Λ can strongly influence the degree of linear correlation of the whole dataset. This is evident from the plots reported in fig. 5.2 which refer again to the highest sonic level and the 300°–330°-sector. Linear fits between ϕ_m and z/Λ were derived for the original and for two randomized datasets (with random permutations) considering only points with $z/\Lambda \leq 0.2$ and all points, separately. Solid lines in fig. 5.2 refer to all points, dashed ones to low z/Λ points only. The similarity relationship from Businger et al. (1971) is also shown for comparison.

When the whole dataset is considered, the derived linear relation fits better the outliers than low-z/Λ points which are much more numerous. The fact that outliers are usually characterized by anomalously high values of z/Λ but by no so high values of ϕ_m, as observed also by Klipp and Mahrt (2004), determine the deviations between low-z/Λ-fits and whole-range-fits. This sensitivity to outliers is reflected, in turn, on the linear correlation coefficient. Indeed, depending on the positions of these outliers, the correlation for the whole dataset cam be improved, as for random datasets in fig. 5.2(b) and (c), or reduced, as for the original dataset in fig. 5.2(a).

In stable conditions, real datasets are typically composed of many data points with $z/\Lambda < 1$ and few scattered points with $z/\Lambda \gg 1$. Thus, the presence of few large-z/Λ points affects not only the correlation coefficient of randomized datasets but also that of observed ones. However this does not mean that the effect of outliers cancel when the observed correlation is compared with correlation of random datasets, as shown in fig. 5.2. Furthermore, Klipp and Mahrt (2004) observed an increase in random correlation when

only low-z/Λ points are considered, which is the opposite of that showed in fig. 5.2(b) and (c). However, they chose higher z/Λ-thresholds, and some sensitivity of correlation to this thresholds, which cannot be explained by variations in the number of data points, was indeed observed. Outliers can then act in a non-easily predictable manner on both observed and random correlations. This further suggests that caution must be payed in the interpretation of the random correlation coefficient as a self-correlation level (Klipp and Mahrt, 2004).

One way to reduce the influence of outliers is to discard them during the generation of the random dataset fixing some threshold for z/Λ. However, this arises further questions about the randomness of the generated dataset. Another way is to consider estimators that are less sensitive to outliers, such as rank correlation coefficients. The Spearman rank correlation coefficient was also considered as a self-correlation estimator, as will be discussed later, although this method has its own drawbacks too.

As a final remark, it is interesting to note that $\phi_m(z/\Lambda = 0) \simeq 1$ also for randomized datasets as indicated by linear fits of fig. 5.2(b)-(c). This closer than expected agreement of random points with the theoretical relationship for small z/Λ was also observed by Klipp and Mahrt (2004). The limited range of the dataset could be responsible of this behaviour, since $\phi_m = \mathrm{O}(1)$ also for most random points.

5.3 Significance level of observed correlation

The strength of the observed correlation cannot be safely estimated comparing the observed linear correlation coefficient with the self-correlation level from eq. (5.2) or from random datasets only. Indeed, the probability that observed deviations are due by chance must be estimated: i.e. the significance level of the observed correlation must be estimated. As discussed in section 5.2, the significance of the observed correlation can be obtained comparing the observed r with the pdf of the self-correlation coefficient.

The pdf of the self-correlation coefficient was estimated from the distribution of r for the 1000 randomized datasets, with all the limitations yet discussed (e.g. outliers sensitivity and residual correlation). A pdf for each level and direction sector (each original dataset) was derived. Randomized datasets from random permutations were considered because, with this method, values of r closer to those from eq. (5.2) were obtained (table 5.2).

In particular, the null hypothesis that the random correlation coefficient was normally distributed was tested. However, instead of r, the normalized test-statistic

$$R = \frac{r - \langle r \rangle_M}{\sqrt{\mathrm{var}(r)_M}}$$

was considered, where r is the linear correlation coefficient of randomized datasets, $\langle r \rangle_M$ the mean value between all $M = 1000$ random datasets (r_{perm}, in table 5.2) and $\mathrm{var}(r)_M$ its sample-variance.

In the null hypothesis R is a normal random variable (zero mean and unitary variance) with pdf

$$p(R) = \frac{e^{-R^2/2}}{\sqrt{2\pi}} \tag{5.4}$$

and cumulative distribution function (cdf)

$$P(R) = \int_{-\infty}^{R} p(x)dx, \quad \text{i.e.} \quad P(R) = 1 - \frac{1}{2}\mathrm{erfc}\left(\frac{R}{\sqrt{2}}\right). \tag{5.5}$$

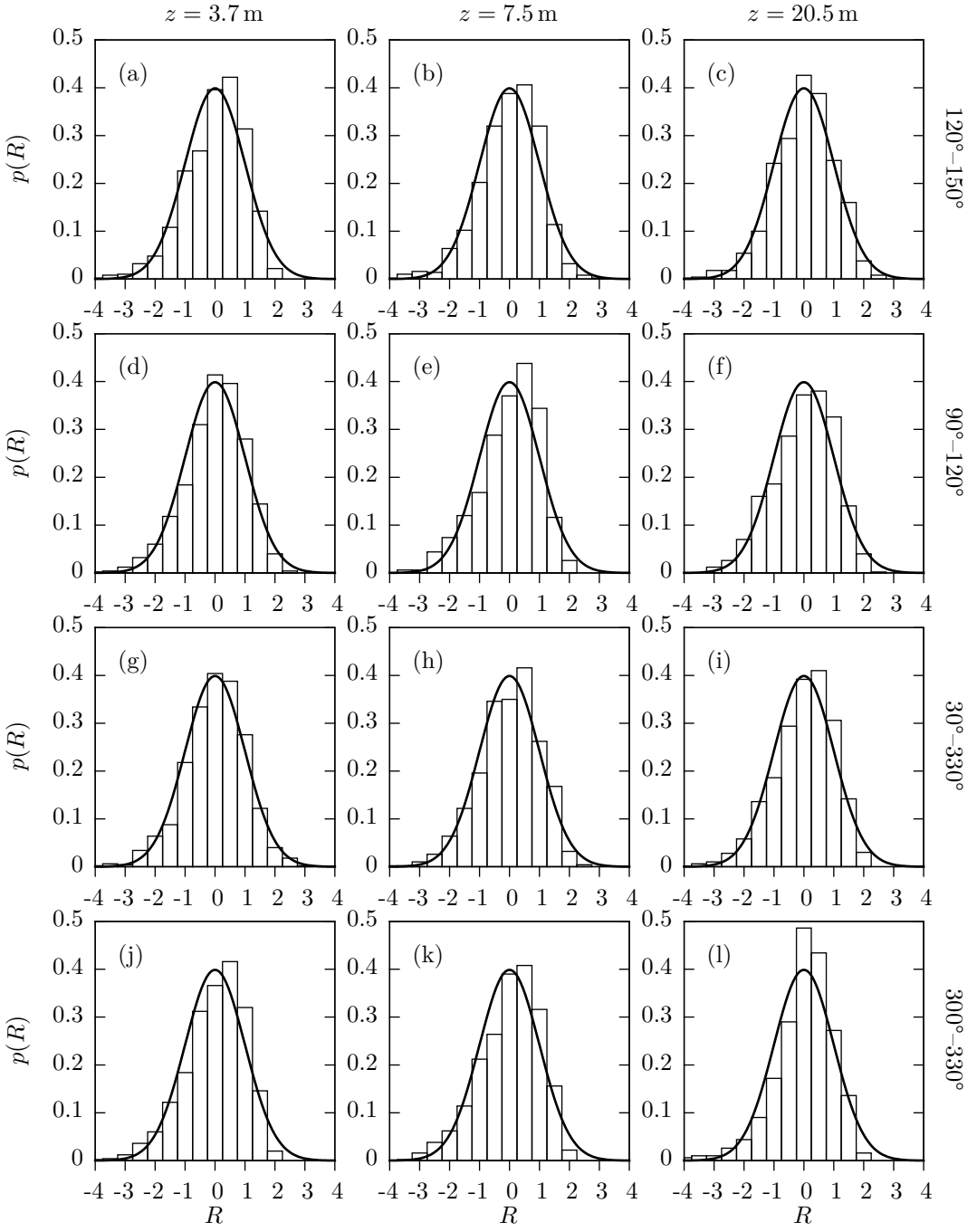

Figure 5.3: Observed probability distribution functions of $R = (r - \langle r \rangle_M)/\sqrt{\mathrm{var}(r)_M}$ for each sonic level (columns) and wind direction sector (rows). The pdf of R in the null hypothesis, $p(R) = e^{(-R^2/2)}/\sqrt{2\pi}$, is represented by the solid line.

The expected distribution of R in the null hypothesis was compared to the observed one for each sonic level and wind direction sector through a chi-square test (Press et al., 1997). Observed values of R were subdivided in 10 intervals: $R \leq 2$, 8 intervals of width $\delta R = 0.5$ for $-2 < R < 2$ and $R \geq 2$. This choice was motivated by the requirement that both the expected number of events and the observed one falling in each interval were $\gg 1$ (Press et al., 1997; Taylor, 2000) although, in some cases, the number of observed events in the two side intervals was only > 1. The reduced chi-square was then computed summing the squared deviations between the observed and the expected number of events over all $m = 8$ intervals:

$$\tilde{\chi}^2 = \frac{1}{d} \sum_{i=1}^{m} \frac{(n_i^{\text{obs}} - n_i^{\text{exp}})^2}{n_i^{\text{exp}}}$$

where $d = m - k$ are the degrees of freedom and k the number of constraints. Because both the mean and the variance of the expected distribution were derived from observations, we have $d = 10 - 3 = 7$ degrees of freedom. The expected number of events in the i-th interval was obtained from the cdf (5.5):

$$n_i^{\text{exp}} = M(P(R_i^{\text{sup}}) - P(R_i^{\text{inf}}))$$

where R_i^{inf} and R_i^{sup} are the extremes of the interval. The probability of obtaining, in the null hypothesis (i.e. that the observed and the expected distributions are the same), a value of $\tilde{\chi}^2$ as extreme as that observed only by chance is then derived (Press et al., 1997). For all levels and direction sectors, the null hypothesis was rejected with a significance level $\ll 0.01$ concluding than that the observed distributions of the random correlation coefficient cannot be accurately approximated by a normal distribution with mean $\langle r \rangle_M$ and variance $\text{var}(r)_M$.

In fig. 5.3, observed and expected distributions for R for each level and wind direction sector are shown. In general, observed distributions are not symmetric around zero and, with respect to the expected distribution, present an exceeding amounts of events for $0 \lesssim R \lesssim 1$, a slower decrease for $R \to -\infty$ and a faster decrease for $R \to \infty$.

Due to the impossibility to derive a theoretical probability function for R the empirical one was considered:

$$P_{\text{emp}}(R) = \frac{1}{M} \sum_{i=1}^{M} \Theta(R - R_i) \tag{5.6}$$

where Θ is the Heavyside's step function,

$$\Theta(x - a) = 0 \quad \text{for} \quad x < a \quad \text{and} \quad \Theta(x - a) = 1 \quad \text{for} \quad x \geq a,$$

and R_i, for $1 \leq i \leq M = 1000$, is the collection of the values of R obtained for each random dataset. The cdf (5.6) is a steps function only piecewise continuous with jumps of $1/M$ in correspondence of each R_i.

The significance levels of the observed correlation was taken as the two-side probability, in the null hypothesis, to obtain a value of R as or more extreme than that observed, R_{obs}. The null hypothesis is that the dataset belongs to random ones and observed deviations are due to chance.

The two-side probability was obtained summing the the left-side probability and the right-side one:

$$P(|R| \geq |R_{\text{obs}}|) = P(R \leq -|R_{\text{obs}}|) + P(R \geq |R_{\text{obs}}|).$$

The left-side probability was obtained counting the number of random datasets, m, with a value of R equal or below $-|R_{\rm obs}|$, and dividing it by M:

$$P(R \leq -|R_{\rm obs}|) = P_{\rm emp}(-|R_{\rm obs}|) = m/M$$

where

$$m = {\rm num}\{R_i\text{'s} \,:\, R_i \leq -|R_{\rm obs}|\}_M.$$

Likely, the right-side probability was obtained counting the number of random datasets, n, with a value of R above $|R_{\rm obs}|$, and dividing it by M:

$$P(R \geq |R_{\rm obs}|) = 1 - P_{\rm emp}(|R_{\rm obs}|) = n/M$$

where

$$n = {\rm num}\{R_i\text{'s} \,:\, R_i > |R_{\rm obs}|\}_M.$$

Then, the two-side significance level is

$$P(|R| \geq |R_{\rm obs}|) = (m+n)/M. \tag{5.7}$$

The normalization by ${\rm var}(r)_M$ does not matter for the validity of (5.7) and can be neglected taking $R = r - \langle r \rangle_M$ and $R_{\rm obs} = r_{\rm obs} - \langle r \rangle_M$. In this formulation, arises again the role of $\langle r \rangle_M$ as the new level of "zero"-correlation when self-correlation is present.

As small the significance level (5.7) is as much the difference between the observed and the random correlation is significant: i.e. as small is the probability that the observed differences between the original dataset and the random ones are due to chance. Finally, it must be noted that significance levels were derived from the distribution of r and not of r^2 because when self-correlation is involved also the sign of the observed correlation matters.

Significance levels, P (eq. (5.7)), were derived for all sonic levels and wind direction sectors and are reported in table 5.3 along with the observed fraction of variance explained by a linear model between ϕ_m and z/λ, $r^2_{\rm obs}$, and that explained by self-correlation from eq. (5.2), $r^2_{(AX)(BY)}$, and from randomized datasets with random permutations, $r^2_{\rm rand}$. As in table 5.2, $r^2_{\rm rand}$ is the average of r^2 between all 1000 random datasets, the uncertainty of this value, estimated as $\sqrt{{\rm var}(r^2)/M}$, with $M = 1000$, is $\mathrm{O}(10^{-3})$, well below the observed differences. The difference between the observed fraction of variance explained and that explained by self-correlation ($r^2_{\rm obs} - r^2_{(AX)(BY)}$ and $r^2_{\rm obs} - r^2_{\rm rand}$) and the significance level, P (also indicated as *p-value*), are two estimators of the the strength of the observed linear correlation.

The significance level, P, is somewhat superior since it accounts also for the signs of the observed and self-correlation, whereas r^2 does not. However, r^2 gives useful information when observed and self-correlation have the same sign, as usually is for ϕ_m and z/Λ, and it is the most used estimator by other authors (e.g. Klipp and Mahrt (2004) and Vickers et al. (2009)). Instead, when observed and self correlation have about the same magnitude but opposite signs, r^2-differences underestimate the strength of the observed correlation.

At the lowest two levels (table 5.3(a)-(b)), the fraction of explained variance by self-correlation ranges from $\sim 30\%$ to $\sim 45\%$ and from $\sim 20\%$ to $\sim 40\%$ if random datasets, $r^2_{\rm rand}$, or eq. (5.2), $r^2_{(AX)(BY)}$, respectively, are considered. At the highest level (table 5.3(c)), these percentages go down to 20%–40%, for random datasets, and to 10%–30%, for eq. (5.2). These lower values, however, do not indicate that the highest level is lesser affected by self-correlation but, instead, that the effect of self-correlation on a linear model is lesser:

Table 5.3: Fraction of explained variance (observed and from self-correlation), net fraction of explained variance (observed − self-correlation) and significance level, P (eq. (5.7)), of the observed linear correlation between ϕ_m and z/Λ, for each sonic level and wind direction sector.

(a) $z = 3.7\,\mathrm{m}$

Sector	r^2_{obs}	$r^2_{(AX)(BY)}$	r^2_{rand}	$r^2_{\mathrm{obs}} - r^2_{(AX)(BY)}$	$r^2_{\mathrm{obs}} - r^2_{\mathrm{rand}}$	P
120°–150°	0.71	0.37	0.41	0.34	0.30	0.006
90°–120°	0.33	0.30	0.34	0.04	−0.01	0.96
30°–330°	0.52	0.34	0.35	0.19	0.17	0.012
300°–330°	0.41	0.38	0.44	0.03	−0.03	0.85

(b) $z = 7.5\,\mathrm{m}$

Sector	r^2_{obs}	$r^2_{(AX)(BY)}$	r^2_{rand}	$r^2_{\mathrm{obs}} - r^2_{(AX)(BY)}$	$r^2_{\mathrm{obs}} - r^2_{\mathrm{rand}}$	P
120°–150°	0.49	0.40	0.40	0.09	0.08	0.15
90°–120°	0.45	0.23	0.32	0.23	0.10	0.19
30°–330°	0.47	0.35	0.37	0.12	0.10	0.21
300°–330°	0.64	0.25	0.43	0.39	0.21	0.18

(c) $z = 20.5\,\mathrm{m}$

Sector	r^2_{obs}	$r^2_{(AX)(BY)}$	r^2_{rand}	$r^2_{\mathrm{obs}} - r^2_{(AX)(BY)}$	$r^2_{\mathrm{obs}} - r^2_{\mathrm{rand}}$	P
120°–150°	0.36	0.16	0.20	0.20	0.16	0.05
90°–120°	0.08	0.10	0.21	−0.02	−0.14	0.16
30°–330°	0.28	0.27	0.33	0.01	−0.05	0.71
300°–330°	0.003	0.20	0.39	−0.20	−0.38	0.008

indeed, self-correlation does not follow a linear model but, instead, when it is strong $\phi_m \sim (z/\Lambda)^{1/3}$.

For the sectors 120°-150° and 30°–330° at $z = 3.7\,\mathrm{m}$ (table 5.3(a)), and sector 120°-150° at $z = 20.5\,\mathrm{m}$ (table 5.3(c)) the observed correlation is very significant, i.e. $P \leq 0.05$. Significance levels for the sectors 90°–120° and 300°–330° at $z = 7.5\,\mathrm{m}$ (table 5.3(b)) are maybe overestimated (i.e. the observed correlation is more significant that those indicated by P) because the level of self-correlation from random datasets, r^2_{rand}, is sensibly higher than those from eq. (5.2), $r^2_{(AX)(BY)}$.

Some doubts are presents also on the values of P for the same sectors at $z = 20.5$ (table 5.3(c)). In this case, however, the significance of an observed non-correlation is tested (i.e. the observed correlation is lower than both self-correlation levels) and doubts on P regard to a possible underestimation. This have few consequences for the sector 90°–120°, for which the observed non-correlation is yet indicated as non-significant ($P > 0.1$). Instead, for the sector 300°–330°, the very significant ($P < 0.01$) non-correlation observed must be viewed with some suspect because of the near-zero observed correlation, r^2_{obs}, affected by some z/Λ-outliers (fig. 5.2) and the difference between the two levels of self-correlation, r^2_{rand} and $r^2_{(AX)(BY)}$. Then, although $P < 0.01$, we cannot conclude that a true physical mechanism was acting to produce the observed non-correlation.

Considering all the possible errors in the estimation of P discussed above, in general, a net fraction of explained variances (i.e. $r^2_{\mathrm{obs}} - r^2_{(AX)(BY)}$ and $r^2_{\mathrm{obs}} - r^2_{\mathrm{rand}}$) $\gtrsim 0.2$ corresponds to a significant ($P \leq 0.1$) or even very significant ($P \leq 0.05$) observed correlation.

5.4 Self-correlation between ϕ_m and other stability parameters: Ri and R_f

After all the considerations made above self-correlation affecting flux-gradient relationships obtained from ϕ_m vs. z/Λ plots one question arise: Can influence of self-correlation be reduced employing other stability parameters instead of z/Λ?

An alternative stability parameter is the gradient Richardson number. Self-correlation in ϕ_m vs. Ri plots arises because both depend on wind shear, even in an opposite manner: $\phi_m \propto d\overline{S}/dz$ and $\mathrm{Ri} \propto (d\overline{S}/dz)^{-2}$. In this case, however, the the sign of self-correlation is opposite to that of observed correlation. Indeed, the self-correlation behaviour is $\phi_m \propto \mathrm{Ri}^{-2}$ whereas, in stable conditions ϕ_m increases with Ri. Then, the effect of self-correlation in ϕ_m vs. Ri plots is to reduce the strength of observed correlation. This explains the increased scatter in plots of ϕ_m when Ri instead of z/Λ is used.

The level of self-correlation in ϕ_m vs. Ri plots can be obtained from eq. (5.2), taking

$$X = u_*^{-1}, \quad A = \frac{d\overline{S}}{dz}, \quad Y = \frac{1}{\overline{\theta}}\frac{d\overline{\theta}}{dz} \quad \text{and} \quad B = \left(\frac{d\overline{S}}{dz}\right)^{-2}$$

where all constant factors, such as the height above ground, are been neglected. As a further simplification we can take $Y = d\overline{\theta}/dz$ assuming that the coefficient of variation of the potential temperature, $\overline{\theta}$, is much smaller that that of its gradient. In stable conditions we expect $r_{(AX)(BY)} < 0$ and lesser in magnitude that that between ϕ_m and z/Λ since the shared variable is the wind shear which have smaller coefficients of variation than fluxes (section 5.1). When the strength of the observed correlation between ϕ_m and Ri is estimated, the observed correlation coefficient should be compared with the (negative) level of self correlation $r_{(AX)(BY)}$ instead of zero. Plots of ϕ_m vs. Ri were not considered in this study because doubts were present on reliability of temperature measurements.

Another possibility, is to plot ϕ_m against the flux Richardson number. In this case the shared variables are two, the wind shear and the friction velocity. The friction velocity generate a self correlation in the same direction of the observed one, $\phi_m \propto u_*^{-1}$ and $\mathrm{R}_f \propto u_*^{-2}$, whereas the wind shear in the opposite one, $\phi_m \propto d\overline{S}/dz$ and $\mathrm{R}_f \propto (d\overline{S}/dz)^{-1}$ (ϕ_m increases with R_f in the stable boundary layer).

The level self-correlation in ϕ_m vs. R_f plots can be estimated from eq. (5.2) taking

$$X = 1, \quad A = \frac{1}{u_*}\frac{d\overline{S}}{dz}, \quad Y = -\frac{\overline{w'\theta'}}{\overline{\theta}} \quad \text{and} \quad B = \frac{1}{u_*^2}\left(\frac{d\overline{S}}{dz}\right)^{-1}$$

where constant factors are neglected, $V_X = 0$ and we can further take $Y = -\overline{w'\theta'}$ since the coefficient of variation of the heat flux is much greater that that of temperature which is also much smaller than unity. From (5.2) we have then

$$r_{(AX)(BY)} = \frac{r_{AB}}{V_A\sqrt{V_Y^2(1+V_B^2)+V_B^2}} \tag{5.8}$$

where

$$V_A^2 = V_x^2(1+V_y^2)+V_y^2, \quad \text{with} \quad x = \frac{d\overline{S}}{dz}, \quad y = u_*^{-1}$$
$$V_B^2 = V_w^2(1+V_z^2)+V_z^2, \quad \text{with} \quad w = \left(\frac{d\overline{S}}{dz}\right)^{-1}, \quad z = u_*^{-2},$$

where x-y and w-z are pairs of random independent variables but $w = w(x)$ and $z = z(y)$. Furthermore, we have

$$r_{AB} = r_{(xy)(wz)} = \frac{\langle yz\rangle / |\langle x\rangle\langle y\rangle\langle w\rangle\langle z\rangle| - 1}{\sqrt{[V_x^2(1+V_y^2)+V_y^2][V_w^2(1+V_z^2)+V_z^2]}}$$

where it was used the fact that $xw = 1$ and $\langle\cdot\rangle$ indicates the expectation value.

The expression for the self-correlation between ϕ_m and R_f is more complicated because the shared variables are two, and its effects more difficult to predict since the two opposite effect: the negative correlation from the sharing of the wind shear and the positive correlation from the sharing of friction velocity. However, since the coefficients of variation for fluxes are usually greater than those for gradients we expect that $r_{AB} > 0$, and then $r_{(AX)(BY)} > 0$, when R_f is used as stability parameter. Anyway, further investigations are needed.

Conclusions

The question if local similarity theory (an extension of Monin-Obukhov similarity theory) holds for the wind profile in the stably stratified boundary layer, over complex terrain and heterogeneous surfaces, was tackled analyzing more than 2000 hours of turbulence measurements acquired on the Climate Change Tower (CCT), Ny-Ålesund, Svalbard, Norway, from May 2012 to May 2014. During this period, observations were acquired also in the long-lived stable boundary layer which onsets in polar regions from autumn to spring, although unreliable snow height measurements have limited the study of this peculiar conditions. In this work, however, no distinctions were made between long-lived and "conventional" stable boundary layers. The tower is located in a fjord and the experimental site is characterized by undulated terrain, glaciers, mountains up to 700-m high few kilometers far from the tower and sea-land transitions. Furthermore, the seasonal cycle of snow-covered and snow-free ground is also present. All these factors generate complex land-ice-sea-atmosphere interactions making the study of the boundary layer very challenging and this experiment a sever verification test for the limits of applicability of local similarity theory.

Due to the lack of calibration tests, an intercomparison between wind speed observations from all sonic and propeller anemometers on the CCT was carried out. During this, a time lag of 10 min between sonic and propeller readings was found and a new synchronized dataset generated. The better agreement was observed between propeller observations. Sonic anemometers showed less coherent measurements and an average over-speeding of about 5% with respect to the propeller data. These deviations between propeller and sonic anemometers were attributed to different boom lengths (and orientation) for the two instruments types causing uneven influences of the tower structure (in particular for the highest sonic anemometer, located at 20.5 m). Particularly important is that largest deviations between propeller and sonic readings were observed for the prevailing wind direction (i.e. 110°-120°) for which the tower should have the optimal orientation. This suggest also that the influence of the tower structure on observed wind speed could be not negligible also for optimal wind directions and that longer booms should be employed to reduce it.

A special attention throughout the whole work was dedicated to methods. In this case, those for the computation of gradients. In particular, the sensitivity of gradients to the evaluation method was inquired. This is a crucial question for local similarity theory since gradients are needed for the derivation of the dimensionless wind shear, ϕ_m. A comparison was made between gradients computed with finite and log-finite differences, fitting wind speed observations with log-linear and log-log^2 profiles and interpolating them with Bessel and log-Bessel splines (log- means that $\ln z$, instead of z, was taken as independent variable). Interpolations, fits and finite differences were carried-out on propeller observations only (at 2.0, 4.8, 10.3 and 33.4 m), which showed the best agreement. Derivatives are then computed

at sonic levels (at 3.7, 7.5 and 20.5 m), where turbulence measurements were available. Because of observed deviations, the use of both propeller and sonic observations would have led to wildly oscillations in interpolated profiles and unrealistically high gradients.

Wind speed vertical gradients have shown small sensitivity to the evaluation method at the lowest (3.7 m) and at the highest (20.5 m) sonic levels when log-methods (i.e. log-finite differences, log-Bessel splines, log-linear and log-log^2 fits) were used. A larger sensitivity was instead observed at the middle sonic level (7.5 m) because this resulted near to the height of maximum non systematics deviations between log-linear and log-log^2 derivatives. Log-methods should be preferred on linear ones (in particular Bessel-splines) which produced systematically higher or lower derivatives, depending on the level. This is because the logarithmic behaviour, usually dominant in observed profiles, is easily captured when $\ln z$, instead of z, is used as independent variable.

A problem affecting the CCT dataset is that of intermittent and unreliable snow height measurements since long-lived stable boundary layers onset mostly during the permanent snow-cover season, from October to May. Some long-lived cases occur also in September and nocturnal stable boundary layers form in June and August, whit snow-free ground. In the present work, the height of measurement levels was taken equal to that above snow-free ground, without any correction for snow depth, and were excluded from the analysis observations acquired from December to April, when snow depth over 50 cm occurred at Ny-Ålesund.

Erroneous estimations of z influence directly both ϕ_m and the stability parameter, z/Λ. However, ϕ_m is affected also indirectly through wind speed gradients. Indeed, the skill of log-methods in the interpolation of logarithmic profiles decreases as the estimated height above ground of observational levels deviates from the true one. The sensitivity of gradients to an unknown displacement height, d, depends on method and level of computation. For a logarithmic profile and $d = 1$ m errors up to 10% in gradients estimation occur. Considering all the three sonic levels, log-Bessel gradients resulted the least affected by errors in z, although log-finite differences showed even smaller errors at 7.5 and 20.5 m. The effect of an unknown displacement height on similarity functions depend on z/Λ and on the function itself. For linear functions, i.e. $\phi_m(z/\Lambda) = 1 + \beta(z/\Lambda)$, deviations between expected and estimated ϕ_m decrease as z/Λ increases. This is indeed an expected behaviour, since when the z-less regime is reached, i.e. $\phi_m \approx \beta(z/\Lambda)$, turbulence does not depend anymore on the height above ground.

Largest deviations between expected and observed ϕ_m were related mostly to weak winds and tower perturbed flows. The sector 150°-300° was recognized as the most perturbed by the tower structure and excluded from the analysis. A wind speed threshold of 3 m s^{-1} was also adopted as a good compromise between the reduction of points scatter (in ϕ_m vs. z/Λ plots) and number of retained runs. Other authors have shown that this threshold discriminates well between weak or intermittent turbulence and continuous turbulence.

Since of the complex terrain and heterogeneous surface characterizing the experimental site, data were further subdivided in four wind direction sectors: from west to south-west, 300°-330°, 330°-30° (around north), 90°-120° and 120°-150°.

The largest deviations between flux-gradient relationships from different sectors were observed in the weakly stable and near-neutral range (i.e. $z/\Lambda \lesssim 0.1$) and for strong winds (i.e. $S > 9$ m s^{-1}). This deviations manifested as higher than expected values of ϕ_m associated to anomalously small heat fluxes. Interesting results arose from the north-western sector (300°-330°) for which this anomalous behaviour was observed at the middle (7.5 m) and the highest (20.5 m) sonic levels but not at the lowest one (3.7 m), where

observed ϕ_m agreed with most used empirical functions. These deviations were associated with a two-layers structure in heat flux profiles, with a shallow surface layer (below 7 m) and a small-flux layer above. This two-layers structure was not present in profiles of wind speed and momentum flux, that were those of a surface layer extending up to the highest level. It would has been interesting to analyze also temperature profiles but doubts were present on reliability of temperature measurements.

Since the sector 300°-330° contains a sea-land transition, it was speculated that this two-layers structure was a manifestation of internal boundary layers formation in conditions of on-shore flows. In particular, the advected layer seems to adjust dynamically but not thermally with the local surface. The same mechanism can also explain the observed deviations for the northern sector (330°-30°) which should be even more influenced by sea-land transitions. However, in this case, also the lowest level is affected, maybe because the shorter land-fetch does not permit even the formation of a shallow surface layer.

Because of these anomalously small fluxes, the local Obukhov length, Λ, is not anymore representative of true stability conditions. This means that points ling on expected empirical functions, move horizontally in the ϕ_m–z/Λ plane toward lower values of z/Λ, generating higher than expected values of ϕ_m and the failure of local similarity theory.

For $z/\Lambda \gtrsim 0.1$, deviations of ϕ_m were mostly between levels, than between sectors, with decreasing ϕ_m as the height above ground increased. The best agreement between observed and expected ϕ_m was observed at the lowest sonic level (3.7 m), in particular with the empirical function prosed by Beljaars and Holtslag (1991). However, in the limited stability range of the considered dataset (i.e. $z/\Lambda \lesssim 1$) deviations between most used formulations are small. Dimensionless gradients at the middle sonic level (7.5 m) were generally smaller with a dependence on z/Λ resembling that from self-correlation: $\phi_m \propto (z/\Lambda)^{1/3}$. The self-correlation behavior is particularly evident for the highest sonic level (20.5 m).

It was hypothesized that lower than expected values of ϕ_m were originated by enhanced turbulence from complex terrain. Indeed, highly variable fluxes of momentum, showing even signatures of upside-down boundary layers, were observed for most of the sectors in moderately stable conditions ($0.1 \leq z/\Lambda \leq 1$). Stable conditions usually occur with lighter winds and then smaller wind shears. It is then possible that, as stability increases, terrain-generated turbulence becomes an important fraction (or even dominates on) shear-generated turbulence. This could also explain the break-down of flux-gradient relationships (indicated by the $\phi_m \propto (z/\Lambda)^{1/3}$-behaviour) observed at 20.5 m and, to a lesser extent, at 7.5 m.

It is also possible that high and variable fluxes were a manifestation of instrumental errors or tower perturbed flows. These doubts regard in particular the highest sonic level (20.5 m) for which ϕ_m showed the self-correlation behaviour, $\phi_m \propto (z/\Lambda)^{1/3}$, for the whole stability range, with the exception of the sector 330°-300°.

The expression for the linear self-correlation coefficient between ϕ_m and z/Λ due to the shared variable u_* (the local friction velocity) was derived. This is the level of no-correlation, instead of zero, against which the observed linear correlation should be compared. The level of self-correlation depends on the distributions of the shared and non-shared variables, taking all points in the considered dataset. In particular, strong self-correlation arises when the coefficient of variation of the shared variable (u_*) is large and those of the non-shared variables (heat flux and wind shear) are small. For the CCT dataset, self-correlation coefficients ranged from 0.3 to 0.6, depending on level and wind direction sector.

The strength of the observed correlation between ϕ_m and z/Λ was estimated comparing the observed linear correlation coefficient with the empirical probability distribution function

of the self-correlation coefficient, derived trough the generation of random datasets. These were obtained with random permutations and sampling with replacement from the original dataset. Random permutations (sampling without replacement) should be preferred since the distributions of variables in the original dataset are retained also in the randomized ones.

A drawback of the linear correlation coefficient as self-correlation estimator is its sensitivity to outliers. This was retained the main cause for the observed overestimation of the self-correlation coefficient derived through randomized datasets. Indeed, randomization generates some z/Λ-outliers, (i.e. points characterized by anomalously high values of z/Λ) that strongly influences the correlation index of the whole dataset.

Another limitation is that ϕ_m and z/Λ could be non-linearly related (although most used empirical functions can be approximated by a linear model for $z/\Lambda \lesssim 1$) making the linear correlation coefficient a poor estimator of the observed correlation. In this case, if the observed relation is $\phi_m = f(z/\Lambda)$, the linear correlation coefficient should be computed between ϕ_m and $f(z/\Lambda)$ both for the original and the randomized datasets. The expression derived for the self-correlation coefficient can be adapted to the non-linear case approximating the observed function with power laws, i.e. $f(z/\Lambda) \approx \text{const.} + (z/\Lambda)^{\alpha}$, in different intervals of (z/Λ) and comparing observed and self-correlation coefficients in each interval. Estimators that are non-sensitive to the functional form of the tested model, such as the rank correlation coefficient, have the drawback that they do not distinguish either between the observed relationship and that from self correlation.

If the effect of self-correlation in ϕ_m vs. z/Λ plots is usually to strength the observed correlation, since observed and self-correlation are about in the same direction, the opposite is true in ϕ_m vs. Ri plots (Ri, the gradient Richardson number). This means that, when observed correlation in ϕ_m vs. Ri plots is compared by a level of no-correlation equal to zero, the strength of the observed correlation is underestimated.

Final considerations and possible future research

A calibration test between the anemometers of the CCT (particularly sonic ones) seems necessary, to exclude the effect of measurement errors on the obtained results. Also their disposition, maybe too near to the tower structure, could be reconsidered.

The study of the boundary layer in Ny-Ålesund was very challenging because of complex sea-land-ice-atmosphere interactions. In particular, the formation of internal boundary layers for on-shore flows and the effect of enhanced turbulence by the complex terrain could be arguments of future research.

The effect of self-correlation on similarity plots requires further investigations both in methods for its estimation and in the development of alternative similarity schemes not affected by self-correlation.

Finally, the observed limitations of local similarity theory on complex and heterogeneous surfaces, if confirmed, suggest that new theories are necessary for these conditions.

Bibliography

Argentini, S., G. Mastrantonio, I. Petenko, I. Pietroni, and A. Viola (2012). «Use of a high-resolution sodar to study surface-layer turbulence at night». In: *Boundary-Layer Meteorology* 143, pp. 177–188.

Baas, P., G. J. Steeneveld, B. J. H. van de Wiel, and A. A. M. Holtslag (2006). «Exploring self-correlation in Flux-gradient relationships for stably stratified conditions». In: *Journal of the Atmospheric Sciences* 63, pp. 3045–3054.

Beljaars, A. C. M. and A. A. M. Holtslag (1991). «Flux parametrization over land ssurface for atmospheric models». In: *Journal of Applied Meteorology* 30, pp. 327–341.

Businger, J. A., J. C. Wyngaard, Y. Izumi, and E. F. Bradley (1971). «Flux-profile relationships in the atmospheric surface layer». In: *Journal of the Atmospheric Sciences* 28, pp. 181–189.

Caporaso, L., A. Riccio, F. Di Giuseppe, and F. Tampieri (2013). «Relating mean radiosoundings profiles to surface fluxes for the very stable boundary layer». In: *Boundary-Layer Meteorology* 147, pp. 203–215.

Cheng, Y. and W. Brutsaert (2005a). «Flux-profile relationship for wind speed and temperature in the stable atmospheric boundary layer». In: *Boundary-Layer Meteorology* 114, pp. 519–538.

Cheng Y. andCheng, Y. M. B. and W. Brutsaert (2005b). «Pathology of Monin-Obukhov Similarity in the stable boundary layer». In: *Journal of Geophysical Research* 110, D06101, doi:10.1029/2004JD004923.

De Boor, C. (2001). *A practical guide to splines*. Ed. by J. E. Mardsen and L. Sirovich. Revised edition. Vol. 27. Applied mathematical sciences. New York: Springer-Verlag.

Dyer, A. J. (1974). «A review of Flux-gradient relationships». In: *Boundary-Layer Meteorology* 7, pp. 363–372.

Forrer, J. and M. W. Rotach (1997). «On the Turbulence structure in the stable boundary layer over the Greenland ice sheet». In: *Boundary-Layer Meteorology* 85, pp. 111–136.

Grachev, A. A., C. W Fairall, P. O. G. Persson, E. L Adreas, and P. S. Guest (2005). «Stable boundary-layer regimes: the SHEBA data». In: *Boundary-Layer Meteorology* 116, pp. 201–235.

Grachev, A. A., E. L. Adreas, C. W Fairall, P. S. Guest, and P. O. G. Persson (2007a). «On the turbulent Prandtl number in the stable atmospheric boundary layer». In: *Boundary-Layer Meteorology* 125, pp. 329–341.

Grachev, A. A., E. L. Adreas, C. W Fairall, P. S. Guest, and P. O. G. Persson (2007b). «SHEBA flux-profile relationships in the stable atmospheric boundary layer». In: *Boundary-Layer Meteorology* 124, pp. 315–333.

Grachev, A. A., E. L. Adreas, C. W Fairall, P. S. Guest, and P. O. G. Persson (2013). «The critical Richardson number and limits of applicability of local similarity theory in the stable boundary layer». In: *Boundary-Layer Meteorology* 147, pp. 51–82.

Ha, K.-Y., Y.-K. Hyun, H.-M. Oh, K.-E. Kim, and L. Mahrt (2007). «Evaluation of boundary layer Similarity theory for stable conditions in CASES-99». In: *Monthly Weather Review* 135, pp. 3474–3483.

Haugen, D. A., J. C. Kaimal, and E. F. Bradley (1971). «Anexconditions study of Reynolds stress and heat flux in the atmospheric surface layer». In: *Quarterly Journal of the Royal Meteorological Society* 97, pp. 168–180.

Högström, U. (1988). «Non-dimensional wind and temperature profiles in the atmospheric surface layer: A re-evaluation». In: *Boundary-Layer Meteorology* 42, pp. 55–78.

Högström, U. (1996). «Review of some basic characteristics of the atmospheric surface layer». In: *Boundary-Layer Meteorology* 78, pp. 215–246.

Holtslag, A. A. M. (1984). «Estimates of diabatic wind speed profiles from near-surfcae weather observations». In: *Boundary-Layer Meteorology* 29, pp. 225–250.

Howell, J. F. and J. Sun (1999). «Surface-layer fluxes in stable conditions». In: *Boundary-Layer Meteorology* 90, pp. 495–520.

ISAC–CNR (2014). *CCT Integrated Project*. URL: http://www.isac.cnr.it/~radiclim/CCTower/.

Kaimal, J. C. and J. J. Finnigan (1994). *Atmospheric boundary layer flows. Their structure and measuremet*. Oxford University Press.

Kim, J.-H. (1999). «Spurious correlation between ratios with a common divisor». In: *Statistics and Probability Letters* 44, pp. 383–386.

Klipp, C. L. and L. Mahrt (2004). «Flux-gradient relationship, self-correlation and intermittency in the stable boundary layer». In: *Quarterly Journal of the Royal Meteorological Society* 130, pp. 2087–2013.

Liang, J., L. Zhang, Y. Wang, X. Cao, Q. Zhang, H. Wang, and B. Zhang (2014). «Turbulence regimes and the validity of similarity theory in the stable boundary layer over complex terrain of the Loess Plateau, China». In: *Journal of Geophysical Research Atmopsheres* 119, pp. 6009–6021.

Mahrt, L. (1986). «On the shallow motion approximation». In: *Journal of the Atmospheric Sciences* 43, pp. 1036–1044.

Maturilli, M., A. Herber, and G. König-Langlo (2013). «Climatology and time series of surface meteorology in Ny-Ålesund, Svalbard». In: *Earth System Science Data* 5, pp. 155–163.

Monin, A. S. and A. M. Obukhov (1954). «Basic laws of turbulent mixing in the surface layer of the atmosphere». In: *Tr. Akad. Nauk SSSR Geophiz. Inst.* 151, pp. 163–187.

Nieuwstadt, F. T. M. (1984). «The turbulent structure of the stable, nocturnal boundary layer». In: *Journal of the Atmospheric Sciences* 41.14, pp. 2202–2216.

Norwegian Polar Institute (2014). *Terrengmodell Svalbard (S0 Terrengmodel)*. Tromsø, Norway: Norwegian Polar Institute. URL: https://data.npolar.no/dataset/dce53a47-c726-4845-85c3-a65b46fe2fea.

Norwegian Polar Institute (2015). *Svalbardkartet*. URL: http://svalbardkartet.npolar.no/.

Obukhov, A. M. (1971). «Turbulence in an atmosphere with a non-uniform temperature». In: *Boundary-Layer Meteorology* 2, pp. 7–29.

Press, W. H., S. A. Teukolsky, W. T. Vetterling, and B. P. Flannery (1997). *Numerical Recipes in Fortran 77: The art of scientific computing*. Second Edition. Vol. 1. Fortran Numerical Recipes. Cambridge University Press.

Salesky, S. T. and M. Chamecki (2012). «Random errors in Turbulence measurements in the atmospheric surface layer: implications for Monin-Obukhov similarity theory». In: *Journal of the Atmospheric Sciences* 69, pp. 3700–3714.

Sorbjan, Z. (1986). «On similarity in the atmospheric boundary layer». In: *Boundary-Layer Meteorology* 34, pp. 377–397.

Sorbjan, Z. and A. A. Grachev (2010). «An evaluation of the Flux-gradient relationship in the stable boundary layer». In: *Boundary-Layer Meteorology* 135, pp. 385–405.

Spiegel, E. A. and G. Veronis (1960). «On the Boussinesq approximation for a compressible fluid». In: *Astrophysics Journal* 131, pp. 442–447.

Stull, R. B. (1988). *An introduction to boundary layer meteorology*. Springer.

Taylor, J. R. (2000). *Introduzione all'analisi degli errori. Lo studio delle incertezze nelle misure fisiche*. Seconda edizione. Italian translation of *An introduction to error analysis. The study of uncertainities in physical measurements*. Second Edition. (1997) University Science Books. Bologna: Zanichelli.

Vickers, D., C. K. Thomas, J. G. Martin, and B. Law (2009). «Self-correlation between assimilation and respiration resulting from flux partitioning of eddy-covariance CO_2 fluxes». In: *Agricultural and Forest Meteorology* 149, pp. 1552–1555.

Wyngaard, J. C. (1981). «Cup, propeller, vane, and sonic anemometers in Turbulence research». In: *Annaual Review in Fluid Mechanics* 13, pp. 399–423.

Wyngaard, J. C. (2010). *Turbulence in the atmosphere*. Cambridge University Press.

Wyngaard, J. C. and O. R. Coté (1972). «Cospectral similarity in the atmospheric surface layer». In: *Quarterly Journal of the Royal Meteorological Society* 98, pp. 590–603.

Yagüe, C., S. Viana, G. Maqueda, and J. M. Redondo (2006). «Influence of stability on the flux-profile relationships for wind speed, ϕ_m, and temperature, ϕ_h, for the stable atmospheric boundary layer». In: *Nonlinear Processes in Geophysics* 13, pp. 185–203.

Zilitinkevich, S. S. and I. N. Esau (2007). «Similarity theory and calculation of turbulent fluxes at the surface fot the stably stratified atmospheric boundary layer». In: *Boundary-Layer Meteorology* 125, pp. 193–205.

Acknowledgments

I wish to thank prof. Silvana Di Sabatino and prof. Francesco Tampieri for his useful suggestions and Dr. Mauro Mazzola, who prepared the dataset on which I have worked and gave me clarifications about it.

The Department of Earth System Science and Environmental Technologies of the Italian National Research Council (CNR) has financed the construction of the Amundsen-Nobile Climate Change Tower, from which analyzed measurements come. The set of instruments installed at the height of 20.5 m was provided by the Korea Polar Research Institute (KOPRI).

Finally, thanks go to my parents, Graziana and Franco, my grandparents, Enrico, Leda and Gemma, and my friends that supported me, especially in my cloudy days.